U.PORTO

FEUP FACULDADE DE ENGENHARIA
UNIVERSIDADE DO PORTO

The extension of a radial point interpolation meshless method to the viscoplastic extrusion process

Rui Orlando Silva Sampaio da Costa

Thesis submitted to Faculdade de Engenharia da Universidade do Porto
as a requirement to obtain the MSc Degree in Mechanical Engineering

Under the supervision of:
Professor Jorge Américo Oliveira Pinto Belinha
Professor Renato Manuel Natal Jorge

Porto, July 2018

© Rui Costa, 2018

"A great dream is not as good as a great memory.
The dream can be had by anyone.
The memory - must be made!"
Eric Thomas

This page has been intentionally left blank.

Agradecimentos

Em primeiro lugar, quero exprimir a minha gratidão ao professor Jorge Belinha, por todo o apoio durante a desenvolvimento da dissertação, todo o entusiasmo, motivação e confiança que depositou em mim. Também por todo o acompanhamento ao longo dos anos em que tanto aprendi e me desenvolvi. Ao professor Renato Natal pela oportunidade de fazer parte da equipa e de trabalhar em mecânica computacional.

Aos meus amigos Israel Modesto, Dani Ribery, Barreiros da Costa, Miss Teenager, Nicky Nightmares e Penelope Cruz, pela amizade que perdura e se mantém ao longo dos anos sempre com o mesmo carinho, companheirismo e aleatoriedade. Um muito obrigado a vocês todos por tudo o que fizeram por mim mesmo que não o saibam.

Àqueles que conheci há 5 anos e me acompanharam desde então e especialmente à Chica, Varela, Pedro, CP, Piri e Rafa. Um enorme obrigado amigos, convosco passei momentos inesquecíveis que tornaram todos estes anos mais fáceis e me fizeram crescer imenso. Ao meu padrinho, Tiga, um grande obrigado por me fazer ver as coisas sempre de maneira diferente. À Ana Isabel por todas as conversas que me deram tanto e que nunca esquecerei.

Por fim, quero agradecer à minha família. Ao meu irmão, Daniel, por todas as palavras de encorajamento, apoio e positividade ao longo dos anos. Aos meus pais, Isabel e António, por fazerem tudo para que nunca me faltasse nada, por tornarem tudo isto possível e me deixarem sonhar.

This page has been intentionally left blank.

Institutional Acknowledgements

The author truly acknowledges the work conditions provided by the Applied Mechanics Division (SMAp) of the department of mechanical engineering (DEMec) of Faculty of Engineering of the University of Porto (FEUP), and by the MIT-Portugal project "MIT-EXPL/ISF/0084/2017", funded by Massachusetts Institute of Technology (USA) and "Ministério da Ciência, Tecnologia e Ensino Superior - Fundação para a Ciência e a Tecnologia" (Portugal).

Additionally, the authors gratefully acknowledge the funding of Project NORTE-01-0145-FEDER-000022 - SciTech - Science and Technology for Competitive and Sustainable Industries, cofinanced by Programa Operacional Regional do Norte (NORTE2020), through Fundo Europeu de Desenvolvimento Regional (FEDER).

Finally, the author acknowledges the synergistic collaboration with the collaborators of "Computational Mechanics Research Laboratory CMech-Lab" (ISEP/ FEUP/ INEGI), and its director, Prof.Dr. Jorge Belinha, and its senior advisers, Prof.Dr. Renato Natal Jorge and Prof.Dr. Lúcia Dinis.

This page has been intentionally left blank.

Abstract

Additive manufacturing is an emergent technology, which witnessed a large growth demanded by the consumer market. Despite this growth, the technology is in need of scientific regulation and guidelines to be reliable and consistent to the point that is feasible to be used as a source of manufactured end-products. One of the processes that has seen the most significant development is the Fused Deposition Modelling (FDM), more commonly known as 3D printing. The motivation to better understand this process makes the study of extrusion of materials important.

In this work, the Radial Point Interpolation Method (RPIM), a meshless method, is applied to the study of extrusion of viscoplastic materials, using the formulation originally intended for the Finite Element Method (FEM), the *flow formulation*. This formulation is based on the reasoning that solid materials under those conditions behave like non Newtonian fluids. The time stepped analysis follows the Lagrangian approach taking advantage of the easy remeshing inherent to meshless methods.

In order to validate the newly developed numerical tool, exhaustive tests are conducted with numerical examples obtained from the literature for the extrusion of aluminium. The program parameters are optimized and the numerical results compared to another meshless method and the FEM.

Keywords: meshless methods; extrusion; flow formulation; additive manufacturing; metal forming.

This page has been intentionally left blank.

Resumo

O fabrico aditivo é uma tecnologia emergente que verificou um grande crescimento originado pelo consumidor geral. Apesar deste crescimento a tecnologia requer regulação científica para ser fiável e consistente ao ponto de ser utilizada para fabricar componentes finais. Um dos processos que maior crescimento verificou foi o *Fused Deposition Modelling* (FDM), ou vulgarmente designado por impressão 3D. A motivação de estudar e entender melhor este processo torna o estudo da extrusão de materiais importante.

Neste trabalho aplica-se o método sem malha *Radial Point Interpolation Method* (RPIM) ao estudo da extrusão de materiais viscoplásticos, usando a formulação originalmente desenvolvida para o método dos elementos finitos, *flow formulation*. Esta formulação tem por base o raciocínio de considerar que materais sólidos naquelas condições se comportam como fluidos não Newtonianos. As análises ao longo do tempo são feitas usando a abordagem de Lagrange pelo que se tira partido da facilidade de atualizar as coordenadas nodais no método sem malha.

De forma a validar a nova ferramenta numérica desenvolvida, esta é testada exaustivamente através de exemplos numéricos encontrados na literatura para a extrusão de alumínio. Os parâmetros do cógido são otimizados e os resultados comparados numericamente a outro método sem malha e ao método dos elementos finitos.

Palavras-chave: métodos sem malha; extrusão; fabrico aditivo; conformação plástica.

This page has been intentionally left blank.

Contents

Acknowledgements **iv**

Institutional acknowledgements **vi**

Abstract **viii**

Resumo **x**

List of Figures **xiv**

List of Tables **xix**

Notation **xx**

1 Introduction **1**
1.1 Meshless methods 1
1.2 Fused Deposition Modelling 2
1.3 Flow formulation and numerical methods 3
1.4 Objectives 4
1.5 Structure 4

2 Meshless Methods **7**
2.1 Outline of the General Procedure 7
2.2 Radial Point Interpolation Method 11
2.2.1 Properties of the RBF Shape Functions 14
2.3 Linear Elasticity with RPIM 14
2.3.1 Solid Mechanics Fundamentals 15
2.3.2 Galerkin Weak Form 17
2.3.3 Discrete Equations 18
2.3.4 2D Linear Elastic Examples 19

3 Flow Formulation **25**
3.1 Governing Equations 25
3.1.1 Material Laws 29
3.2 Discrete Equations 31
3.2.1 Direct Method 33
3.2.2 Mixed Method 34
3.2.3 Mixed Dual Method 35
3.3 Code Considerations 36
3.3.1 General Static Procedure 37

3.3.2 Time Stepped Procedure 41

4 Preliminary Results **45**
4.1 Direct Method 46
4.1.1 Order of Integration 46
4.2 Mixed Method 54
4.2.1 Order of Integration 54
4.3 Mixed Dual Method 61
4.3.1 Order of Integration 61
4.3.2 Nodes Inside the Influence Domains 68
4.3.3 Mesh Independence 76
4.3.4 Convergence Study 84
4.3.5 Time Stepped Results 94

5 Benchmark results **101**
5.1 Problem Definition 101
5.2 Mixed Dual Method 105

6 Conclusion **111**

Bibliography **115**

List of Figures

2.1 Schematic representation of the nodal discretization of a domain. . . 7
2.2 Representation of the background integration mesh. 8
2.3 Gauss quadrature procedure. 9
2.4 Representation of the construction of influence domains. 10
2.5 Representation of the Pascal's triangle of monomials. 11
2.6 Schematic representation of the four models studied. 20
2.7 Results obtained with the FEM and RPIM for model 1. 21
2.8 Results obtained with the FEM and RPIM for model 2. 21
2.9 Results obtained with the FEM and RPIM for model 3. 22
2.10 Results obtained with the FEM and RPIM for model 4. 22
2.11 Comparison of results between methods. 23

3.1 Relationship between properties for various materials [1]. 31

4.1 Schematic representation of model studied. 46
4.2 Reference results from the meshless study [2]. 46
4.3 Nodal mesh analysed with the direct method $divL = divD = 48$. . . . 47
4.4 Results obtained with full integration in the direct method and $quado = 2$. 48
4.5 Results obtained with full integration in the direct method and $quado = 3$. 48
4.6 Results obtained with full integration in the direct method and $quado = 4$. 48
4.7 Results obtained with full integration in the direct method and $quado = 5$. 49
4.8 Results obtained with full integration in the direct method and $quado = 6$. 49
4.9 Results obtained with full integration in the direct method and $quado = 7$. 49
4.10 Results obtained with full integration in the direct method and $quado = 8$. 50
4.11 Results obtained with full integration in the direct method and $quado = 9$. 50
4.12 Results obtained with full integration in the direct method and $quado = 10$. 50
4.13 Results obtained with hybrid integration in the direct method and $quado = 2$. 51
4.14 Results obtained with hybrid integration in the direct method and $quado = 3$. 51

4.15 Results obtained with hybrid integration in the direct method and *quado* = 4. 51
4.16 Results obtained with hybrid integration in the direct method and *quado* = 5. 52
4.17 Results obtained with hybrid integration in the direct method and *quado* = 6. 52
4.18 Results obtained with hybrid integration in the direct method and *quado* = 7. 52
4.19 Results obtained with hybrid integration in the direct method and *quado* = 8. 53
4.20 Results obtained with hybrid integration in the direct method and *quado* = 9. 53
4.21 Results obtained with hybrid integration in the direct method and *quado* = 10. 53
4.22 Results obtained with full integration in the mixed method and *quado* = 2. 54
4.23 Results obtained with full integration in the mixed method and *quado* = 3. 55
4.24 Results obtained with full integration in the mixed method and *quado* = 4. 55
4.25 Results obtained with full integration in the mixed method and *quado* = 5. 55
4.26 Results obtained with full integration in the mixed method and *quado* = 6. 56
4.27 Results obtained with full integration in the mixed method and *quado* = 7. 56
4.28 Results obtained with full integration in the mixed method and *quado* = 8. 56
4.29 Results obtained with full integration in the mixed method and *quado* = 9. 57
4.30 Results obtained with full integration in the mixed method and *quado* = 10. 57
4.31 Results obtained with hybrid integration in the mixed method and *quado* = 2. 58
4.32 Results obtained with hybrid integration in the mixed method and *quado* = 3. 58
4.33 Results obtained with hybrid integration in the mixed method and *quado* = 4. 58
4.34 Results obtained with hybrid integration in the mixed method and *quado* = 5. 59
4.35 Results obtained with hybrid integration in the mixed method and *quado* = 6. 59
4.36 Results obtained with hybrid integration in the mixed method and *quado* = 7. 59
4.37 Results obtained with hybrid integration in the mixed method and *quado* = 8. 60
4.38 Results obtained with hybrid integration in the mixed method and *quado* = 9. 60

4.39 Results obtained with hybrid integration in the mixed method and $quado = 10$. 60
4.40 Nodal mesh analysed with the mixed dual method. 61
4.41 Results obtained with the mixed dual method and $quado = 2$. 62
4.42 Results obtained with the mixed dual method and $quado = 3$. 62
4.43 Results obtained with the mixed dual method and $quado = 4$. 62
4.44 Results obtained with the mixed dual method and $quado = 5$. 62
4.45 Results obtained with the mixed dual method and $quado = 6$. 63
4.46 Results obtained with the mixed dual method and $quado = 7$. 63
4.47 Results obtained with the mixed dual method and $quado = 8$. 63
4.48 Results obtained with the mixed dual method and $quado = 9$. 63
4.49 Results obtained with the mixed dual method and $quado = 10$. 64
4.50 Schematic representation of model with the interest point A (green) and lines (orange). 64
4.51 Evolution of velocity at a point and the time of computation for each order of integration. 65
4.52 Differences in velocity and time relative to the 10^{th} order of integration 65
4.53 Ratio between relative difference in time and relative difference in velocity. 66
4.54 Vertical velocity component on the same horizontal line for each order of integration. 67
4.55 Velocity profiles for each order of integration in the same vertical line. 67
4.56 Detail of the velocity profiles. 68
4.57 Nodal mesh analysed with the mixed dual method. 68
4.58 Results obtained with the mixed dual method and $n_{dom} = 10$. 69
4.59 Results obtained with the mixed dual method and $n_{dom} = 11$. 69
4.60 Results obtained with the mixed dual method and $n_{dom} = 12$. 69
4.61 Results obtained with the mixed dual method and $n_{dom} = 13$. 69
4.62 Results obtained with the mixed dual method and $n_{dom} = 14$. 70
4.63 Results obtained with the mixed dual method and $n_{dom} = 15$. 70
4.64 Results obtained with the mixed dual method and $n_{dom} = 16$. 70
4.65 Results obtained with the mixed dual method and $n_{dom} = 17$. 70
4.66 Results obtained with the mixed dual method and $n_{dom} = 18$. 71
4.67 Results obtained with the mixed dual method and $n_{dom} = 19$. 71
4.68 Results obtained with the mixed dual method and $n_{dom} = 20$. 71
4.69 Results obtained with the mixed dual method and $n_{dom} = 21$. 71
4.70 Results obtained with the mixed dual method and $n_{dom} = 22$. 72
4.71 Results obtained with the mixed dual method and $n_{dom} = 23$. 72
4.72 Results obtained with the mixed dual method and $n_{dom} = 24$. 72
4.73 Results obtained with the mixed dual method and $n_{dom} = 25$. 72
4.74 Results obtained with the mixed dual method and $n_{dom} = 26$. 73
4.75 Results obtained with the mixed dual method and $n_{dom} = 27$. 73
4.76 Results obtained with the mixed dual method and $n_{dom} = 28$. 73
4.77 Results obtained with the mixed dual method and $n_{dom} = 29$. 73
4.78 Results obtained with the mixed dual method and $n_{dom} = 30$. 74
4.79 Results obtained with the mixed dual method and $n_{dom} = 31$. 74
4.80 Results obtained with the mixed dual method and $n_{dom} = 32$. 74

4.81 Evolution of the velocity a point with the number of nodes inside the influence domain. 75
4.82 Evolution of the velocity with number of nodes considering only the valid solutions. 76
4.83 Nodal mesh analysed with $\lambda = 1000$. 77
4.84 Nodal mesh analysed with $\lambda = 100$. 77
4.85 Nodal mesh analysed with $\lambda = 10$. 78
4.86 Nodal mesh analysed with $\lambda = 7,5$. 78
4.87 Nodal mesh analysed with $\lambda = 5$. 79
4.88 Nodal mesh analysed with $\lambda = 4$. 79
4.89 Nodal mesh analysed with $\lambda = 3$. 80
4.90 Nodal mesh analysed with $\lambda = 2$. 80
4.91 Results obtained with the mixed dual method and $\lambda = 1000$. 81
4.92 Results obtained with the mixed dual method and $\lambda = 100$. 81
4.93 Results obtained with the mixed dual method and $\lambda = 10$. 81
4.94 Results obtained with the mixed dual method and $\lambda = 7,5$. 81
4.95 Results obtained with the mixed dual method and $\lambda = 5$. 82
4.96 Results obtained with the mixed dual method and $\lambda = 4$. 82
4.97 Results obtained with the mixed dual method and $\lambda = 3$. 82
4.98 Results obtained with the mixed dual method and $\lambda = 2$. 82
4.99 Evolution of the solution as the mesh becomes more regular. 83
4.100Error associated with every degree of irregularity. 84
4.101Nodal mesh analysed with $divL = divD = 6$ and $\lambda = \infty$. 85
4.102Nodal mesh analysed with $divL = divD = 12$ and $\lambda = \infty$. 85
4.103Nodal mesh analysed with $divL = divD = 12$ and $\lambda = \infty$. 86
4.104Nodal mesh analysed with $divL = divD = 12$ and $\lambda = \infty$. 86
4.105Nodal mesh analysed with $divL = divD = 12$ and $\lambda = \infty$. 87
4.106Nodal mesh analysed with $divL = divD = 6$ and $\lambda = 10$. 87
4.107Nodal mesh analysed with $divL = divD = 12$ and $\lambda = 10$. 88
4.108Nodal mesh analysed with $divL = divD = 12$ and $\lambda = 10$. 88
4.109Nodal mesh analysed with $divL = divD = 12$ and $\lambda = 10$. 89
4.110Nodal mesh analysed with $divL = divD = 12$ and $\lambda = 10$. 89
4.111Results obtained with the mixed dual method and a regular mesh with $divL = divD = 6$. 90
4.112Results obtained with the mixed dual method and a regular mesh with $divL = divD = 12$. 90
4.113Results obtained with the mixed dual method and a regular mesh with $divL = divD = 24$. 90
4.114Results obtained with the mixed dual method and a regular mesh with $divL = divD = 48$. 91
4.115Results obtained with the mixed dual method and a regular mesh with $divL = divD = 96$. 91
4.116Results obtained with the mixed dual method and an irregular mesh with $divL = divD = 6$. 91
4.117Results obtained with the mixed dual method and an irregular mesh with $divL = divD = 12$. 92
4.118Results obtained with the mixed dual method and an irregular mesh with $divL = divD = 24$. 92

4.119Results obtained with the mixed dual method and an irregular mesh with $divL = divD = 48$. 92
4.120Results obtained with the mixed dual method and an irregular mesh with $divL = divD = 96$. 93
4.121Evolution of the solution as the mesh becomes denser. 93
4.122Evolution of the relative difference as the mesh becomes denser. . . . 94
4.123Reference results over time from the meshless study [2]. 95
4.124Results from the mixed dual method at $t = 2,5$. 96
4.125Results from the mixed dual method at $t = 12,5$. 97
4.126Results from the mixed dual method at $t = 17,5$. 98
4.127Comparison, with reference study, of pressure at $y = 300\,mm$ and $t \approx 17,5\,s$. 99
4.128Comparison, with reference study, of pressure at $x = 300\,mm$ and $t = 0\,s$. 100

5.1 Die model with just one step. 101
5.2 Die model with two steps. 102
5.3 Die model with four steps. 102
5.4 Conical die model. 103
5.5 Reference results from the FEM study [3]. 104
5.6 Results of the first model, with 1 step. 105
5.7 Results of the second model, with 2 steps. 106
5.8 Results of the third model, with 4 steps. 107
5.9 Results of the fourth model, the conical die. 108

List of Tables

4.1 Material properties used in simulation [2], ... 46

5.1 Parameters used for simulation [3, 4], ... 103

Notation

General Notation

a	Scalar
$\boldsymbol{a}$	Vector
$\boldsymbol{A}$	Matrix

Acronyms

2D	Bidimensional
3D	Tridimensional
ABS	Acrylonitrile butadiene styrene
AM	Additive manufacturing
DEM	Diffuse element method
DIY	*Do it yourself*
EFGM	Element free Galerkin method
FDM	Fused deposition modelling
FEM	Finite element method
MFEM	Meshless finite element method
MFS	Method of finite spheres
MLPG	Local Petrov-Galerkin method
MLS	Moving least squares
MQ	Multi-quadric
NEM	Natural element method
NNPRIM	Natural neighbour radial point interpolation method
PAM	Point assembly method
PBF	Polynomial basis function
PIM	Point interpolation method
PLA	Polylactic acid
PVC	Polyvinyl chloride
RBF	Radial basis function
RPIM	Radial point interpolation method
RPKM	Reproducing kernel particle method
SLA	Stereolithography
SPH	Smooth particle hydrodynamics

Symbols

Chapter 2 - Meshless Methods

$\boldsymbol{a}^*$	Vector of coefficients associated with the RBF;
$\boldsymbol{b}$	Vector of external volume forces;
$\boldsymbol{b}^*$	Vector of coefficients associated with the PBF;
$\boldsymbol{B}$	Deformation matrix;
c	RPIM shape function parameter;
$\boldsymbol{D}$	Linear elastic constitutive matrix;
d_{ij}	Component (i,j) of the constitutive matrix;
d_{iI}	Euclidean distance between integration point, I, and node, i;
E	Young's modulus;
f_i	Component of external force on direction i;
$\boldsymbol{f}$	Vector of external nodal forces;
$\boldsymbol{f}_b$	Vector of external volumetric nodal forces;
$\boldsymbol{f}_t$	Vector of external boundary nodal forces;
$\boldsymbol{F}$	Generic matrix function;
$\boldsymbol{K}$	Stiffness matrix;
L	Lagrange functional;
$\boldsymbol{\mathcal{L}}$	Matrix of differential operators;
$\bar{M}_{T(j,i)}$	Component (j,i) of matrix $\boldsymbol{M}_T^{-1}$
$\boldsymbol{M}_T$	Total moment matrix;
n_g	Number of Gauss points;
$\boldsymbol{N}$	Matrix of shape functions;
p	RPIM shape function parameter;
$\boldsymbol{p}$	Vector of polynomial basis functions;
$\boldsymbol{P}$	Matrix of polynomial basis functions;
$\boldsymbol{r}$	Vector of radial basis functions;
$\boldsymbol{R}$	Matrix of radial basis functions;
t	Time variable;
$\boldsymbol{t}$	Vector of external boundary forces;
T	Kinetic energy;
u	Displacement along the x direction;
u^h	Interpolation function of the RPIM;
$\boldsymbol{u}$	Vector of displacements;
$\boldsymbol{u}_s$	Vector of nodal values associated with generic function $\boldsymbol{u}$;
$\tilde{\boldsymbol{u}}$	Vector of nodal displacements;
U	Strain energy;
v	Displacement along the y direction;
w	Displacement along the z direction;
$\bar{w}$	Weight of the Gauss point;
W_f	Work done by external forces;
$\boldsymbol{x}$	Vector of nodal coordinates;
$\boldsymbol{X}$	Set comprised of n nodes;
Γ	Boundary of domain;
δ	Differential increment;

$\boldsymbol{\varepsilon}$	Deformation tensor;
ν	Poisson's coefficient;
ρ	Material's density;
$\boldsymbol{\sigma}$	Cauchy stress tensor;
$\boldsymbol{\phi}$	Vector of shape functions of the RPIM;
Ω	Volume of domain.

Chapter 3 - Flow Formulation

$\boldsymbol{b}$	Vector of external volume forces;
$\boldsymbol{B}$	Deformation matrix;
$\boldsymbol{D}$	Non linear viscoplastic constitutive matrix;
$\boldsymbol{f}$	Vector of external nodal forces;
$\boldsymbol{f}_b$	Vector of external volumetric nodal forces;
$\boldsymbol{f}_t$	Vector of external boundary nodal forces;
$\langle g \rangle$	Function used in the Perzyna viscoplastic model;
h	Parameter concerned with nodal spacing;
$\boldsymbol{I}$	Identity matrix;
$\boldsymbol{I}_d$	Matrix used to compute the deviatoric components of stress and strain rate;
$\boldsymbol{I}_0$	Matrix used to establish stress-strain rate relation in incompressible cases;
$\boldsymbol{I}_1$	Matrix used to establish stress-strain rate relation in compressible cases;
$\boldsymbol{K}_p$	Pressure stiffness matrix of the direct method;
$\boldsymbol{K}_v$	Velocity stiffness matrix;
L	Lagrange functional;
$\boldsymbol{\mathcal{L}}$	Matrix of differential operators;
$\boldsymbol{m}$	Auxiliary vector to compute average components of stress and strain rate;
n	Sensitivity index;
$\boldsymbol{N}_p$	Matrix of pressure shape functions;
$\boldsymbol{N}_v$	Matrix of velocity shape functions;
p	Pressure variable;
$\tilde{\boldsymbol{p}}$	Vector of nodal pressures;
$\boldsymbol{q}$	Vector of hardening parameters;
$\boldsymbol{Q}$	Pressure stiffness matrix of the mixed and mixed dual methods;
t	Time variable;
$\boldsymbol{t}$	Vector of external boundary forces;
$\boldsymbol{u}$	Vector of displacements;
$\boldsymbol{v}$	Vector of velocities;
$\tilde{\boldsymbol{v}}$	Vector of nodal velocities;
Y	Viscoplastic potential of von Mises;
α	Penalty parameter;
γ	Fluidity parameter;
Γ	Boundary of domain;
δ	Differential increment;
ε_{ij}	Linear strain component;
$\dot{\varepsilon}_{ij}$	Linear strain rate component;
$\dot{\varepsilon}_m$	Scalar value of strain rate average;
$\dot{\bar{\varepsilon}}$	Effective strain rate;

$\dot{\boldsymbol{\varepsilon}}$ Strain rate;
$\dot{\boldsymbol{\varepsilon}}_d$ Deviatoric strain rate;
$\dot{\boldsymbol{\varepsilon}}_m$ Average strain rate;
$\dot{\boldsymbol{\varepsilon}}^{vp}$ Viscoplastic strain rate;
λ Randomizer parameter;
μ Non linear material viscosity;
μ_0 Initial non linear viscosity;
σ_y Yield stress;
$\bar{\sigma}$ Effective stress;
$\boldsymbol{\sigma}$ Stress;
$\boldsymbol{\sigma}_d$ Deviatoric stress;
$\boldsymbol{\sigma}_m$ Average stress;
Ω Volume of domain;

Chapter 1

Introduction

In this work, a meshless method, the Radial Point Interpolation Method (RPIM) is used to study the viscoplastic flow of materials in the extrusion process.

Meshless methods are, similarly to the Finite Element Method (FEM), numerical methods used to solve partial differential equations. The importance of numerical techniques grew with the need to solve more complex engineering problems. Such complexity, which could present itself in the form of complex geometry and loading or complex physical phenomena, does in some cases hinder the analytical solution of the governing equations. Therefore, numerical methods are used to simplify the problems in study, either by making some simplifying assumptions on the phenomena or by discretizing and therefore simplifying the geometry.

The FEM was, at this point, extensively proved to be a reliable tool of analysis for a wide variety of engineering problems. In spite its popularity, the method has some limitations by design, which the meshless methods aim to mitigate. Some of these are problems involving complex geometries, large deformations or constant remeshing or updating of nodal coordinates. This is due to the element-based domain discretization used in the FEM which, in the mentioned cases, leads to highly distorted elements prone to portraying wrong results. It was with these limitation in mind that researchers started looking for and developing alternative methods, such as the meshless methods. These methods use a element-free domain discretization, which significantly increases the performance in the problems listed before.

1.1 Meshless methods

The popularity of meshless methods grew exponentially within the last years, especially in the engineering community. These methods have evolved remarkably throughout almost thirty years. It is possible to classify them by three fundamental modules: the field approximation (or interpolation) function, the used formulation and the integration.

In general, the methods can be broadly distinguished as being either approximant or interpolant. There are many approximation, or interpolation functions published today. Some of the most relevant are: the Taylor approximation, the Moving Least-Square (MLS) approximation, the Reducing Kernel approximation and the hp-cloud approximation. While these all lack the delta Kronecker property due to their nature, the ones that follow possess this ability: the polynomial interpolation, the parametric interpolation, the radial interpolation and the Sibson interpolation.

Additionally, meshless methods can be classified in two categories concerning the formulation, a first one that pursues the strong form of the solution and another that seeks the weak form. While the first uses the partial differential equations directly, the latter uses a variational principle to simplify the equations.

As for the integration, the methods are classified as true meshless methods if a point collocation or nodal integration scheme is used. In opposition to this, there are the meshless methods that, contrarily, to denomination, use a background mesh for the integration.

Although, there are methods that date as early as the 70s, such as the Smooth Particle Hydrodynamics (SPH) [5], it wasn't until the creation of the first meshfree approximation schemes that these methods started to gain some popularity. These schemes were based on the Moving Least Squares (MLS) and gave birth to the first meshless method in 1992 named the Diffuse Element Method (DEM) [6]. Although DEM was the first, the most noteworthy MLS-based method ended up to be an extension of the DEM - the Element Free Galerkin Method (EFGM) developed by *Belytschko et al.* circa 1994 [7]. At the same time that the MLS-based methods were being developed, *W. K. Liu et al.* published a method based on the reproducing kernel approximation, the Reproducing Kernel Particle Method (RPKM) [8]. A couple of years later, in 1998, a method was created to solve the lack of the delta Kronecker property, the Natural Element Method (NEM) [9]. Over the course of the next ten years the meshless methods witnessed evolutions in methods such as: the Local Petrov-Galerkin Method (MLPG) [10], which later evolved to the Method of Finite Spheres (MFS) [11], the Point Interpolation Method (PIM) [12], the Point Assembly Method (PAM) [13], the Radial Point Interpolation Method (RPIM) [14], the Meshless Finite Element Method (MFEM) [15] and the Natural Neighbour Radial Point Interpolation Method (NNRPIM) [16].

Althoug many more methods exist, the ones listed above are some of the most important ones. The focus of this work will rely on the method that was first published in 2002 by *G. R. Liu et al.* [14], the RPIM.

1.2 Fused Deposition Modelling

The reasoning behind studying the extrusion process is based on the Additive Manufacturing (AM), most specifically the Fused Deposition Modelling (FDM) process. It is considered that the AM processes had its genesis around 1860s with the photo sculptures and 1890s with topography. The modern day process of Stereolithography (SLA) shares a huge amount of similarities with a process dating back to 1951, the "Photo-glyph recording" [17, 18]. All these were precursors to a technology that would witness its definitive rise in the 21^{st} century.

With the rapid development of the consumer grade market and the *DIY* (do it yourself) maker movement, the AM processes witnessed an enormous growth. Specifically the FDM process, which is most commonly called 3D printing. The FDM process has several stages each one governed by different physical phenomena, involving materials such as PLA or ABS, but several other polymers and composite filaments are already available on the market. The first stage is the extrusion in which a filament of material is pushed through a hot nozzle. The nozzle acts to direct and aid the material flow, since the heat of the nozzle aims to lower the material's viscosity. Afterwards, the flowing polymer makes contact with the extrusion bed and

that constitutes the second phase. In this phase there is relative motion between the bed an the nozzle allowing for the deposition of material in a variety of shapes, ultimately leading to the previously designed 3D component. The third and final phase refers to the bond formation or coalescence of the several layers of extruded material, creating in the end a solid part. In this work, the focus will be in the extrusion part of the process.

The FDM process allows to quickly design, print, prototype or even manufacture a complete product in a relatively short amount of time and without any major investment, as consumer grade 3D printers are getting cheaper by the hour. This helps not only individual makers, designers, engineers and hobbyists but also helps create small businesses and start ups, and even major companies who are looking to push the boundaries of what it is possible to manufacture nowadays. This created a kind of snowball effect in which the market and the technology were feeding in each others growth, continuously. This rapid development raised the awareness of the scientific community, although no efforts to standardize and fundamentally study the phenomenon, lay down design and manufacture guidelines have been made. Consequently, today, it is possible to obtain very different prints in the same printer, using the same 3D file and the same printing parameters. For this reason the importance to study the process grew, as the potential of an optimized FDM process is enormous [17, 18].

Presently, industries such as aeronautics, automotive and biomedical are investing in AM technologies to obtain final components [17, 18]. Not prototypes, but to obtain the finished products. These initiatives, however, require the processes to be more reliable and consistent. Part of this necessary leap in development is concerned with how the machines are manufactured and to define the necessary guidelines, but there is also a big part that is concerned with the physical phenomenon involved in each phase of the process. These are often too complex to study theoretically and that's where simulation and numerical methods comes in to fill in the gap. In this particular case, the numerical methods have the ability to create a big change on how engineers think about design and manufacturing in the future. AM technologies shifted the paradigm by removing geometrical constraints of traditional process without any additional costs. With AM, it is possible to create parts with internal voids and even mechanisms that don't require assembly. Besides drastically reducing costs, it also minimizes the waste that is commonly associated with traditional processes [17, 18].

However, these clear advantages come with challenges needing to be overcome. Most of them are technology related and, in the specific case of FDM there are not sufficient studies related with extrusion or contact problems, documented in the literature, presenting the required level of detail. For this reason, in this work, the focus will be, as already mentioned, the extrusion part of the FDM process although it will be based on the metal forming side of the extrusion process as the literature for this is more abundant. Despite this, the processes are fundamentally the same with minor differences in the constitutive models.

1.3 Flow formulation and numerical methods

In the realm of continuum mechanics, it is possible to trace an imaginary line that divides the materials behaving as solids and others that behave as fluids. It

is only when looking at processes, such as extrusion, that one gets the feeling that the line is not as clear as ideally expected. Extrusion, as a forming process usually deals with hot metals or hot polymers, these are solid materials that are heated to a strategically chosen temperature in order to make them workable in the conditions the process requires. Well, *Zienkiewicz et al.* formulated this problem for the FEM circa 1970s by reasoning that the solid materials would behave has non Newtonian fluids.

This formulation, now conveniently named *flow formulation*, was pioneer in the study of bulk and sheet metal forming processes, such as extrusion, rolling, forging, cutting and deep drawing. Originally intended for the FEM [19, 20], recently it was imported to meshless methods [21, 22, 2] and used extensively to study the same forming process, showing an equal performance, an in some cases a better one. Forming processes are generally associated with big deformations, which constitute an *"Aquilles heel"* of the FEM, so it is no surprise that the more versatile element free meshless methods thrive in these processes.

In this work, the flow formulation will be used to study the viscoplastic extrusion of materials. The main challenge with this lies exactly in the distinction between solid and fluid. While in the realm of metal forming processes, the flow formulation was applied with the intent of studying the velocity/displacement fields and stress fields of the materials. In the extrusion process studied in this work, the focus is not the stress but rather the pressure field, which is more commonly associated with fluids.

1.4 Objectives

The main objective of this work is to lay the foundation to be able to study the polymer extrusion in the FDM process, as well as to be able to connect the extrusion simulation to the simulation of the other phases in the process, aiming to develop an all-in-one FDM simulation package.

Consequently, in this work the goal is to study and understand the flow formulation, its mathematical basis and implementation, study and apply the RPIM to this physical field, implement material laws that would be suitable for a polymer and in the end, create a numerical tool in *Matlab* that is robust, provides confidence in the produced solutions and allows further development.

1.5 Structure

This thesis is organized as follows:

Chapter 2 - Meshless Methods

The general procedure of meshless methods, as well as the foundation of the RPIM are shown. Additionally, it is presented a brief description of the Solid Mechanics fundamentals and linear elastic problems as they help to better understand how the method works and how it performs in preparation for the viscoplastic analysis.

Chapter 3 - Flow Formulation

In this chapter, the mathematical basis of all the analyses and implemented code is elaborated. The equations are presented sequentially for the three versions of the formulation, which resulted from successive attempts. Also, in this section the algorithms associated with the analysis of viscoplastic flow are described for the static and time stepped procedures.

Chapter 4 - Preliminary Results

The concepts and methods defined and explained in the previous chapters are applied, tested and compared to one numerical example from literature. The goal is to test the different versions of the formulation, understand them and find the one that produces the best results. This one is further developed and its parameters are optimized for this type of problem. This validation is performed under the static procedure and, in the end, some time stepped results are shown.

Chapter 5 - Benchmark Results

Another numerical example is programmed to test the methods robustness against different and more complex geometries. The analysis in this chapter uses the method and parameters that were found to be optimal in the previous chapter.

Chapter 6 - Conclusion

In this final chapter, the most important conclusions are discussed and some reflection about future work is carried out.

This page has been intentionally left blank.

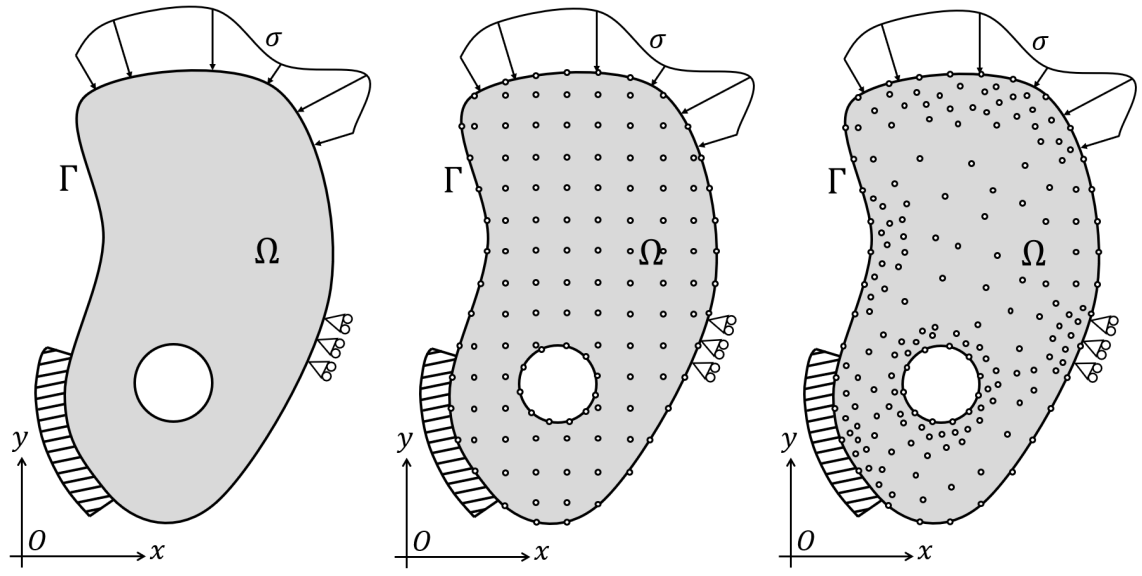
Chapter 2

Meshless Methods

The work developed throughout this thesis was based on the RPIM. For this reason, to more easily apply such technology to the realm of viscoplastic flow of materials, it is necessary to understand the inner workings of the method, not only in what concerns the solid mechanics but also the flow formulation.

2.1 Outline of the General Procedure

Meshless methods are discrete numerical techniques that allow to solve equations, more specifically, partial differential equations. Moreover, meshless methods are nodal dependent methods, i.e., they rely on the nodal discretization of a solid continuous domain (Figure 2.1). Thus, a meshless analysis follows a similar outline as other nodal dependent numerical methods.



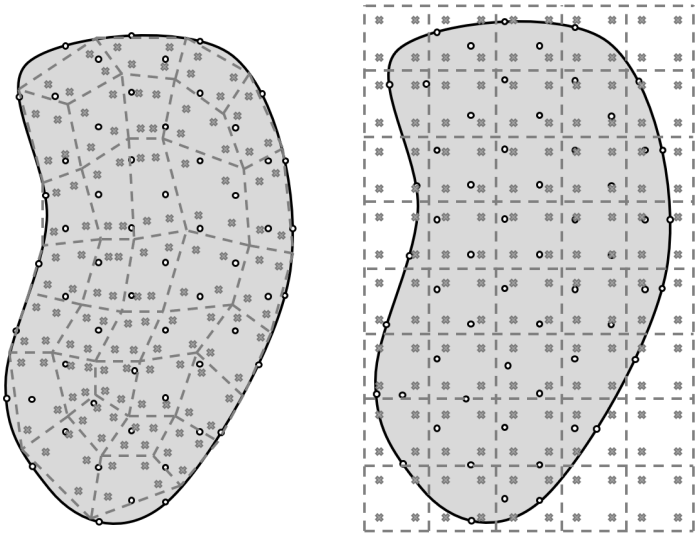
(a) Solid domain. (b) Regular discretization. (c) Irregular discretization.

Figure 2.1: Schematic representation of the nodal discretization of a domain.

Such outline can be described as follows. First, the domain is defined by characterizing the geometry under study, which involves identifying the contour of the domain and its boundaries. Then, the domain is numerically discretized with a set

of nodes, regularly or irregularly distributed, commonly known as nodal discretization. These nodes, despite possible comparisons with the FEM, do not constitute a mesh in the sense that, in true meshless methods, no relationship between nodes is required to construct the shape functions. Despite this, the nodal distribution and density affect the method's performance. As a general rule, a denser mesh will generally lead to more accurate results than a coarser mesh. However, the same can be said for the computational cost, as the finer the mesh the higher the load on the computer running the program. The spatial distribution also plays an important role given that an unbalanced distribution of nodes can lead to lower accuracy. The literature shows that the areas of interest where stress concentrations are to be expected such as: discontinuities, convex boundaries, material interfaces, etc. generally require a higher nodal density as compared to areas where field variable's gradients are less pronounced [1, 23, 24].

After approximating the domain into a set of discrete independent nodes, a background integration mesh is constructed. This background mesh can be either nodal dependent or nodal independent, but in either cases it is required by some methods to properly integrate the weak form equations. These methods that require this background mesh loose the ability to be classified as true meshless, which is the case for RPIM, since it requires one. In this case, it is common to use a Gaussian integration mesh as it is done in the FEM, which can be fitted to problem domain, or it can be larger than the problem domain and the points that are outside it are manually erased (Figure 2.2). An alternative often seen in true meshless methods is the use of Voronoï diagrams, which allows to use the nodes as integration points and to obtain the weight associated with each one. This nodal integration scheme is often associated with a decrease in accuracy, which creates the need for stabilization methods leading to higher computational costs [24].

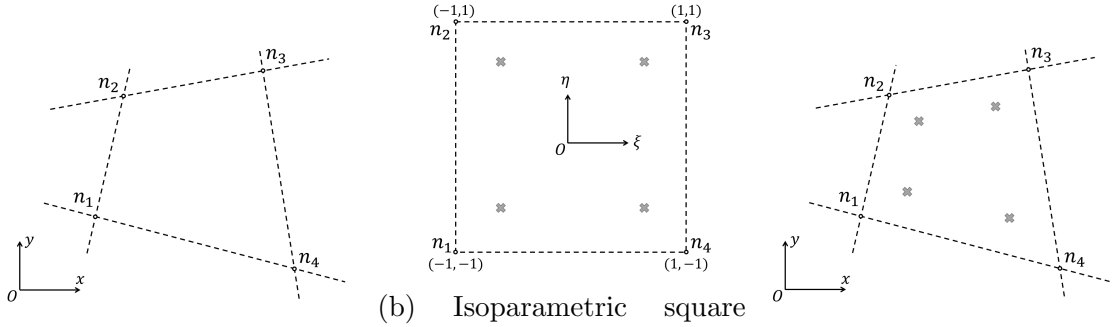


(a) Fitted integration mesh. (b) General integration mesh.

Figure 2.2: Representation of the background integration mesh.

In this work the Gaussian quadrature method, depicted in Figure 2.3, is used. In this approach the solid domain is divided into a grid of quadrilaterals. Each

grid cell is transformed into an isoparametric square and then filled with integration points respecting the Gauss integration procedure, which, based on the number of specified points, determines the coordinates of each point in the natural coordinate system ($O\xi\eta$). Afterwards, using isoparametric interpolation functions the Cartesian coordinates of each integration point is determined. Also, the weight, $\bar{w}$, of the integration point is obtained multiplying the isoparametric weight with the Jacobian matrix determinant of the respective grid cell [24].



(a) Initial quadrilateral. (b) Isoparametric square with 2x2 quadrature scheme. (c) Return to Oxy.

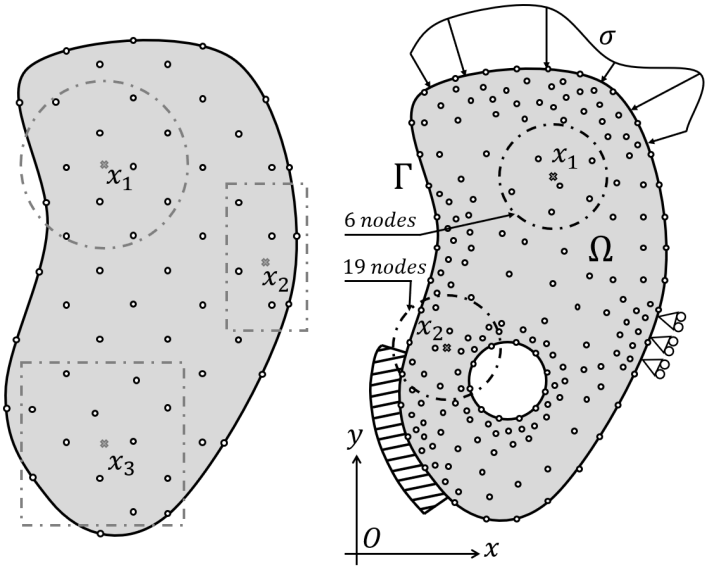
Figure 2.3: Gauss quadrature procedure.

So, the integration of a general function $\boldsymbol{F}(\boldsymbol{x})$ is numerically solved with,

$$\int_{\Omega} \boldsymbol{F}(\boldsymbol{x})\,\mathrm{d}\Omega = \sum_{i=1}^{n_g} \bar{w}_i \boldsymbol{F}(\boldsymbol{x}_i), \tag{2.1}$$

where n_g is the number of integration points.

Having the nodal discretization and the integration mesh sorted out, the method can now establish the nodal connectivity. This property is a default in the FEM due to the element matrix, in which it is based. Lacking the elements, in meshless methods each point of interest has its own influence domain. This point of interest, depending on the integration scheme, can be a integration point if a background mesh is used or a node if the point collocation or nodal integration methodologies are used. In this work, a background mesh was used thus, the points of interest are the integration points. The influence domain is determined by placing concentric areas or volumes in each integration point and the nodes inside each area or volume are said to be within the influence domain of that point. Not only concentric areas or volumes are possible, various shapes of domain can be considered, as shown if Figure 2.4. Now, these areas or volumes can be as big or as small as desired but it is recommended that all influence-domains have the same number of nodes inside, so its size must be dependent on the nodal density on the vicinity of the integration point. A bad example of this is represented in Figure 2.4b where one influence domain has more than double the amount of nodes of the other influence domain. It is also important to note that unlike the FEM, where elements have rigid boundaries and connections between each other and mustn't overlap, in the meshless methods influence domains impose the nodal connectivity with the overlapping of the different influence domains [24].



(a) Different sizes and shapes of influence domains.

(b) Example of bad choice of influence domain size.

Figure 2.4: Representation of the construction of influence domains.

Now that the numerical discretization of the domain is defined, the integration scheme was chosen and the nodes have been imposed a connectivity, the shape functions can be calculated. As mentioned before, meshless methods can be either approximant or interpolant and that classification is determined by the type of shape functions used (approximation or interpolation functions). The RPIM is an interpolation method, as it uses a radial basis function. The interpolation functions have an advantage over the approximation ones because they are null in every node of the influence domain except the node of interest, where it assumes the value of one. This characteristic gives the method the Kronecker delta property, which is handy when imposing constraints [24].

Establishing the equation system is the next step. Depending on the method this can be done applying the shape functions either to the strong or the weak form of the formulation. The strong form is obtained through equilibrium equations that govern the physical phenomenon and the weak form is obtained by using those equations in a variational principle. As in the case of RPIM, a method using the weak form of Galerkin, the discrete equations are obtained using the weighted residual method on the governing equations. The resulting equation are assorted in a local nodal matrix and later assembled into the global matrix for the solution of the global system of equations. In this work, only displacement-based analysis will be performed, which means that the global system of equation will be composed of algebraic equations [24].

The last step in the analysis is to obtain the solution fields. These are obtained with the appropriate solver, in this case an algebraic equation solver that performs a Gauss elimination or LU decomposition methods on the global matrices of the problem [24].

2.2 Radial Point Interpolation Method

As it was mentioned before, the RPIM is a meshless method that leads back to 2002 and it was published by *G. R. Liu et al.* [14]. This method is an evolution of the older PIM, which is also based on point interpolators, the difference being the first uses both polynomial and radial basis functions.

Consider a continuous function $\boldsymbol{u}(\boldsymbol{x})$ which is discretized by an interpolation function $u^h(\boldsymbol{x})$ composed by n nodes of coordinates $\boldsymbol{X} = \{\boldsymbol{x}_1, \boldsymbol{x}_2, ..., \boldsymbol{x}_n\}$. The function, in the RPIM, is made up of a linear combination of a radial basis function (RBF), $r_i(\boldsymbol{x})$, and a polynomial basis function (PBF), $p_i(\boldsymbol{x})$. So, it is possible to define for an integration point $\boldsymbol{x}_I$ the interpolation function as, [24]

$$u^h(\boldsymbol{x}_I) = \sum_{i=1}^{n} r_i(\boldsymbol{x}_I) a_i^*(\boldsymbol{x}_I) + \sum_{j=1}^{m} p_j(\boldsymbol{x}_I) b_j^*(\boldsymbol{x}_I) = \boldsymbol{r}^{\mathrm{T}}(\boldsymbol{x}_I)\boldsymbol{a}^*(\boldsymbol{x}_I) + \boldsymbol{p}^{\mathrm{T}}(\boldsymbol{x}_I)\boldsymbol{b}^*(\boldsymbol{x}_I), \tag{2.2}$$

where m is the number of monomials of the complete polynomial basis, $a_i(\boldsymbol{x}_I)$ and $b_i(\boldsymbol{x}_I)$ are the coefficients of $\boldsymbol{r}(\boldsymbol{x}_I)$ and $\boldsymbol{p}(\boldsymbol{x}_I)$, respectively, and can be defined as,

$$\begin{aligned} \boldsymbol{a}^*(\boldsymbol{x}_I) &= \begin{bmatrix} a_1^*(\boldsymbol{x}_I) & a_2^*(\boldsymbol{x}_I) & ... & a_n^*(\boldsymbol{x}_I) \end{bmatrix}^{\mathrm{T}}, \\ \boldsymbol{b}^*(\boldsymbol{x}_I) &= \begin{bmatrix} b_1^*(\boldsymbol{x}_I) & b_2^*(\boldsymbol{x}_I) & ... & b_m^*(\boldsymbol{x}_I) \end{bmatrix}^{\mathrm{T}}. \end{aligned} \tag{2.3}$$

The PBF, whose monomial terms are given by the Pascal's triangle (Figure 2.5), can be defined as,

$$\boldsymbol{p}(\boldsymbol{x}_I) = \begin{bmatrix} p_1(\boldsymbol{x}_I) & p_2(\boldsymbol{x}_I) & ... & p_m(\boldsymbol{x}_I) \end{bmatrix}^{\mathrm{T}}. \tag{2.4}$$

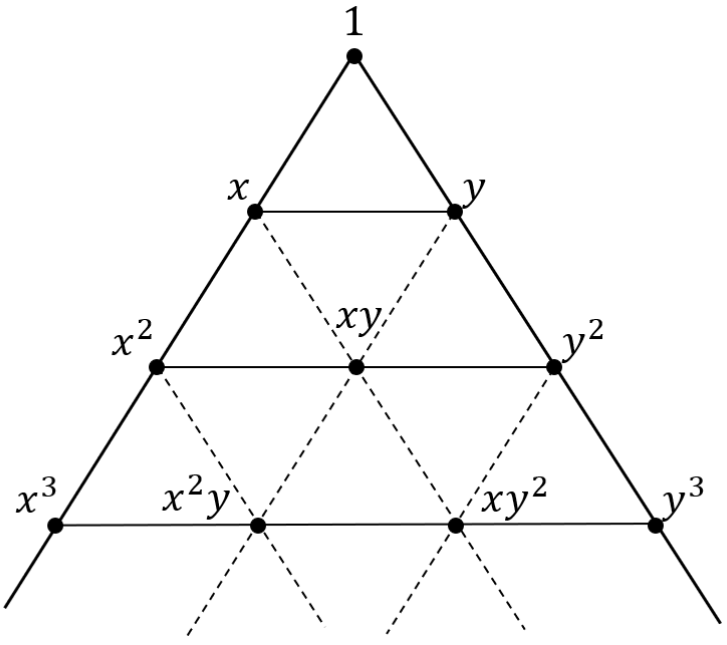


Figure 2.5: Representation of the Pascal's triangle of monomials.

So, if it is assumed that $m = 3$, it is possible to write the PBF vector as,

$$\boldsymbol{p}(\boldsymbol{x}_I) = \begin{bmatrix} 1 & x_I & y_I \end{bmatrix}^{\mathrm{T}}. \tag{2.5}$$

As for the RBF vector, it can be defined as,

$$\begin{aligned} \boldsymbol{r}(\boldsymbol{x}_I) &= \begin{bmatrix} r_1(\boldsymbol{x}_I) & r_2(\boldsymbol{x}_I) & \dots & r_n(\boldsymbol{x}_I) \end{bmatrix}^{\mathrm{T}}, \\ &= \begin{bmatrix} r_1(\boldsymbol{x}_1 - \boldsymbol{x}_I) & r_2(\boldsymbol{x}_2 - \boldsymbol{x}_I) & \dots & r_n(\boldsymbol{x}_n - \boldsymbol{x}_I) \end{bmatrix}^{\mathrm{T}}. \end{aligned} \tag{2.6}$$

There are several RBF documented in literature: the multi-quadrics (MQ), the Gaussian function, the thin plate spline function, etc. The most common one, and the one that was used in this work is the MQ-RBF which is written as,

$$r_i(\boldsymbol{x}_I) = (d_{iI}^2 + c^2)^p, \tag{2.7}$$

where d_{iI} is the euclidean norm between the integration point and the nodes, which can be defined for a two-dimensional space as,

$$d_{iI} = \sqrt{(x_i - x_I)^2 + (y_i - y_I)^2}, \tag{2.8}$$

and c and p are RBF shape parameters which in this work take the following values,

$$\begin{aligned} c &= 0,0001, \\ p &= 0,9999. \end{aligned} \tag{2.9}$$

The coefficients $a_i(\boldsymbol{x}_I)$ and $b_i(\boldsymbol{x}_I)$ have yet to be determined, and for this, a procedure similar to the generic PIM formulation is used. Thus, $u^h(\boldsymbol{x})$ will be forced to pass through all the n nodes of the influence domain of $\boldsymbol{x}_I$. Consequently, equation (2.2) is satisfied for every node in the influence domain. Following this reasoning, the following system of n equations with $n + m$ unknowns is obtained,

$$\begin{cases} u^h(\boldsymbol{x}_1) = \sum_{i=1}^{n} r_i(\boldsymbol{x}_1) a_i^*(\boldsymbol{x}_I) + \sum_{j=1}^{m} p_j(\boldsymbol{x}_1) b_j^*(\boldsymbol{x}_I) = u(\boldsymbol{x}_1), \\ u^h(\boldsymbol{x}_2) = \sum_{i=1}^{n} r_i(\boldsymbol{x}_2) a_i^*(\boldsymbol{x}_I) + \sum_{j=1}^{m} p_j(\boldsymbol{x}_2) b_j^*(\boldsymbol{x}_I) = u(\boldsymbol{x}_2), \\ \vdots \\ u^h(\boldsymbol{x}_n) = \sum_{i=1}^{n} r_i(\boldsymbol{x}_n) a_i^*(\boldsymbol{x}_I) + \sum_{j=1}^{m} p_j(\boldsymbol{x}_n) b_j^*(\boldsymbol{x}_I) = u(\boldsymbol{x}_n). \end{cases} \tag{2.10}$$

In order to obtain a unique solution an extra set of m equations is needed. These come as a consequence of Duchon's theorem and can be written as,

$$\begin{cases} \sum_{i=1}^{n} p_1(\boldsymbol{x}_I) a_i^*(\boldsymbol{x}_I) = 0, \\ \sum_{i=1}^{n} p_2(\boldsymbol{x}_I) a_i^*(\boldsymbol{x}_I) = 0, \\ \vdots \\ \sum_{i=1}^{n} p_m(\boldsymbol{x}_I) a_i^*(\boldsymbol{x}_I) = 0. \end{cases} \tag{2.11}$$

Adopting matrix notation, these equations become,

$$\begin{aligned} \boldsymbol{R}\boldsymbol{a}^*(\boldsymbol{x}_I) + \boldsymbol{P}\boldsymbol{b}^*(\boldsymbol{x}_I) &= \boldsymbol{u}_s, \\ \boldsymbol{P}^{\mathrm{T}}\boldsymbol{a}^*(\boldsymbol{x}_I) &= \boldsymbol{0}, \end{aligned} \tag{2.12}$$

where $\boldsymbol{u}_s$ is the vector containing the nodal parameters of the field function for each node inside the influence domain. The generic moment matrix, $\boldsymbol{R}$, is defined as,

$$\boldsymbol{R} = \begin{bmatrix} r_1(\boldsymbol{x}_1) & r_2(\boldsymbol{x}_1) & \cdots & r_n(\boldsymbol{x}_1) \\ r_1(\boldsymbol{x}_2) & r_2(\boldsymbol{x}_2) & \cdots & r_n(\boldsymbol{x}_2) \\ \vdots & \vdots & \ddots & \vdots \\ r_1(\boldsymbol{x}_n) & r_2(\boldsymbol{x}_n) & \cdots & r_n(\boldsymbol{x}_n) \end{bmatrix}. \tag{2.13}$$

Similarly, the polynomial moment matrix, $\boldsymbol{P}$, is given by,

$$\boldsymbol{P} = \begin{bmatrix} p_1(\boldsymbol{x}_1) & p_2(\boldsymbol{x}_1) & \cdots & p_m(\boldsymbol{x}_1) \\ p_1(\boldsymbol{x}_2) & p_2(\boldsymbol{x}_2) & \cdots & p_m(\boldsymbol{x}_2) \\ \vdots & \vdots & \ddots & \vdots \\ p_1(\boldsymbol{x}_n) & p_2(\boldsymbol{x}_n) & \cdots & p_m(\boldsymbol{x}_n) \end{bmatrix}. \tag{2.14}$$

Following the example above with $m = 3$ in 2D space, it is then obtained

$$\boldsymbol{P} = \begin{bmatrix} 1 & x_1 & y_1 \\ 1 & x_2 & y_2 \\ \vdots & \vdots & \vdots \\ 1 & x_n & y_n \end{bmatrix}. \tag{2.15}$$

Writing equation (2.12) in matrix form,

$$\begin{bmatrix} \boldsymbol{R} & \boldsymbol{P} \\ \boldsymbol{P}^{\mathrm{T}} & \boldsymbol{0} \end{bmatrix} \begin{bmatrix} \boldsymbol{a}^*(\boldsymbol{x}_I) \\ \boldsymbol{b}^*(\boldsymbol{x}_I) \end{bmatrix} = \boldsymbol{M}_T \begin{bmatrix} \boldsymbol{a}^*(\boldsymbol{x}_I) \\ \boldsymbol{b}^*(\boldsymbol{x}_I) \end{bmatrix} = \begin{bmatrix} \boldsymbol{u}_s \\ \boldsymbol{0} \end{bmatrix}. \tag{2.16}$$

Matrices $\boldsymbol{R}$ and $\boldsymbol{P}$ are symmetrical, thus, the total moment matrix, $\boldsymbol{M}_T$, is also symmetric. Now, by inverting it is possible to obtain the coefficients,

$$\begin{bmatrix} \boldsymbol{a}^*(\boldsymbol{x}_I) \\ \boldsymbol{b}^*(\boldsymbol{x}_I) \end{bmatrix} = \boldsymbol{M}_T^{-1} \begin{bmatrix} \boldsymbol{u}_s \\ \boldsymbol{0} \end{bmatrix}. \tag{2.17}$$

Substituting the newly found coefficients in equation (2.2) it yields,

$$u^h(\boldsymbol{x}_I) = \begin{bmatrix} \boldsymbol{r}(\boldsymbol{x}_I)^{\mathrm{T}} & \boldsymbol{p}(\boldsymbol{x}_I)^{\mathrm{T}} \end{bmatrix} \begin{bmatrix} \boldsymbol{a}^*(\boldsymbol{x}_I) \\ \boldsymbol{b}^*(\boldsymbol{x}_I) \end{bmatrix} = \begin{bmatrix} \boldsymbol{r}(\boldsymbol{x}_I)^{\mathrm{T}} & \boldsymbol{p}(\boldsymbol{x}_I)^{\mathrm{T}} \end{bmatrix} \boldsymbol{M}_T^{-1} \begin{bmatrix} \boldsymbol{u}_s \\ \boldsymbol{0} \end{bmatrix}. \tag{2.18}$$

Defining the shape function vector, $\boldsymbol{\phi}(\boldsymbol{x}_I)$, such that,

$$u^h(\boldsymbol{x}_I) = \sum_{i=1}^{n} \phi_i(\boldsymbol{x}_I) u_i = \boldsymbol{\phi}(\boldsymbol{x}_I)^{\mathrm{T}} \boldsymbol{u}_s, \tag{2.19}$$

it is possible to now relate the shape function vector with equation (2.18), as follows,

$$\begin{bmatrix} \boldsymbol{r}(\boldsymbol{x}_I)^{\mathrm{T}} & \boldsymbol{p}(\boldsymbol{x}_I)^{\mathrm{T}} \end{bmatrix} \boldsymbol{M}_T^{-1} \begin{bmatrix} \boldsymbol{u}_s \\ \boldsymbol{0} \end{bmatrix} = \boldsymbol{\phi}(\boldsymbol{x}_I)^{\mathrm{T}} \boldsymbol{u}_s, \tag{2.20}$$

where the vector $\boldsymbol{\phi}(\boldsymbol{x}_I)$ is given by,

$$\boldsymbol{\phi}(\boldsymbol{x}_I) = \begin{bmatrix} \phi_1(\boldsymbol{x}_I) & \phi_2(\boldsymbol{x}_I) & \cdots & \phi_n(\boldsymbol{x}_I) \end{bmatrix}, \tag{2.21}$$

in which [24, 14],

$$\phi_i(\boldsymbol{x}_I) = \sum_{j=1}^{n} r_j(\boldsymbol{x}_I)\bar{M}_{T(j,i)} + \sum_{k=1}^{m} p_k(\boldsymbol{x}_I)\bar{M}_{T(n+k,i)}, \tag{2.22}$$

where $\bar{M}_{T(j,i)}$ is the (j,i) element of matrix $\boldsymbol{M}_T^{-1}$. Once this inverse matrix is obtained, the derivatives of the shape functions are easily obtained as [24, 14]:

$$\begin{aligned} \frac{\partial \phi_i}{\partial x} &= \sum_{j=1}^{n} \frac{\partial r_j}{\partial x}\bar{M}_{T(j,i)} + \sum_{k=1}^{m} \frac{\partial p_k}{\partial x}\bar{M}_{T(n+k,i)}, \\ \frac{\partial \phi_i}{\partial y} &= \sum_{j=1}^{n} \frac{\partial r_j}{\partial y}\bar{M}_{T(j,i)} + \sum_{k=1}^{m} \frac{\partial p_k}{\partial y}\bar{M}_{T(n+k,i)}. \end{aligned} \tag{2.23}$$

2.2.1 Properties of the RBF Shape Functions

Following the mathematical description of the previous pages, it becomes apparent that after the calculation of the basis functions, the shape functions, $\phi_i(\boldsymbol{x}_I)$, depend exclusively on the distribution of nodes used to discretize the domain. These functions have some important properties which deserve mentioning [24, 14]:

1. The RPIM shape functions are linearly independent in each influence domain;
2. The RPIM shape functions possess the Kronecker delta property,

$$\phi_i(\boldsymbol{x} = \boldsymbol{x}_j) = \begin{cases} 1, & i = j \\ 0, & i \neq \end{cases}; \tag{2.24}$$

3. The RPIM shape functions possess the partition of unity property,

$$\sum_{i=1}^{n} \phi_i(\boldsymbol{x}) = 1; \tag{2.25}$$

4. The RPIM shape functions have reproducing properties, which means that any functional included in the basis of the RPIM shape function can be exactly reproduced by the RPIM approximation;
5. The RPIM shape functions have compact support since its value is zero for any node outside the influence domain.

2.3 Linear Elasticity with RPIM

The main focus of this work is the non-linear viscoplastic flow of materials using the RPIM, which is a highly demanding and complicated subject. For this reason it is important to gain some degree of familiarity with the method with a simpler more well-known problem: two dimensional linear elasticity. Thus, in this section a brief introduction is made to solid mechanics, as well as some 2D linear elastic examples are discussed.

2.3.1 Solid Mechanics Fundamentals

When a solid body is acted upon by an external force, a stress field develops in this body. Also, these forces can cause the body to change shape, i.e., to deform. In this case, a strain field develops in the body. Solid mechanics is the field of mechanics that studies and relates these physical quantities, stress and strains in solid bodies.

Stress

In a 3D stress state there are six independent stress components and nine in total. These can be arranged in a symmetric matrix, called the Cauchy stress tensor,

$$\boldsymbol{\sigma} = \begin{bmatrix} \sigma_{xx} & \tau_{xy} & \tau_{xz} \\ \tau_{yx} & \sigma_{yy} & \tau_{yz} \\ \tau_{zx} & \tau_{zy} & \sigma_{zz} \end{bmatrix}, \tag{2.26}$$

where σ_{ij} represents a normal stress component and τ_{ij} a shear stress component.

In a body subjected to an arbitrary system of forces - can be volume or surface loads - the stress field must ensure the equilibrium of the body as whole or a single part by itself. Thus, by analysing an infinitesimal element of volume one can deduce these equilibrium equations,

$$\begin{aligned} \frac{\partial \sigma_{xx}}{\partial x} + \frac{\partial \tau_{xy}}{\partial y} + \frac{\partial \tau_{xz}}{\partial z} + f_x = 0, \\ \frac{\partial \tau_{yx}}{\partial x} + \frac{\partial \sigma_{yy}}{\partial y} + \frac{\partial \tau_{yz}}{\partial z} + f_y = 0, \\ \frac{\partial \tau_{zx}}{\partial x} + \frac{\partial \tau_{zy}}{\partial y} + \frac{\partial \sigma_{zz}}{\partial z} + f_z = 0. \end{aligned} \tag{2.27}$$

Strain

In a 3D problem there are also six independent strain components and nine in total which can be arranged in a matrix, similarly to what was done with the stresses, called the the strain tensor,

$$\boldsymbol{\varepsilon} = \begin{bmatrix} \varepsilon_{xx} & \frac{1}{2}\gamma_{xy} & \frac{1}{2}\gamma_{xz} \\ \frac{1}{2}\gamma_{yx} & \varepsilon_{yy} & \frac{1}{2}\gamma_{yz} \\ \frac{1}{2}\gamma_{zx} & \frac{1}{2}\gamma_{zy} & \varepsilon_{zz} \end{bmatrix}, \tag{2.28}$$

where ε_{ij} represents a normal strain component and γ_{ij} a shear strain component.

Strain is the result of deformation of the body. When deformation occurs there is relative motion between the points in the body, therefore each strain component can be defined as a function of the displacement,

$$\begin{aligned} \varepsilon_{xx} &= \frac{\partial u}{\partial x} \quad \gamma_{xy} = \frac{\partial u}{\partial y} + \frac{\partial v}{\partial x}, \\ \varepsilon_{yy} &= \frac{\partial v}{\partial y} \quad \gamma_{yz} = \frac{\partial v}{\partial z} + \frac{\partial w}{\partial y}, \\ \varepsilon_{zz} &= \frac{\partial w}{\partial z} \quad \gamma_{zx} = \frac{\partial w}{\partial x} + \frac{\partial u}{\partial z}. \end{aligned} \tag{2.29}$$

or simply,

$$\boldsymbol{\varepsilon} = \boldsymbol{\mathcal{L}} \boldsymbol{u}, \tag{2.30}$$

where $\boldsymbol{\varepsilon}$, $\boldsymbol{\mathcal{L}}$ and $\boldsymbol{u}$ are given by,

$$\boldsymbol{\varepsilon} = \begin{bmatrix} \varepsilon_{xx} \\ \varepsilon_{yy} \\ \varepsilon_{zz} \\ \gamma_{xy} \\ \gamma_{yz} \\ \gamma_{zx} \end{bmatrix} \quad , \quad \boldsymbol{\mathcal{L}} = \begin{bmatrix} \frac{\partial}{\partial x} & 0 & 0 \\ 0 & \frac{\partial}{\partial y} & 0 \\ 0 & 0 & \frac{\partial}{\partial z} \\ \frac{\partial}{\partial y} & \frac{\partial}{\partial x} & 0 \\ 0 & \frac{\partial}{\partial z} & \frac{\partial}{\partial y} \\ \frac{\partial}{\partial z} & 0 & \frac{\partial}{\partial x} \end{bmatrix} \quad , \quad \boldsymbol{u} = \begin{bmatrix} u \\ v \\ w \end{bmatrix}. \tag{2.31}$$

2D Problems

In 2D problems there are two types of stress states:

Plane stress When the thickness of the body is much smaller than the other two dimensions and all the loading is contained in the midplane of the body, the plane stress state can be assumed. In which,

$$\sigma_{zz} = \tau_{xz} = \tau_{yz} = 0. \tag{2.32}$$

Plane strain When the thickness of the body is much larger than the other two dimensions and the loading is uniform along the longitudinal axis of the body, the plain strain state can be assumed. In which,

$$\varepsilon_{zz} = \gamma_{xz} = \gamma_{yz} = 0. \tag{2.33}$$

Constitutive Equations

In general, in this work only isotropic materials will be used. These materials are characterized for having directional independent material properties. They are the same regardless of the direction of loading. Also, in this section only materials governed by linear elastic constitutive equations, in this case, by the Hooke's law, are considered. Thus, it is possible to write,

$$\boldsymbol{\sigma} = \boldsymbol{D}\boldsymbol{\varepsilon}. \tag{2.34}$$

In 2D problems specifically, the matrix $\boldsymbol{D}$ can take the following form,

$$\boldsymbol{D} = \begin{bmatrix} d_{11} & d_{12} & 0 \\ d_{21} & d_{22} & 0 \\ 0 & 0 & d_{33} \end{bmatrix}, \tag{2.35}$$

where in plane stress $\boldsymbol{D}$ assumes the form of,

$$\boldsymbol{D} = \frac{E}{1-\nu^2} \begin{bmatrix} 1 & \nu & 0 \\ \nu & 1 & 0 \\ 0 & 0 & \frac{1-\nu}{2} \end{bmatrix}, \tag{2.36}$$

and, in plane strain $\boldsymbol{D}$ is represented as,

$$\boldsymbol{D} = \frac{E}{(1+\nu)(1-2\nu)} \begin{bmatrix} 1-\nu & \nu & 0 \\ \nu & 1-\nu & 0 \\ 0 & 0 & \frac{1-2\nu}{2} \end{bmatrix}. \tag{2.37}$$

2.3.2 Galerkin Weak Form

To obtain the discrete equations the weak form of Galerkin will be used. This is a variational principle based on the energy principle, that states that, of all possible displacement configurations satisfying the compatibility conditions, the essential boundary conditions (either kinematic or displacement) and the initial and final conditions, the real solution's configuration is the one which minimizes the Lagrangian functional L,

$$L = T - U + W_f, \tag{2.38}$$

being T the kinetic energy, U the strain energy and W_f the work produced by the external forces. The kinetic energy is defined by,

$$T = \frac{1}{2}\int_\Omega \rho \dot{\boldsymbol{u}}^{\mathrm{T}} \dot{\boldsymbol{u}}\, \mathrm{d}\Omega, \tag{2.39}$$

the strain energy is given by,

$$U = \frac{1}{2}\int_\Omega \boldsymbol{\varepsilon}^{\mathrm{T}} \boldsymbol{\sigma}\, \mathrm{d}\Omega, \tag{2.40}$$

and the work of the external forces is,

$$W_f = \int_\Omega \boldsymbol{u}^{\mathrm{T}} \boldsymbol{b}\, \mathrm{d}\Omega + \int_\Gamma \boldsymbol{u}^{\mathrm{T}} \boldsymbol{t}\, \mathrm{d}\Gamma, \tag{2.41}$$

where Ω represents the volume of the domain, Γ the area of the surface or boundary of the domain, $\boldsymbol{u}$ the displacement field, $\dot{\boldsymbol{u}}$ the first derivative of the displacement field, $\boldsymbol{b}$ the vector of body forces and $\boldsymbol{t}$ the vector of boundary forces. Thus, rewriting the Lagrangian functional, equation (2.38) yields,

$$L = \frac{1}{2}\int_\Omega \rho \dot{\boldsymbol{u}}^{\mathrm{T}} \dot{\boldsymbol{u}}\, \mathrm{d}\Omega - \frac{1}{2}\int_\Omega \boldsymbol{\varepsilon}^{\mathrm{T}} \boldsymbol{\sigma}\, \mathrm{d}\Omega + \int_\Omega \boldsymbol{u}^{\mathrm{T}} \boldsymbol{b}\, \mathrm{d}\Omega + \int_\Gamma \boldsymbol{u}^{\mathrm{T}} \boldsymbol{t}\, \mathrm{d}\Gamma. \tag{2.42}$$

In static analysis the velocity is neglected and consequently the term of the kinetic energy is not considered,

$$L = -\frac{1}{2}\int_\Omega \boldsymbol{\varepsilon}^{\mathrm{T}} \boldsymbol{\sigma}\, \mathrm{d}\Omega + \int_\Omega \boldsymbol{u}^{\mathrm{T}} \boldsymbol{b}\, \mathrm{d}\Omega + \int_\Gamma \boldsymbol{u}^{\mathrm{T}} \boldsymbol{t}\, \mathrm{d}\Gamma. \tag{2.43}$$

Minimizing the Lagrange functional,

$$\begin{aligned} \delta \int_{t_1}^{t_2} \left[-\frac{1}{2}\int_\Omega \boldsymbol{\varepsilon}^{\mathrm{T}} \boldsymbol{\sigma}\, \mathrm{d}\Omega + \int_\Omega \boldsymbol{u}^{\mathrm{T}} \boldsymbol{b}\, \mathrm{d}\Omega + \int_\Gamma \boldsymbol{u}^{\mathrm{T}} \boldsymbol{t}\, \mathrm{d}\Gamma \right] \mathrm{d}t = 0, \\ \int_{t_1}^{t_2} \left[-\frac{1}{2}\int_\Omega \delta\left(\boldsymbol{\varepsilon}^{\mathrm{T}} \boldsymbol{\sigma}\right)\, \mathrm{d}\Omega + \int_\Omega \delta\boldsymbol{u}^{\mathrm{T}} \boldsymbol{b}\, \mathrm{d}\Omega + \int_\Gamma \delta\boldsymbol{u}^{\mathrm{T}} \boldsymbol{t}\, \mathrm{d}\Gamma \right] \mathrm{d}t = 0. \end{aligned} \tag{2.44}$$

For an integral to be null the same has to be verified for its integrand, thus,

$$\frac{1}{2}\int_\Omega \delta\left(\boldsymbol{\varepsilon}^{\mathrm{T}} \boldsymbol{\sigma}\right)\, \mathrm{d}\Omega - \int_\Omega \delta\boldsymbol{u}^{\mathrm{T}} \boldsymbol{b}\, \mathrm{d}\Omega - \int_\Gamma \delta\boldsymbol{u}^{\mathrm{T}} \boldsymbol{t}\, \mathrm{d}\Gamma = 0. \tag{2.45}$$

Looking only at the first term of equation (2.45) it is possible to write,

$$\delta\left(\boldsymbol{\varepsilon}^{\mathrm{T}}\boldsymbol{\sigma}\right) = \delta\boldsymbol{\varepsilon}^{\mathrm{T}}\boldsymbol{\sigma} + \boldsymbol{\varepsilon}^{\mathrm{T}}\delta\boldsymbol{\sigma}. \tag{2.46}$$

Now, adopting a constitutive equation of the form $\boldsymbol{\sigma} = \boldsymbol{D}\boldsymbol{\varepsilon}$ with the material matrix being symmetric, i.e., $\boldsymbol{D}^{\mathrm{T}} = \boldsymbol{D}$, it yields,

$$\delta\boldsymbol{\varepsilon}^{\mathrm{T}}\boldsymbol{\sigma} = \delta\boldsymbol{\varepsilon}^{\mathrm{T}}\boldsymbol{D}\boldsymbol{\varepsilon} = \delta\boldsymbol{\varepsilon}^{\mathrm{T}}\boldsymbol{D}^{\mathrm{T}}\boldsymbol{\varepsilon} = \delta\left(\boldsymbol{D}\boldsymbol{\varepsilon}\right)^{\mathrm{T}}\boldsymbol{\varepsilon} = \delta\boldsymbol{\sigma}^{\mathrm{T}}\boldsymbol{\varepsilon}. \tag{2.47}$$

This term is in fact a scalar so the transpose does not affect the result, thus,

$$\delta\boldsymbol{\sigma}^{\mathrm{T}}\boldsymbol{\varepsilon} = \left(\delta\boldsymbol{\sigma}^{\mathrm{T}}\boldsymbol{\varepsilon}\right)^{\mathrm{T}} = \boldsymbol{\varepsilon}^{\mathrm{T}}\delta\boldsymbol{\sigma} \;\rightarrow\; \boldsymbol{\varepsilon}^{\mathrm{T}}\delta\boldsymbol{\sigma} = \delta\boldsymbol{\varepsilon}^{\mathrm{T}}\boldsymbol{\sigma}. \tag{2.48}$$

Substituting in equation (2.46) results in,

$$\delta\left(\boldsymbol{\varepsilon}^{\mathrm{T}}\boldsymbol{\sigma}\right) = 2\delta\boldsymbol{\varepsilon}^{\mathrm{T}}\boldsymbol{\sigma}. \tag{2.49}$$

Which ultimately, having equation (2.45) in mind, leads to the following,

$$\int_{\Omega}\delta\boldsymbol{\varepsilon}^{\mathrm{T}}\boldsymbol{\sigma}\,\mathrm{d}\Omega - \int_{\Omega}\delta\boldsymbol{u}^{\mathrm{T}}\boldsymbol{b}\,\mathrm{d}\Omega - \int_{\Gamma}\delta\boldsymbol{u}^{\mathrm{T}}\boldsymbol{t}\,\mathrm{d}\Gamma = 0. \tag{2.50}$$

2.3.3 Discrete Equations

The vector of nodal displacements can be defined as,

$$\tilde{\boldsymbol{u}} = \begin{bmatrix}\tilde{u}_1 & \tilde{v}_1 & \tilde{u}_2 & \tilde{v}_2 & \cdots & \tilde{u}_n & \tilde{u}_n\end{bmatrix}^{\mathrm{T}}, \tag{2.51}$$

where the tilde in the notation denotes that the vector in question is associated with nodal values. The displacement in an interest point can, therefore, be given by,

$$\boldsymbol{u} = \begin{bmatrix}u\\ v\end{bmatrix} = \boldsymbol{N}\tilde{\boldsymbol{u}}, \tag{2.52}$$

where the matrix of shape functions, $\boldsymbol{N}$, is given by,

$$\boldsymbol{N} = \begin{bmatrix}N_1 & 0 & N_2 & 0 & \cdots & N_n & 0\\ 0 & N_1 & 0 & N_2 & \cdots & 0 & N_n\end{bmatrix}. \tag{2.53}$$

In 2D the the strain operator matrix defined in equation (2.31) becomes,

$$\boldsymbol{\mathcal{L}} = \begin{bmatrix}\frac{\partial}{\partial x} & 0\\ 0 & \frac{\partial}{\partial y}\\ \frac{\partial}{\partial y} & \frac{\partial}{\partial x}\end{bmatrix}. \tag{2.54}$$

This allows to write the following,

$$\boldsymbol{\varepsilon} = \boldsymbol{\mathcal{L}}\boldsymbol{u} = \boldsymbol{\mathcal{L}}\boldsymbol{N}\tilde{\boldsymbol{u}} = \boldsymbol{B}\tilde{\boldsymbol{u}}, \tag{2.55}$$

with $\boldsymbol{B}$ being,

$$\boldsymbol{B} = \begin{bmatrix}\boldsymbol{B}_1 & \boldsymbol{B}_2 & \cdots & \boldsymbol{B}_n\end{bmatrix},\ \boldsymbol{B}_i = \begin{bmatrix}\frac{\partial N_i}{\partial x} & 0\\ 0 & \frac{\partial N_i}{\partial y}\\ \frac{\partial N_i}{\partial y} & \frac{\partial N_i}{\partial x}\end{bmatrix}. \tag{2.56}$$

Recalling equation (2.34), it is possible to write,

$$\boldsymbol{\sigma} = \boldsymbol{D}\boldsymbol{\varepsilon} = \boldsymbol{D}\boldsymbol{B}\tilde{\boldsymbol{u}}. \tag{2.57}$$

Introducing equations (2.52), (2.55) and (2.57) into (2.50) yields,

$$\int_{\Omega} \delta\tilde{\boldsymbol{u}}^{\mathrm{T}}\boldsymbol{B}^{\mathrm{T}}\boldsymbol{D}\boldsymbol{B}\tilde{\boldsymbol{u}}\,\mathrm{d}\Omega - \int_{\Omega} \delta\tilde{\boldsymbol{u}}^{\mathrm{T}}\boldsymbol{N}\boldsymbol{b}\,\mathrm{d}\Omega - \int_{\Gamma} \delta\tilde{\boldsymbol{u}}^{\mathrm{T}}\boldsymbol{N}\boldsymbol{t}\,\mathrm{d}\Gamma = 0. \tag{2.58}$$

The terms concerning nodal values, the ones with the tilde, are independent from the integral variables and consequently it is possible to write,

$$\delta\tilde{\boldsymbol{u}}^{\mathrm{T}}\left(\int_{\Omega} \boldsymbol{B}^{\mathrm{T}}\boldsymbol{D}\boldsymbol{B}\,\mathrm{d}\Omega\,\tilde{\boldsymbol{u}} - \int_{\Omega} \boldsymbol{N}\boldsymbol{b}\,\mathrm{d}\Omega - \int_{\Gamma} \boldsymbol{N}\boldsymbol{t}\,\mathrm{d}\Gamma\right) = 0, \tag{2.59}$$

or simply,

$$\int_{\Omega} \boldsymbol{B}^{\mathrm{T}}\boldsymbol{D}\boldsymbol{B}\,\mathrm{d}\Omega\,\tilde{\boldsymbol{u}} - \int_{\Omega} \boldsymbol{N}\boldsymbol{b}\,\mathrm{d}\Omega - \int_{\Gamma} \boldsymbol{N}\boldsymbol{t}\,\mathrm{d}\Gamma = 0. \tag{2.60}$$

Equation (2.60) constitutes the weak form of the governing equations for a simple liner elastic problem. It can be written in matrix form as,

$$\boldsymbol{K}\tilde{\boldsymbol{u}} = \boldsymbol{f}, \tag{2.61}$$

where the stiffness matrix, $\boldsymbol{K}$, and the external forces vector, $\boldsymbol{f}$, are given by,

$$\begin{aligned} \boldsymbol{K} &= \int_{\Omega} \boldsymbol{B}^{\mathrm{T}}\boldsymbol{D}\boldsymbol{B}\,\mathrm{d}\Omega, \\ \boldsymbol{f} &= \boldsymbol{f}_b + \boldsymbol{f}_t = \int_{\Omega} \boldsymbol{N}\boldsymbol{b}\,\mathrm{d}\Omega + \int_{\Gamma} \boldsymbol{N}\boldsymbol{t}\,\mathrm{d}\Gamma. \end{aligned} \tag{2.62}$$

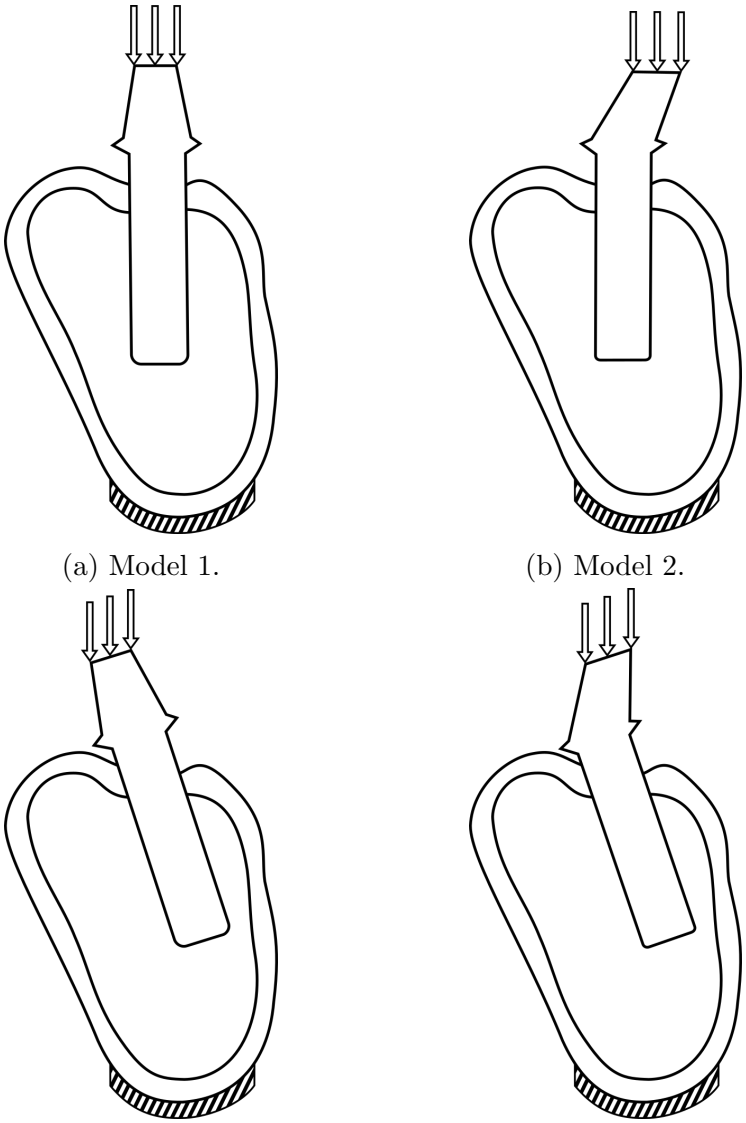
To obtain the solution for the displacement field, the system of algebraic equations needs solving and for this, one must invert the stiffness matrix,

$$\tilde{\boldsymbol{u}} = \boldsymbol{K}^{-1}\boldsymbol{f}. \tag{2.63}$$

2.3.4 2D Linear Elastic Examples

As a first contact with meshless methods and the RPIM, specifically, some research work in the scope of the thesis was done. This research focused heavily on biomechanics and how meshless methods could be an improvement over the FEM. More often than not, the research work relied on comparing the methods performance, as such, the example that will be described in this section is concerned with dentistry implants and how the RPIM and the FEM perform in this type of problem.

The example is based on a 3D FEM study performed by *Tian et al.* [25] in which two 3D models of implants were analysed. Since the goal of the study was to comprehend the relationship between the stress distribution on the implant and the bone tissues surrounding the implant, the models were analysed in two different positions, producing in the end a total of four numerical models. These models can be observed, schematically, in their 2D version in Figure 2.6.



(a) Model 1. (b) Model 2.

(c) Model 3. (d) Model 4.

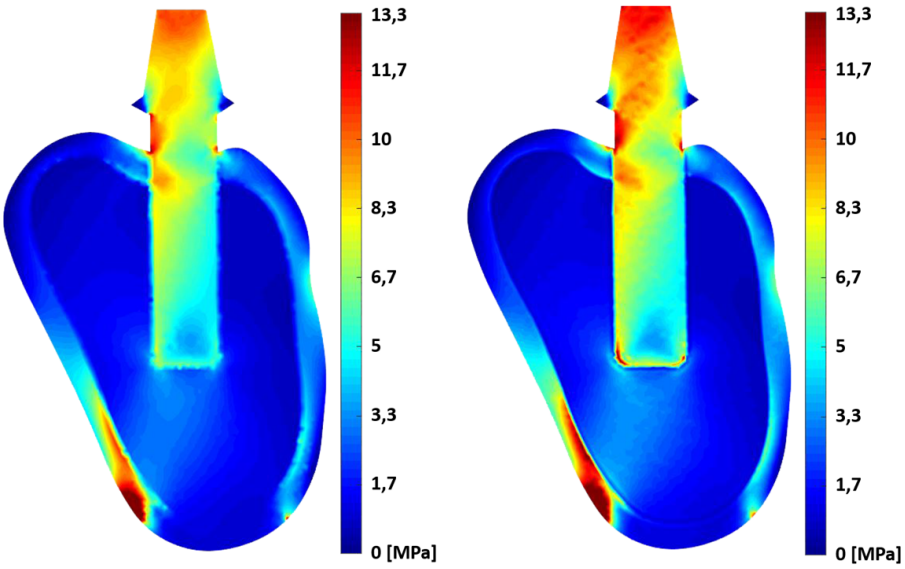
Figure 2.6: Schematic representation of the four models studied.

The two implants - whose base is 4 mm in diameter and 14 mm in height - differed from one another at the abutment part. Although both were similar in size - height 5 mm and top diameter of 3 mm - one had a straight abutment (models 1 and 3) and the other had and abutment possessing a 20° angle with its axis (models 2 and 4). These two feature classic implant geometry that is available to dentists, and the use of one or the other has to do with clinical practice and the specific case of the patient. This clinical constraint is also the reason to study both implants in a skewed position (70° with the vertical axis). Some patients may not have a bone tissue structure that allows for the upright configuration (models 1 and 2) and the dentist may than opt to insert these implants with a slight angle (models 3 and 4).

The FEM study aimed at understanding whether this angle plays a significant role in the stress field to change how the implant interacts with the bone tissue in the every-day lives of the patients. For this, a standard vertical occlusal load, that is, the load that occurs when the occlusal surfaces of the top and bottom teeth contact (for example when chewing), was considered. This load had a magnitude of 100 N. The

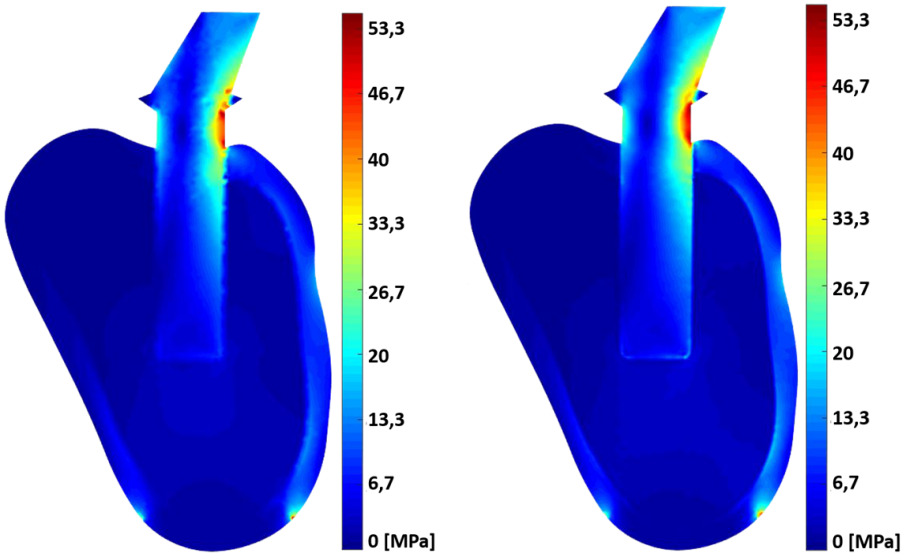
implant and abutment were considered to be a titanium alloy ($E = 110000\,\text{MPa}$ and $\nu = 0,3$) and, also, a cortical layer ($E = 13700\,\text{MPa}$ and $\nu = 0,3$) and a trabecular layer ($E = 1370\,\text{MPa}$ and $\nu = 0,3$) were considered in the bone structure.

In this study, due to the lack of clinical knowledge, it is not the clinical benefits or insights that will be the focus, but rather the way the RPIM approach fairs up against the FEM. Thus, it will be compared a 2D FEM and RPIM linear elastic static analysis of the four models and also benchmark the obtained results with the 3D study.



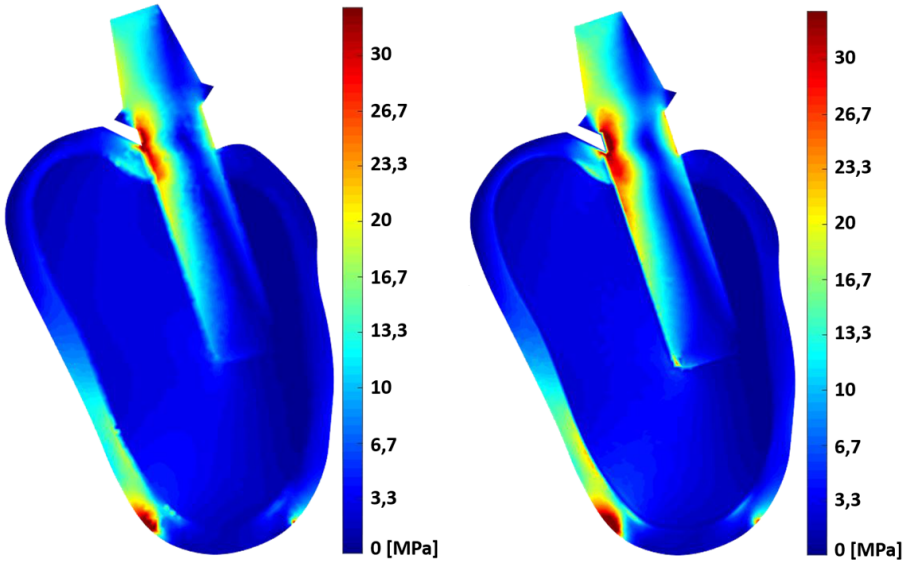
(a) FEM. (b) RPIM.

Figure 2.7: Results obtained with the FEM and RPIM for model 1.



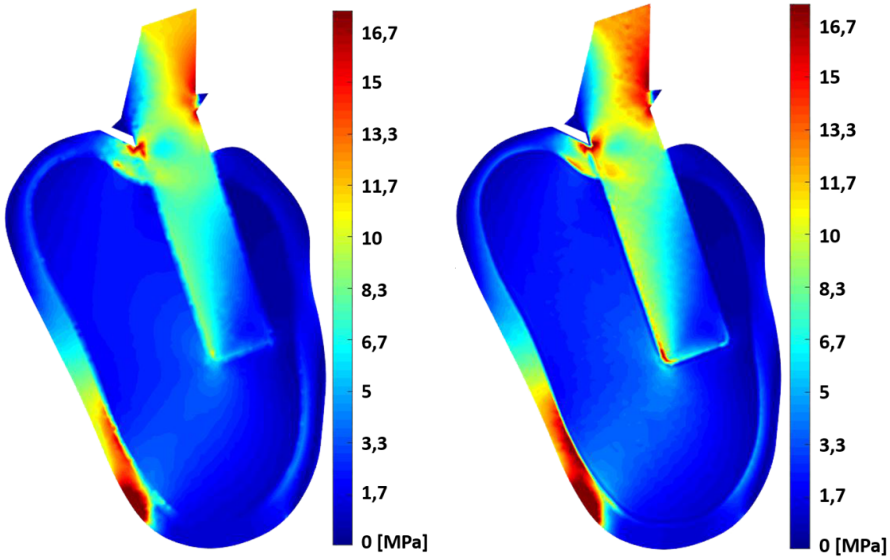
(a) FEM. (b) RPIM.

Figure 2.8: Results obtained with the FEM and RPIM for model 2.



(a) FEM. (b) RPIM.

Figure 2.9: Results obtained with the FEM and RPIM for model 3.



(a) FEM. (b) RPIM.

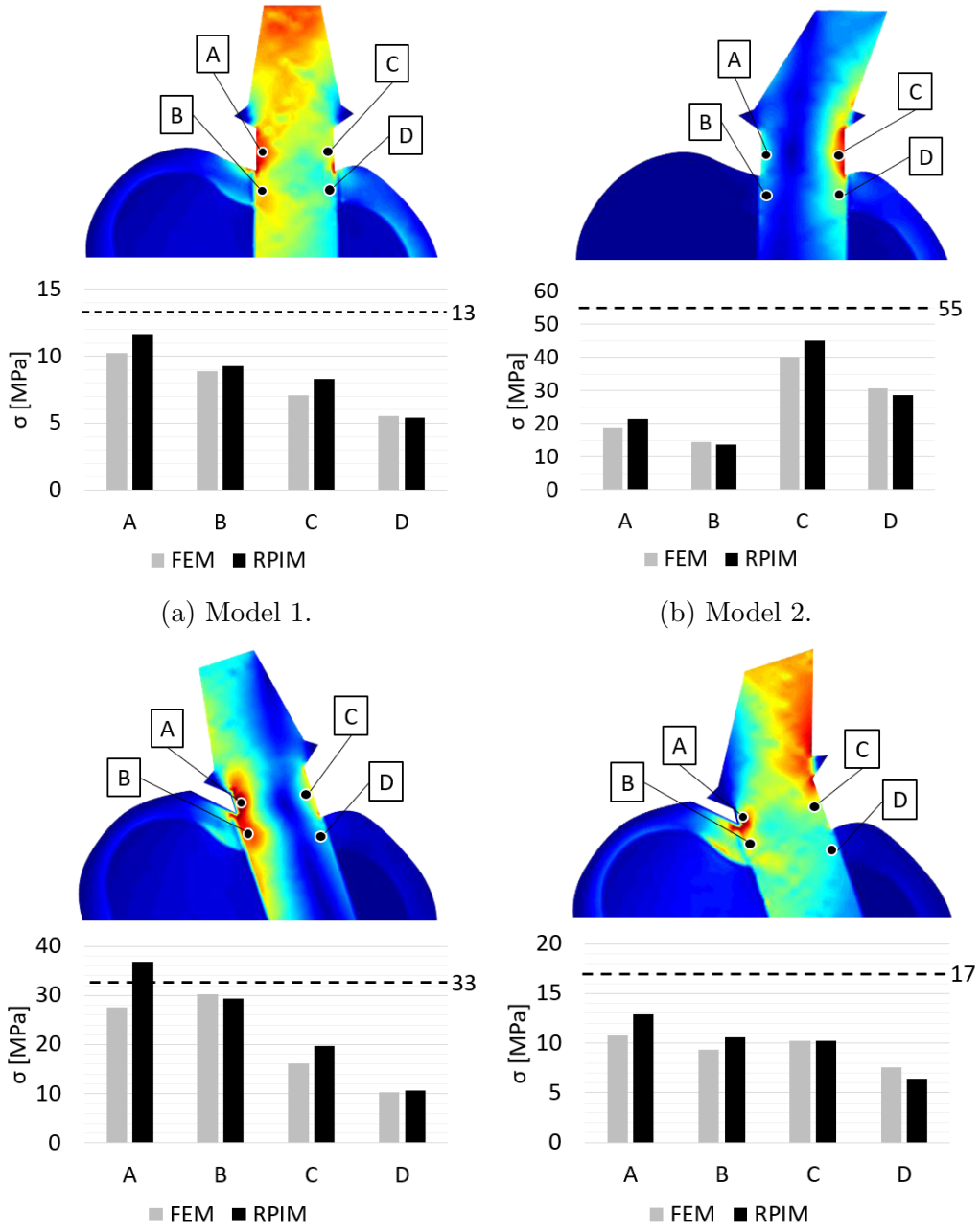
Figure 2.10: Results obtained with the FEM and RPIM for model 4.

For a better visual comparison the results have been limited to an upper limit, which corresponds to the maximum stress value obtained in the 3D study. This allows to visually compare the RPIM's results against the FEM's results.

At a first glance, it is possible to observe that RPIM's results possess a classic advantage commonly associated with the meshless methods over the FEM, the smoothness and resolution of the stress fields. For once, there are less visible fluctuations in the RPIM's color map, also, in the material boundaries it is possible to recognize in the RPIM a better transition.

Now, in order to compare the methods performances numerically four points (A, B, C and D) were picked in critical areas in the implants and the values of the von

Mises stress read from those points were plotted (Figures 2.11) for both the RPIM and the FEM, as well as the maximum value of the 3D study (dashed line in Figures 2.11).



(a) Model 1.

(b) Model 2.

(c) Model 3.

(d) Model 4.

Figure 2.11: Comparison of results between methods.

As it can be observed from the plots in Figures 2.11, the results from the RPIM and FEM are numerically comparable as they are very close for every point considered. Also, there appears to be a trend in which the RPIM seems to estimate a larger stress value than that of the FEM. All in all, RPIM produced results close to the 2D and 3D FEM analysis and this provides confidence in the methods ability.

This page has been intentionally left blank.

Chapter 3

Flow Formulation

As was mentioned the FDM additive manufacturing process relies on the extrusion of a polymer based material through a hot nozzle. Conceptually, this process can be closely compared to the more common and well studied forming process, extrusion. While the extrusion process is most used with metals (e.g. aluminium profiles) it is also widely used with polymers (e.g. PVC profiles).

For this reason, in this work the extrusion part of the FDM process will be modelled as a forming process using the basis described in literature for the extrusion of aluminium and polymers.

In this chapter, the formulation of the physical phenomenon is established and the RPIM equations are extended to the flow formulation in order to define the discrete system of equations.

3.1 Governing Equations

Forming processes, such as extrusion, involve large, permanent deformation. In such cases, it is an accepted conclusion that elastic effects are in general insignificant. Consequently, in the pioneer works in this subject, the initial assumption neglected the elastic deformations. This allows to treat the material as a non Newtonian viscoplastic fluid (commonly defined as a material unable of sustaining deviatoric stress while static), hence the term *flow formulation* [1, 20, 23, 4, 26].

Accepting these assumptions *a priori* then, it is possible to relate the Cauchy stress tensor, $\boldsymbol{\sigma}$, to the rate of deformation, strain rate $\dot{\boldsymbol{\varepsilon}}$, in the following manner,

$$\boldsymbol{\sigma} = \boldsymbol{D}(\dot{\boldsymbol{\varepsilon}}, T) \cdot \dot{\boldsymbol{\varepsilon}}, \tag{3.1}$$

where the matrix $\boldsymbol{D}$ may be dependent on the temperature and the strain rate itself, making this a non-linear problem. In the case of metals, such as aluminium, a strain hardening effect is also present and, so another dependence arises, this time to the strain invariants.

This kind of formulation is characterized by the fact that the velocities, $\boldsymbol{v}$, rather than displacements, $\boldsymbol{u}$, are of paramount importance and will require additional solution steps if a picture of the process through time is to be obtained. Such steps involve a time integration of velocity, knowing that,

$$\frac{\partial \boldsymbol{u}}{\partial t} = \boldsymbol{v}. \tag{3.2}$$

Replacing the displacements by the velocities, one can define the strain rate, $\dot{\boldsymbol{\varepsilon}}$, using the definition of strain,

$$\begin{aligned} \varepsilon_{ij} &= \frac{1}{2}\left(\frac{\partial u_i}{\partial x_j} + \frac{\partial u_j}{\partial x_i}\right), \\ \dot{\varepsilon}_{ij} &= \frac{1}{2}\left(\frac{\partial v_i}{\partial x_j} + \frac{\partial v_j}{\partial x_i}\right). \end{aligned} \tag{3.3}$$

Although a full displacement analysis is possible, i.e. one that incorporates both the rate and the elastic effects, it makes for a much more complex formulation and consequently a much more demanding numerical solution. Thus, in this work only the rate will be considered.

Some researchers assumed a steady state character for the extrusion process. This allows the use of a Eulerian type mesh - one that is fixed in space. Although an intermediate phase of the process exists, in which this assumption can be considered accurate (as a first approximation), generally it is not the case as the pressure of extrusion is often variable in time due to temperature changes and radial flows. Nevertheless, the Eulerian approach is valid to simulate non-stationary processes given that proper corrections are applied, often iteratively [2, 20, 21].

In contrast to the Eulerian approach, aiming to simulate the whole process, some non-stationary formulations arose in the form of Lagrangian models, in which the mesh is no longer fixed in space. This gained freedom requires a procedure to update the nodal coordinates in each iteration of the process. In spite of the clear advantage of this method, there is one major drawback that is related with the mesh deformation as the simulation goes on [2, 20, 21].

To reduce this problem another method was developed called Arbitrary Lagrangian Eulerian (ALE), in which the mesh is moved with a prescribed velocity independent of fluid motion. This prescribed velocity reduces mesh deformation. However it is a sensitive parameter that must be carefully chosen and can be difficult to determine [2, 20, 21].

In this work, a Lagrangian formulation will be used because of its accuracy in modelling a non-stationary process and because meshless methods do not show the same limitation of mesh deformation inherent to the FEM in the same situation.

In general, for polymer melts involved in extrusion processes the Reynolds number can be considered small, hence the flow is laminar and the effects of both the inertial and gravity forces can be neglected. Besides that, the assumption shall be made that the material has an isotropic and incompressible behaviour, which corresponds closely with the behaviour of most metals and polymers.

Considering these simplifications and hypothesis, the governing equations for the flow formulation of incompressible viscoplastic material takes the form,

$$\begin{aligned} \nabla \cdot \boldsymbol{\sigma} &= \boldsymbol{f} \quad in \quad \Omega, \\ \nabla \cdot \boldsymbol{v} &= 0 \quad in \quad \Omega. \end{aligned} \tag{3.4}$$

In matrix notation, the Cauchy stress tensor can be written as a sum of two contributions,

$$\boldsymbol{\sigma} = \boldsymbol{\sigma}_d + \boldsymbol{\sigma}_m, \tag{3.5}$$

where $\boldsymbol{\sigma}_d$ is de deviatoric stress tensor, $\boldsymbol{\sigma}_m$ is the average stress tensor characterized by a hydrostatic stress state,

$$\boldsymbol{\sigma}_m = -p\boldsymbol{I}, \tag{3.6}$$

where p is the pressure associated with that hydrostatic stress state, and is defined by,

$$p = -tr(\boldsymbol{\sigma})/3. \tag{3.7}$$

Following a similar procedure, this time for the strain rate tensor, it is obtained,

$$\dot{\boldsymbol{\varepsilon}} = \dot{\boldsymbol{\varepsilon}}_d + \dot{\boldsymbol{\varepsilon}}_m, \tag{3.8}$$

where $\dot{\boldsymbol{\varepsilon}}_d$ represents the deviatoric strain rates and $\dot{\boldsymbol{\varepsilon}}_m$ an isotropic strain rate state of magnitude $\dot{\varepsilon}_m$,

$$\dot{\boldsymbol{\varepsilon}}_m = \dot{\varepsilon}_m\boldsymbol{I}, \tag{3.9}$$

where $\dot{\varepsilon}_m$ is given by,

$$\dot{\varepsilon}_m = tr(\dot{\boldsymbol{\varepsilon}})/3. \tag{3.10}$$

If the stress and the strain rate are defined as vectors and not as tensors, using the *Voigt* notation in a two-dimensional space, the following is obtained,

$$\begin{aligned} \dot{\boldsymbol{\varepsilon}} &= \begin{bmatrix} \dot{\varepsilon}_x & \dot{\varepsilon}_y & \dot{\gamma}_{xy} \end{bmatrix}^{\mathrm{T}}, \\ \boldsymbol{\sigma} &= \begin{bmatrix} \sigma_x & \sigma_y & \tau_{xy} \end{bmatrix}^{\mathrm{T}}. \end{aligned} \tag{3.11}$$

Defining a matrix $\boldsymbol{m}$ in the following manner,

$$\boldsymbol{m} = \begin{bmatrix} 1 & 1 & 0 \end{bmatrix}^{\mathrm{T}}. \tag{3.12}$$

Using this notation, is is possible to write,

$$\begin{aligned} p &= -\frac{1}{3}\boldsymbol{m}^{\mathrm{T}}\boldsymbol{\sigma}, \\ \dot{\varepsilon}_m &= \frac{1}{3}\boldsymbol{m}^{\mathrm{T}}\dot{\boldsymbol{\varepsilon}}, \end{aligned} \tag{3.13}$$

and also write the following,

$$\begin{aligned} \boldsymbol{\sigma}_d &= \boldsymbol{\sigma} + \boldsymbol{m}p, \\ \dot{\boldsymbol{\varepsilon}}_d &= \dot{\boldsymbol{\varepsilon}} - \boldsymbol{m}\dot{\varepsilon}_m. \end{aligned} \tag{3.14}$$

Inserting (3.13) in (3.14), it yields,

$$\begin{aligned} \boldsymbol{\sigma}_d &= \left(\boldsymbol{I} - \frac{1}{3}\boldsymbol{m}\boldsymbol{m}^{\mathrm{T}}\right)\boldsymbol{\sigma}, \\ \dot{\boldsymbol{\varepsilon}}_d &= \left(\boldsymbol{I} - \frac{1}{3}\boldsymbol{m}\boldsymbol{m}^{\mathrm{T}}\right)\dot{\boldsymbol{\varepsilon}}, \end{aligned} \tag{3.15}$$

where,

$$\boldsymbol{I}_d = \left(\boldsymbol{I} - \frac{1}{3}\boldsymbol{m}\boldsymbol{m}^{\mathrm{T}} \right), \tag{3.16}$$

and thus,

$$\boldsymbol{I}_d = \frac{1}{3}\begin{bmatrix} 2 & -1 & 0 \\ -1 & 2 & 0 \\ 0 & 0 & 3 \end{bmatrix}. \tag{3.17}$$

The deviatoric stresses, $\boldsymbol{\sigma}_d$, under the assumptions described above is considered proportional to the deviatoric strain rates, [1, 2, 20, 21, 23, 4, 26]

$$\boldsymbol{\sigma}_d = \mu \boldsymbol{I}_0 \dot{\boldsymbol{\varepsilon}}_d, \tag{3.18}$$

where μ is the material viscosity and the matrix $\boldsymbol{I}_0$ is,

$$\boldsymbol{I}_0 = \begin{bmatrix} 2 & 0 & 0 \\ 0 & 2 & 0 \\ 0 & 0 & 1 \end{bmatrix}. \tag{3.19}$$

The expression (3.18) can be further developed by inserting the relation of deviatoric strain rates defined in equation (3.15),

$$\boldsymbol{\sigma}_d = \mu \boldsymbol{I}_0 \boldsymbol{I}_d \dot{\boldsymbol{\varepsilon}} = \mu \boldsymbol{I}_1 \dot{\boldsymbol{\varepsilon}}, \tag{3.20}$$

where $\boldsymbol{I}_1$ is,

$$\boldsymbol{I}_1 = \frac{1}{3}\begin{bmatrix} 4 & -2 & 0 \\ -2 & 4 & 0 \\ 0 & 0 & 3 \end{bmatrix}. \tag{3.21}$$

These stress-strain rate matrix relations, $\boldsymbol{I}_0$ and $\boldsymbol{I}_1$, are both valid in this specific problem but both have some considerations associated with its application. Considering the incompressibility assumption for the 2D problem, it is possible to define,

$$tr(\dot{\boldsymbol{\varepsilon}}) = \dot{\varepsilon}_x + \dot{\varepsilon}_y = 0, \tag{3.22}$$

because there is no volume change and the first strain invariant is associated with volume changes. Looking at (3.22) and (3.10) it is possible to conclude that in the case of incompressibility,

$$\dot{\varepsilon}_m = 0. \tag{3.23}$$

If this is the case, only the deviatoric component exists for the strain rates, $\dot{\boldsymbol{\varepsilon}} = \dot{\boldsymbol{\varepsilon}}_d$, and therefore matrix $\boldsymbol{I}_0$ should be used to relate stress and strain rates. If incompressibility is not a constraint and the first strain invariant is not null, then matrix $\boldsymbol{I}_1$ should be used instead.

In this work, since incompressibility is assumed *a priori*, the relation established in (3.18) will be considered. To introduce the incompressibility in the numerical

formulation, a penalty method will be used. One can write the penalized form of the constraint established in (3.4) as,

$$\nabla \cdot \boldsymbol{v} = p/\alpha, \tag{3.24}$$

where $\alpha \to \infty$. In the limit, the exact constraint is obtained and that can be approximated as close as necessary by using a large enough α. Although, most authors recommend the use of α as a function of the material viscosity, [1, 20, 23, 4, 26]

$$\alpha = 10^{7-8}\mu. \tag{3.25}$$

3.1.1 Material Laws

For a Newtonian fluid, the viscosity is constant. However, in this general case the viscosity may be dependent on the strain rate itself, the accumulated strain and the temperature. Besides, introducing non linearity in the problem also makes the material properties dependent on the heat transfer that is occuring in the domain. The fluid is then considered non Newtonian.

Perzyna's Viscoplasticity Model

For a von Mises type of viscoplastic material, i.e., one in which the yield is governed by a critical value in the second deviatoric stress invariant, J_2, valid in the analysis of ductile materials, the relationship between the strain rate and the stress field of the material can be obtained using the Perzyna model [21], which states,

$$\dot{\boldsymbol{\varepsilon}}^{\boldsymbol{vp}} = \dot{\gamma}\frac{\partial Y(\boldsymbol{\sigma}, \boldsymbol{q})}{\partial \boldsymbol{\sigma}}, \tag{3.26}$$

where Y is the viscoplastic potential, that is usually the same as the plastic criterion, and $\boldsymbol{q}$ represents hardening parameters common in metals. Note that the vp superscript denotes the viscoplastic component of the strain, which is the only one that exists when the elastic part is neglected. Thus, the superscript will be avoided from now on. Also, $\dot{\gamma}$ is a scalar defined as the following function,

$$\dot{\gamma} = \frac{\langle g(Y(\boldsymbol{\sigma}, \boldsymbol{q}))\rangle}{\gamma}, \text{ with } \langle x\rangle = \frac{x + |x|}{2}, \tag{3.27}$$

where $\langle g\rangle$ is a monotonic function which takes zero value if the viscoplastic potential is negative or null, and γ is a physical constant often called fluidity parameter.

Considering a von Mises yield criterion,

$$Y(\boldsymbol{\sigma}, \boldsymbol{q}) = \bar{\sigma}(\boldsymbol{\sigma}_d) - \sigma_y(\dot{\bar{\boldsymbol{\varepsilon}}}, T), \tag{3.28}$$

where σ_y is the uniaxial yield stress of the material. This material property is often a function of temperature and the effective strain rate, and can follow laws like the Sellars-Tegart law commonly used for aluminium. For the sake of simplicity, and since the prime goal of of this work is the polymer application, a constant σ_y will

be considered. Also, $\bar{\sigma}$ is the effective stress and $\dot{\bar{\varepsilon}}$ the effective strain rate, and they are defined as,

$$\begin{aligned} \bar{\sigma} &= \sqrt{\frac{3}{2}\boldsymbol{\sigma}_d : \boldsymbol{\sigma}_d} = \sqrt{3J_2}, \\ \dot{\bar{\varepsilon}} &= \sqrt{\frac{2}{3}\dot{\boldsymbol{\varepsilon}} : \dot{\boldsymbol{\varepsilon}}}. \end{aligned} \tag{3.29}$$

Combining equations (3.26) and (3.28),

$$\dot{\boldsymbol{\varepsilon}} = \dot{\gamma}\frac{3\boldsymbol{\sigma}_d}{2\bar{\sigma}}. \tag{3.30}$$

Now, introducing the definition of effective strain rate defined in equation (3.29),

$$\dot{\bar{\varepsilon}} = \frac{\dot{\gamma}}{\bar{\sigma}}\sqrt{\frac{3}{2}\boldsymbol{\sigma}_d : \boldsymbol{\sigma}_d} = \dot{\gamma}, \tag{3.31}$$

proving that $\dot{\gamma}$ is the same as the effective strain rate. Following this conclusion, and considering only cases where Y is positive, i.e., $\bar{\sigma}$ is greater or equal than σ_y, it can be assumed that $g(f) = f$ and follow equation (3.27) with,

$$\dot{\bar{\varepsilon}} = \dot{\gamma} = \frac{\langle \bar{\sigma} - \sigma_y \rangle}{\gamma} \rightarrow \bar{\sigma} = \gamma\dot{\bar{\varepsilon}} + \sigma_y \ , \ \bar{\sigma} \geq \sigma_y. \tag{3.32}$$

This relationship, when introduced in equation (3.30), yields the following viscoplastic constitutive equation,

$$\boldsymbol{\sigma}_d = 2\frac{\gamma\dot{\bar{\varepsilon}} + \sigma_y}{3\dot{\bar{\varepsilon}}}\dot{\boldsymbol{\varepsilon}}. \tag{3.33}$$

Notice that after analysing equation (3.18) becomes apparent that, [21]

$$\mu = \frac{\sigma_y + \gamma\dot{\bar{\varepsilon}}}{3\dot{\bar{\varepsilon}}}. \tag{3.34}$$

Some authors rewrite the same relation with an exponential coefficient, which represents a different solution of the same Perzyna-like model, [20]

$$\mu = \frac{\sigma_y + \gamma\dot{\bar{\varepsilon}}^n}{3\dot{\bar{\varepsilon}}}. \tag{3.35}$$

In the special cases of plasticity or materials where a rigid-plastic behaviour is applicable, it follows that $Y = \bar{\sigma} - \sigma_y = 0$ and, therefore,

$$\mu = \frac{\sigma_y}{3\dot{\bar{\varepsilon}}}. \tag{3.36}$$

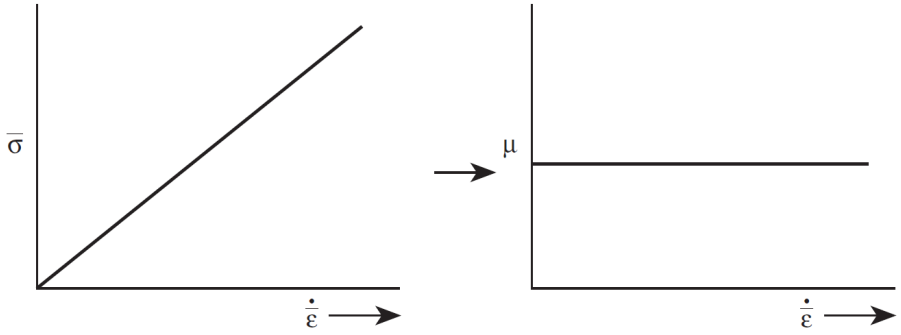
Norton-Hoff Model

For non Newtonian fluids, such as polymers and hot metals, most authors recommend the use of a power law that in general holds appropriate. This law (called Ostwald de Waele law in [20] and Norton-Hoff model in [21, 27]) states the following,

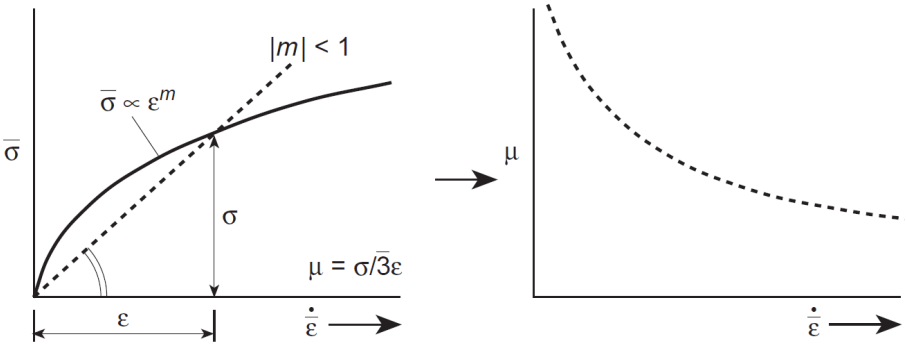
$$\mu = \mu_0\dot{\bar{\boldsymbol{\varepsilon}}}^{n-1}, \tag{3.37}$$

where n is smaller than unity and is called the sensitivity index, $\mu_0 = \mu_0(T)$ is the initial viscosity and $\dot{\bar{\varepsilon}}$ is the effective strain rate already defined in equation (3.29).

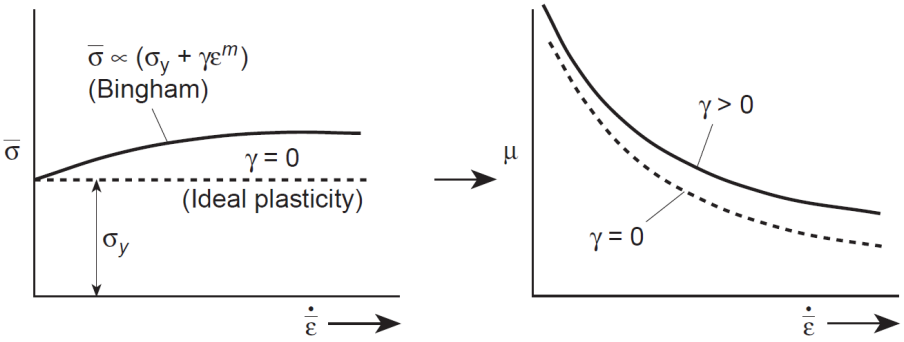
In Figure 3.1 the relationship between the material's viscosity, μ, effective strain rate, $\dot{\bar{\varepsilon}}$, and effective stress, $\bar{\sigma}$, is represented for different types of materials.



(a) Linear, Newtonian fluid.



(b) Non Newtonian polymers.



(c) Viscoplastic materials.

Figure 3.1: Relationship between properties for various materials [1].

3.2 Discrete Equations

The flow formulation allows the analysis of the material flow using the regular displacement-based methodology. This means that while in regular 2D linear elastic equations one refers to nodal displacements, in this method, the displacements will represent velocities. Thus, the vector of nodal velocities can be written as,

$$\tilde{\boldsymbol{v}} = \begin{bmatrix} \tilde{v}_{x1} & \tilde{v}_{y1} & \tilde{v}_{x2} & \tilde{v}_{y2} & \cdots & \tilde{v}_{xn} & \tilde{v}_{yn} \end{bmatrix}^{\mathrm{T}}. \tag{3.38}$$

Notice the tilde above the v which represents nodal values. The velocity in an interest point can, therefore, be given by,

$$\boldsymbol{v} = \begin{bmatrix} v_x \\ v_y \end{bmatrix} = \boldsymbol{N}_v \tilde{\boldsymbol{v}}, \tag{3.39}$$

where the matrix of velocity shape functions, $\boldsymbol{N}_v$, is given by,

$$\boldsymbol{N}_v = \begin{bmatrix} N_{v1} & 0 & N_{v2} & 0 & \cdots & N_{vn} & 0 \\ 0 & N_{v1} & 0 & N_{v2} & \cdots & 0 & N_{vn} \end{bmatrix}. \tag{3.40}$$

Similarly, the vector of nodal pressures is,

$$\tilde{\boldsymbol{p}} = \begin{bmatrix} \tilde{p}_1 & \tilde{p}_2 & \cdots & \tilde{p}_n \end{bmatrix}^{\mathrm{T}}, \tag{3.41}$$

which can be used to obtain the pressure at any interest point with the following expression,

$$p = \boldsymbol{N}_p \tilde{\boldsymbol{p}}, \tag{3.42}$$

where the matrix of pressure shape functions, $\boldsymbol{N}_p$, is defined as,

$$\boldsymbol{N}_p = \begin{bmatrix} N_{p1} & N_{p2} & \cdots & N_{pn} \end{bmatrix}. \tag{3.43}$$

Defining the strain operator matrix as,

$$\boldsymbol{\mathcal{L}} = \begin{bmatrix} \frac{\partial}{\partial x} & 0 \\ 0 & \frac{\partial}{\partial y} \\ \frac{\partial}{\partial y} & \frac{\partial}{\partial x} \end{bmatrix}. \tag{3.44}$$

This, with equation (3.3) in mind, allows to write the following about the strain rate vector,

$$\dot{\boldsymbol{\varepsilon}} = \boldsymbol{\mathcal{L}} \boldsymbol{v} = \boldsymbol{\mathcal{L}} \boldsymbol{N}_v \tilde{\boldsymbol{v}} = \boldsymbol{B} \tilde{\boldsymbol{v}}, \tag{3.45}$$

with $\boldsymbol{B}$ being,

$$\boldsymbol{B} = \begin{bmatrix} \boldsymbol{B}_1 & \boldsymbol{B}_2 & \cdots & \boldsymbol{B}_n \end{bmatrix}, \ \boldsymbol{B}_i = \begin{bmatrix} \frac{\partial N_{vi}}{\partial x} & 0 \\ 0 & \frac{\partial N_{vi}}{\partial y} \\ \frac{\partial N_{vi}}{\partial y} & \frac{\partial N_{vi}}{\partial x} \end{bmatrix}. \tag{3.46}$$

Recalling equations (3.14) and (3.18), it is possible write,

$$\boldsymbol{\sigma} = \mu \boldsymbol{I}_0 \dot{\boldsymbol{\varepsilon}} - \boldsymbol{m} p = \mu \boldsymbol{I}_0 \boldsymbol{B} \tilde{\boldsymbol{v}} - \boldsymbol{m} p, \tag{3.47}$$

allowing to rewrite the weak form of the problem using the Galerkin variational principle, defined in equation (2.38). Since, the displacement vector in this formulation is actually comprised of velocities, its first derivatives are accelerations. In this work, the dynamic effects are neglected, and so, the Lagrangian functional can be written as,

$$L = -\frac{1}{2} \int_{\Omega} \dot{\boldsymbol{\varepsilon}}^{\mathrm{T}} \boldsymbol{\sigma} \, \mathrm{d}\Omega + \int_{\Omega} \boldsymbol{v}^{\mathrm{T}} \boldsymbol{b} \, \mathrm{d}\Omega + \int_{\Gamma} \boldsymbol{v}^{\mathrm{T}} \boldsymbol{t} \, \mathrm{d}\Gamma. \tag{3.48}$$

Minimizing it,

$$\begin{aligned}\delta\int_{t_1}^{t_2}\left[-\frac{1}{2}\int_\Omega \dot{\boldsymbol{\varepsilon}}^{\mathrm{T}}\boldsymbol{\sigma}\,\mathrm{d}\Omega+\int_\Omega \boldsymbol{v}^{\mathrm{T}}\boldsymbol{b}\,\mathrm{d}\Omega+\int_\Gamma \boldsymbol{v}^{\mathrm{T}}\boldsymbol{t}\,\mathrm{d}\Gamma\right]\mathrm{d}t=0,\\ \int_{t_1}^{t_2}\left[-\frac{1}{2}\int_\Omega \delta\left(\dot{\boldsymbol{\varepsilon}}^{\mathrm{T}}\boldsymbol{\sigma}\right)\,\mathrm{d}\Omega+\int_\Omega \delta\boldsymbol{v}^{\mathrm{T}}\boldsymbol{b}\,\mathrm{d}\Omega+\int_\Gamma \delta\boldsymbol{v}^{\mathrm{T}}\boldsymbol{t}\,\mathrm{d}\Gamma\right]\mathrm{d}t=0.\end{aligned} \tag{3.49}$$

For an integral to be zero, its integrand must also be null, which allows to write the following,

$$-\frac{1}{2}\int_\Omega \delta\left(\dot{\boldsymbol{\varepsilon}}^{\mathrm{T}}\boldsymbol{\sigma}\right)\,\mathrm{d}\Omega+\int_\Omega \delta\boldsymbol{v}^{\mathrm{T}}\boldsymbol{b}\,\mathrm{d}\Omega+\int_\Gamma \delta\boldsymbol{v}^{\mathrm{T}}\boldsymbol{t}\,\mathrm{d}\Gamma=0. \tag{3.50}$$

From the procedure described before leading to equation (2.49), it is known that,

$$\delta\left(\dot{\boldsymbol{\varepsilon}}^{\mathrm{T}}\boldsymbol{\sigma}\right)=2\delta\dot{\boldsymbol{\varepsilon}}^{\mathrm{T}}\boldsymbol{\sigma}, \tag{3.51}$$

which ultimately, having equation (3.50) in mind, leads to the following expression,

$$\int_\Omega \delta\dot{\boldsymbol{\varepsilon}}^{\mathrm{T}}\boldsymbol{\sigma}\,\mathrm{d}\Omega-\int_\Omega \delta\boldsymbol{v}^{\mathrm{T}}\boldsymbol{b}\,\mathrm{d}\Omega-\int_\Gamma \delta\boldsymbol{v}^{\mathrm{T}}\boldsymbol{t}\,\mathrm{d}\Gamma=0. \tag{3.52}$$

Introducing equations (3.39), (3.45) and (3.47) into (3.52) yields the following,

$$\int_\Omega \delta\tilde{\boldsymbol{v}}^{\mathrm{T}}\boldsymbol{B}^{\mathrm{T}}\mu\boldsymbol{I}_0\boldsymbol{B}\tilde{\boldsymbol{v}}\,\mathrm{d}\Omega-\int_\Omega \delta\tilde{\boldsymbol{v}}^{\mathrm{T}}\boldsymbol{B}^{\mathrm{T}}\boldsymbol{m}p\,\mathrm{d}\Omega+\int_\Omega \delta\tilde{\boldsymbol{v}}^{\mathrm{T}}\boldsymbol{N}_v^{\mathrm{T}}\boldsymbol{b}\,\mathrm{d}\Omega+\int_\Gamma \delta\tilde{\boldsymbol{v}}^{\mathrm{T}}\boldsymbol{N}_v^{\mathrm{T}}\boldsymbol{t}\,\mathrm{d}\Gamma=0. \tag{3.53}$$

The $\delta\tilde{\boldsymbol{v}}^{\mathrm{T}}$ and $\tilde{\boldsymbol{v}}$ terms are independent of the integrals so they can be brought outside, yielding,

$$\delta\tilde{\boldsymbol{v}}^{\mathrm{T}}\left(\int_\Omega \boldsymbol{B}^{\mathrm{T}}\mu\boldsymbol{I}_0\boldsymbol{B}\,\mathrm{d}\Omega\,\tilde{\boldsymbol{v}}-\int_\Omega \boldsymbol{B}^{\mathrm{T}}\boldsymbol{m}p\,\mathrm{d}\Omega+\int_\Omega \boldsymbol{N}_v^{\mathrm{T}}\boldsymbol{b}\,\mathrm{d}\Omega+\int_\Gamma \boldsymbol{N}_v^{\mathrm{T}}\boldsymbol{t}\,\mathrm{d}\Gamma\right)=0, \tag{3.54}$$

which ultimately, leads to,

$$\int_\Omega \boldsymbol{B}^{\mathrm{T}}\mu\boldsymbol{I}_0\boldsymbol{B}\,\mathrm{d}\Omega\,\tilde{\boldsymbol{v}}-\int_\Omega \boldsymbol{B}^{\mathrm{T}}\boldsymbol{m}p\,\mathrm{d}\Omega+\int_\Omega \boldsymbol{N}_v^{\mathrm{T}}\boldsymbol{b}\,\mathrm{d}\Omega+\int_\Gamma \boldsymbol{N}_v^{\mathrm{T}}\boldsymbol{t}\,\mathrm{d}\Gamma=0. \tag{3.55}$$

3.2.1 Direct Method

In the direct method, the only degree of freedom that will be considered is the velocity in the nodes. This means that the pressure has to be eliminated. For this, a penalty method is used in the incompressibility constraint. From equations (3.4), (3.13), (3.23) and (3.24),

$$\dot{\varepsilon}_m=0\;\rightarrow\;\boldsymbol{m}^{\mathrm{T}}\dot{\boldsymbol{\varepsilon}}=0, \tag{3.56}$$

which, in penalty form can be numerically represented as,

$$\boldsymbol{m}^{\mathrm{T}}\dot{\boldsymbol{\varepsilon}}=\boldsymbol{m}^{\mathrm{T}}\boldsymbol{B}\tilde{\boldsymbol{v}}=p/\alpha, \tag{3.57}$$

where α, a big number, was chosen to be $\alpha = 10^7\mu$, according to (3.25). From this, it follows,

$$p = \alpha \boldsymbol{m}^{\mathrm{T}} \boldsymbol{B} \tilde{\boldsymbol{v}}. \tag{3.58}$$

Introducing equation (3.58) in equation (3.55), it is obtained,

$$\int_{\Omega} \boldsymbol{B}^{\mathrm{T}} \mu \boldsymbol{I}_0 \boldsymbol{B} \, \mathrm{d}\Omega \, \tilde{\boldsymbol{v}} - \alpha \int_{\Omega} \boldsymbol{B}^{\mathrm{T}} \boldsymbol{m} \boldsymbol{m}^{\mathrm{T}} \boldsymbol{B} \, \mathrm{d}\Omega \, \tilde{\boldsymbol{v}} + \int_{\Omega} \boldsymbol{N}_v^{\mathrm{T}} \boldsymbol{b} \, \mathrm{d}\Omega + \int_{\Gamma} \boldsymbol{N}_v^{\mathrm{T}} \boldsymbol{t} \, \mathrm{d}\Gamma = 0. \tag{3.59}$$

Assuming,

$$\begin{aligned} \boldsymbol{K}_v &= \int_{\Omega} \boldsymbol{B}^{\mathrm{T}} \mu \boldsymbol{I}_0 \boldsymbol{B} \, \mathrm{d}\Omega, \\ \boldsymbol{K}_p &= -\alpha \int_{\Omega} \boldsymbol{B}^{\mathrm{T}} \boldsymbol{m} \boldsymbol{m}^{\mathrm{T}} \boldsymbol{B} \, \mathrm{d}\Omega, \\ \boldsymbol{f}_b &= \int_{\Omega} \boldsymbol{N}_v^{\mathrm{T}} \boldsymbol{b} \, \mathrm{d}\Omega, \\ \boldsymbol{f}_t &= \int_{\Gamma} \boldsymbol{N}_v^{\mathrm{T}} \boldsymbol{t} \, \mathrm{d}\Gamma, \\ \boldsymbol{f} &= \boldsymbol{f}_b + \boldsymbol{f}_t, \end{aligned} \tag{3.60}$$

where $\boldsymbol{K}_v$, $\boldsymbol{K}_p$, $\boldsymbol{f}_b$, $\boldsymbol{f}_t$ and $\boldsymbol{f}$ are the stiffness matrix associated with velocity, stiffness matrix associated with pressure, the vector of body forces, the vector of boundary forces and the vector of external forces, respectively. This way, it is possible to write the weak form equations in a more compact manner,

$$(\boldsymbol{K}_v + \boldsymbol{K}_p) \, \tilde{\boldsymbol{v}} = \boldsymbol{f}. \tag{3.61}$$

The velocity field can be obtained inverting the stiffness matrix,

$$\tilde{\boldsymbol{v}} = (\boldsymbol{K}_v + \boldsymbol{K}_p)^{-1} \, \boldsymbol{f}. \tag{3.62}$$

Also, the pressure field can be obtained using equation (3.58). Some authors recommend that every pressure related term is integrated using reduced integration to avoid locking issues [20].

3.2.2 Mixed Method

In the mixed formulation, pressure becomes a part of the system of equations. So now, instead of just the velocities, the formulation has velocities and pressure as the degrees of freedom associated with each node. Thus, introducing equation (3.42) into (3.55) results in,

$$\int_{\Omega} \boldsymbol{B}^{\mathrm{T}} \mu \boldsymbol{I}_0 \boldsymbol{B} \, \mathrm{d}\Omega \, \tilde{\boldsymbol{v}} - \int_{\Omega} \boldsymbol{B}^{\mathrm{T}} \boldsymbol{m} \boldsymbol{N}_p \tilde{\boldsymbol{p}} \, \mathrm{d}\Omega + \int_{\Omega} \boldsymbol{N}_v^{\mathrm{T}} \boldsymbol{b} \, \mathrm{d}\Omega + \int_{\Gamma} \boldsymbol{N}_v^{\mathrm{T}} \boldsymbol{t} \, \mathrm{d}\Gamma = 0. \tag{3.63}$$

Similar to $\tilde{\boldsymbol{v}}$, $\tilde{\boldsymbol{p}}$ is not of function of the volume of the domain and so it can be taken outside the integral,

$$\int_{\Omega} \boldsymbol{B}^{\mathrm{T}} \mu \boldsymbol{I}_0 \boldsymbol{B} \, \mathrm{d}\Omega \, \tilde{\boldsymbol{v}} - \int_{\Omega} \boldsymbol{B}^{\mathrm{T}} \boldsymbol{m} \boldsymbol{N}_p \, \mathrm{d}\Omega \, \tilde{\boldsymbol{p}} + \int_{\Omega} \boldsymbol{N}_v^{\mathrm{T}} \boldsymbol{b} \, \mathrm{d}\Omega + \int_{\Gamma} \boldsymbol{N}_v^{\mathrm{T}} \boldsymbol{t} \, \mathrm{d}\Gamma = 0, \tag{3.64}$$

where,

$$\boldsymbol{Q} = -\int_{\Omega} \boldsymbol{B}^{\mathrm{T}} \boldsymbol{m} \boldsymbol{N}_p \, \mathrm{d}\Omega. \tag{3.65}$$

So, this allows to write,

$$\boldsymbol{K}_v \tilde{\boldsymbol{v}} + \boldsymbol{Q} \tilde{\boldsymbol{p}} = \boldsymbol{f}. \tag{3.66}$$

This system requires an additional equation for $\tilde{\boldsymbol{p}}$, which can be obtained by a week form of equation (3.57),

$$\boldsymbol{Q}^{\mathrm{T}} \tilde{\boldsymbol{v}} - \frac{h^2}{\alpha} \boldsymbol{I} \tilde{\boldsymbol{p}} = \boldsymbol{0}, \tag{3.67}$$

where h is a parameter regarding the average minimum nodal spacing. In matrix form comes that,

$$\begin{bmatrix} \boldsymbol{K}_v & \boldsymbol{Q}^{\mathrm{T}} \\ \boldsymbol{Q}^{\mathrm{T}} & -\frac{h^2}{\alpha} \boldsymbol{I} \end{bmatrix} \begin{bmatrix} \tilde{\boldsymbol{v}} \\ \tilde{\boldsymbol{p}} \end{bmatrix} = \begin{bmatrix} \boldsymbol{f} \\ \boldsymbol{0} \end{bmatrix}. \tag{3.68}$$

Thus, the nodal solution can be obtained with,

$$\begin{bmatrix} \tilde{\boldsymbol{v}} \\ \tilde{\boldsymbol{p}} \end{bmatrix} = \begin{bmatrix} \boldsymbol{K}_v & \boldsymbol{Q}^{\mathrm{T}} \\ \boldsymbol{Q}^{\mathrm{T}} & -\frac{h^2}{\alpha} \boldsymbol{I} \end{bmatrix}^{-1} \begin{bmatrix} \boldsymbol{f} \\ \boldsymbol{0} \end{bmatrix}. \tag{3.69}$$

3.2.3 Mixed Dual Method

Mathematically, the mixed dual method shares the formulation with the mixed method. Thus, the weak form governing equation for this method is equation (3.68). Despite this, the difference between the two lies in the nodal discretization utilized.

The direct penalty method uses only one nodal discretization, in which, each node has two velocity degrees of freedom for both in-plane directions. In this method, the pressure is calculated in the integration points and not as a nodal field variable. Similarly, the mixed method also has only one nodal discretization. Although, the mixed method's nodes possess two velocity degrees of freedom and one pressure degree of freedom. For every node, and in each iteration of the program, the complete velocity and pressure information is an output of the governing system of equations. In both these methods there is the possibility to independently calculate shape functions for the velocity and pressure terms. This allows for more versatility in the choice of integration scheme, as reduced and hybrid schemes become a possibility.

In the case of the mixed dual method there are two nodal discretizations independent from one another. One is for velocity related terms, and the other for pressure related terms. This is an attempt to mimic a common FEM methodology utilized in mixed *u-p* type formulations, in which, a distinct type of elements is used. These element's nodes are specifically associated with one field variable. An element of this

kind would be the regular 3-noded triangular element with an additional 4^{th} node in the center, the nodes in the contour could be linked with velocity calculations and the central node associated with pressure calculations.

It is common for the pressure nodes to be less in number as compared to the the velocity ones, and so the same trend was implemented in this work, since the velocity mesh is denser than the pressure mesh. And, although there are two independent nodal discretizations, there is just one background integration mesh shared by the two. In this method, there is no use in implementing hybrid integration schemes as this is a default because of the difference in the nodal density for velocity and pressure terms. Looking from the perspective of one integration point, for the same area it sees much more velocity nodes than pressure nodes and the inherent integration scheme will be weighted by the number of nodes it sees in its influence domain. And to better mimic the FEM's mixed formulation elements, the pressure influence domains were built by removing nodes from the velocity influence domains. This way, it was assured that every pressure node inside the influence domain of a certain integration point corresponds with a node of the velocity mesh that is also inside the same influence domain.

3.3 Code Considerations

Having described the main mathematical foundation of the methods implemented in this work, it is important to discuss and present some key aspects of the code that served to implement them. Those key aspects include its structure, key variables, and overall general procedure.

As it was stated previously, due to the nature of the physical phenomenon in study this work is highly non-linear and therefore its analysis will be iterative. This means that since the solution depends on itself, the converged final value will be the result of several runs of the program. That will be outlined in more detail in the algorithm descriptions. In the meantime, it is important to define some variables used in the program that will be useful in the following discussion of results. In no particular order:

$\boldsymbol{x}$ Vector of spatial coordinates for velocity and pressure nodes (direct penalty and mixed methods) or just velocity nodes (mixed dual method).

$\boldsymbol{x_p}$ Vector of nodal coordinates for the pressure discretization (mixed dual method).

α Penalty parameter used to enforce the incompressibility constraint. Its value is taken, per recommendation of the literature, as,

$$\alpha = 10^7 \mu. \tag{3.70}$$

L Total length of the model in the x direction.

D Total length of the model in the y direction.

$divL$ Number of mesh divisions created along the L dimension, i.e., along the x direction. This refers to densest mesh of all methods, in this case, the velocity discretization.

$divD$ Number of mesh divisions created along the D dimension, i.e., along the y direction. This refers to densest mesh of all methods, in this case, the velocity discretization.

n_{node} Number of velocity nodes in a particular mesh. This number can be, easily, calculated for a rectangular mesh as follows,

$$n_{node} = (divL + 1) \cdot (divD + 1). \tag{3.71}$$

n_{dom} Number of nodes inside a particular influence domain.

λ Parameter used to create irregular meshes. This parameter acts in the nodal coordinates and is inversely proportional to the degree of irregularity. The greater the value of the parameter, the more regular the mesh is. λ is defined as,

$$\begin{aligned} x_{irreg} &= x_{reg} + \frac{rand - 0,5}{0,5} \frac{L}{\lambda \cdot divL} \text{ with } 0 \leq rand \leq 1, \\ y_{irreg} &= y_{reg} + \frac{rand - 0,5}{0,5} \frac{D}{\lambda \cdot divD} \text{ with } 0 \leq rand \leq 1. \end{aligned} \tag{3.72}$$

Also, notice that $rand$ is a random scalar between 0 and 1 that follows a Gaussian distribution.

$quado$ Number of integration points considered in both directions for the particular integration scheme. A grid of $n_{quado} \cdot n_{quado}$ integration points is created.

$quado_{red}$ Number of integration points considered in both directions if a reduced integration scheme is required. A grid of $n_{quadored} \cdot n_{quadored}$ integration points is created.

3.3.1 General Static Procedure

In this section, the general procedure of the program will be outlined step by step. Most specifically, the program in its static form, with no mesh updating and no time steps.

Direct Method

1. Read problem data, input variables and material properties;
2. Construct the nodal discretization:
   (a) Based on the input data construct a regular rectangular mesh;
   (b) If necessary apply a randomization procedure - equation (3.72) - on the existing discretization to construct an irregular mesh;
   (c) Based on the geometrical definition remove specific nodes from the existing discretization to create voids or other geometrical details in the mesh.
3. Construct the integration mesh:

(a) Create the integration mesh following the isoparametric formulation and the Gaussian quadrature scheme for a $L \times D$ rectangular domain;

(b) Remove integration points outside the domain (if there exists voids).

4. Construct the reduced integration mesh with a similar procedure as the last step;

5. Construct the full integration influence domains:

   (a) Perform a radial search for each Gauss point to select the closest n_{dom} nodes;

6. Construct the reduced integration influence domains with the same procedure as the last step;

7. Calculate the shape functions and its derivatives for the full integration, i.e., the velocity terms shape functions - equations (2.22) and (2.23);

8. Calculate the shape functions for the reduced integration scheme, i.e., the pressure terms shape functions - equations (2.22) and (2.23);

9. Build the stiffness matrix - equations (3.60):

   (a) Loop through every Gauss point to build a local stiffness matrix. In case its the first iteration the calculation will be performed using the initial value of viscosity provided in the input data, otherwise it will use the calculated velocity and strain rate to compute the best viscosity value - equation (3.35) or (3.37);

   (b) Assembly the local stiffness matrix in the global system matrix;

10. Impose boundary conditions:

    (a) Based on input data impose both force and displacement constraints to the respective nodes - equations (3.60).

11. Solve the algebraic system of equations to obtain the nodal velocities - equation (3.62);

12. Compute the pressure on the integration points using equation (3.58);

13. Compute the strain rate at the Gauss points to prepare for the next iterations - equation (3.45);

14. Interpolate the velocity of the Gauss points based on the nodal values - equation (3.39);

15. Calculate an average velocity value of the domain and store it:

    (a) If it is the first iteration jump to point 5 and repeat;

    (b) If it is not the first iteration compare the last two domain average values and if the relative difference is below a cut-off value stop the program as the solution is converged;

    (c) Otherwise, if it is still larger than the cut-off value jump to point 5 and repeat.

Mixed Method

1. Read problem data, input variables and material properties;
2. Construct the nodal discretization:
   (a) Based on the input data construct a regular rectangular mesh;
   (b) If necessary apply a randomization procedure - equation (3.72) - on the existing discretization to construct an irregular mesh;
   (c) Based on the geometrical definition remove specific nodes from the existing discretization to create voids or other geometrical details in the mesh.
3. Construct the integration mesh:
   (a) Create the integration mesh following the isoparametric formulation and the Gaussian quadrature scheme for a $L \times D$ rectangular domain;
   (b) Remove integration points outside the domain (if there exists voids).
4. Construct the reduced integration mesh with a similar procedure as the last step;
5. Construct the full integration influence domains:
   (a) Performs a radial search for each Gauss point to select the closest n_{dom} nodes;
6. Construct the reduced integration influence domains with the same procedure as the last step;
7. Calculate the shape functions and its derivatives for the full integration, i.e., the velocity terms shape functions - equations (2.22) and (2.23);
8. Calculate the shape functions for the reduced integration scheme, i.e., the pressure terms shape functions - equations (2.22) and (2.23);
9. Build the stiffness matrix - equations (3.64) and (3.65):
   (a) Loop through every Gauss point to build a local stiffness matrix. In case its the first iteration the calculation will be performed using the initial value of viscosity provided in the input data, otherwise it will use the calculated velocity and strain rate to compute the best viscosity value - equation (3.35) or (3.37);
   (b) Assembly the local stiffness matrix in the global system matrix - equation (3.68);
10. Impose boundary conditions:
    (a) Based on input data impose both force and displacement constraints to the respective nodes - equations (3.60) and (3.64).
11. Solve the algebraic system of equations to obtain the nodal velocities and pressures - equation (3.69);

12. Compute the strain rate at the Gauss points to prepare for the next iterations - equation (3.45);

13. Interpolate the velocity of the Gauss points based on the nodal values - equation (3.39);

14. Calculate average velocities and pressure values of the domain and store them:

    (a) If it is the first iteration jump to point 5 and repeat;

    (b) If it is not the first iteration compare the last two domain average values for each variable and if both the relative differences are below a cut-off value stop the program as the solution is converged;

    (c) Otherwise, if they're still larger than the cut-off value jump to point 5 and repeat.

Mixed Dual Method

1. Read problem data, input variables and material properties;

2. Construct the nodal discretizations:

    (a) Based on the input data construct a regular rectangular mesh;

    (b) Construct a second less dense rectangular mesh with every other node from the previous mesh;

    (c) If necessary apply a randomization procedure - equation (3.72) - on the existing discretizations to construct irregular meshes;

    (d) Based on the geometrical definition remove specific nodes from the existing discretizations to create voids or other geometrical details in the meshes.

3. Construct the integration mesh:

    (a) Create the integration mesh following the isoparametric formulation and the Gaussian quadrature scheme for a $L \times D$ rectangular domain;

    (b) Remove integration points outside the domain (if there exists voids).

4. Construct the velocity influence domains:

    (a) Performs a radial search for each Gauss point to select the closest n_{dom} nodes;

5. Construct the pressure influence domains:

    (a) From the velocity influence domain remove every node that is not in the pressure discretization.

6. Calculate the shape functions and its derivatives for the the velocity influence domains - equations (2.22) and (2.23);

7. Calculate the shape functions for the pressure influence domains - equations (2.22) and (2.23);

8. Build the stiffness matrix - equations (3.64) and (3.65):
   (a) Loop through every Gauss point to build a local stiffness matrix. In case its the first iteration the calculation will be performed using the initial value of viscosity provided in the input data, otherwise it will use the calculated velocity and strain rate to compute the best viscosity value - equation (3.35) or (3.37);
   (b) Assembly the local stiffness matrix in the global system matrix - equation (3.68);
9. Impose boundary conditions:
   (a) Based on input data impose both force and displacement constraints to the respective nodes - equations (3.64) and (3.60).
10. Solve the algebraic system of equations to obtain the nodal velocities and pressures - equation (3.69);
11. Compute the strain rate at the Gauss points to prepare for the next iterations - equation (3.45);
12. Interpolate the velocity of the Gauss points based on the nodal values - equation (3.39);
13. Calculate average velocities and pressure values of the domain and store them:
   (a) If it is the first iteration jump to point 4 and repeat;
   (b) If it is not the first iteration compare the last two domain average values for each variable and if both the relative differences are below a cut-off value stop the program as the solution is converged;
   (c) Otherwise, if they're still larger than the cut-off value jump to point 4 and repeat.

3.3.2 Time Stepped Procedure

Since this method is based on a Lagrangian approach, it is capable to update the mesh and perform the simulation at different time steps, allowing to understand what happens in the process with time. The procedure implemented to run several time steps is not much different from the general static procedure. As an example it will be described for the mixed dual method with the changes highlighted in bold,

1. Read problem data, input variables and material properties;
2. Construct the nodal discretizations:
   (a) Based on the input data construct a regular rectangular mesh;
   (b) Construct a second less dense rectangular mesh with every other node from the previous mesh;
   (c) If necessary apply a randomization procedure - equation (3.72) - on the existing discretizations to construct irregular meshes;

(d) Based on the geometrical definition remove specific nodes from the existing discretizations to create voids or other geometrical details in the meshes.

3. Construct the integration mesh:

   (a) Create the integration mesh following the isoparametric formulation and the Gaussian quadrature scheme for a $L \times D$ rectangular domain;

   (b) Remove integration points outside the domain (if there exists voids).

4. Construct the velocity influence domains:

   (a) Performs a radial search for each Gauss point to select the closest n_{dom} nodes;

5. Construct the pressure influence domains:

   (a) From the velocity influence domain remove every node that is not in the pressure discretization.

6. Calculate the shape functions and its derivatives for the the velocity influence domains - equations (2.22) and (2.23);

7. Calculate the shape functions for the pressure influence domains - equations (2.22) and (2.23);

8. Build the stiffness matrix - equations (3.64) and (3.65):

   (a) Loop through every Gauss point to build a local stiffness matrix. In case its the first iteration the calculation will be performed using the initial value of viscosity provided in the input data, otherwise it will use the calculated velocity and strain rate to compute the best viscosity value - equation (3.35) or (3.37);

   (b) Assembly the local stiffness matrix in the global system matrix - equation (3.68);

9. Impose boundary conditions:

   (a) Based on input data impose both force and displacement constraints to the respective nodes - equations (3.64) and (3.60);

   (b) **Save the nodal information about the boundary in which velocities are imposed, since it is imperative to keep track of these nodes moving through space;**

10. Solve the algebraic system of equations to obtain the nodal velocities and pressures - equation (3.69);

11. Compute the strain rate at the Gauss points to prepare for the next iterations - equation (3.45);

12. Interpolate the velocity of the Gauss points based on the nodal values - equation (3.39);

13. Calculate average velocities and pressure values of the domain and store them:

    (a) If it is the first iteration jump to point 4 and repeat;

    (b) If it is not the first iteration compare the last two domain average values for each variable and if both the relative differences are larger than a cut-off value jump to point 4 and repeat;

    (c) **Otherwise, if they're smaller than the cut-off value then the program has converged and it is time to perform a time step, jump to next step.**

14. **Update nodal spatial coordinates and integration point coordinates based on their velocity;**

$$\begin{aligned} x_{new} &= x_{old} + \tilde{v}_x \Delta t \\ y_{new} &= y_{old} + \tilde{v}_y \Delta t \end{aligned} \tag{3.73}$$

15. **With new nodal spatial coordinates jump to point 4 to calculate the next time step. Repeat until the desired time step is reached.**

This page has been intentionally left blank.

Chapter 4

Preliminary Results

In this chapter the formulations described in the previous chapter will be studied and compared with literature results. The goal is to validate the formulations, see which one provides the best results and to find what are the best parameters for the analysis. Parameters such as order of integration, number of nodes in the influence domain, grid independence and nodal density will be studied in the following manner:

1. Order of integration - using a high nodal density and a high number of nodes inside the influence domains, the order of integration will be studied with increasing values of $quado/quado_{red}$.;

2. Nodes in the influence domain - using the previously determined order of integration and the same high nodal density, influence domains will be tested with different n_{dom};

3. Mesh independence - in order to test the robustness of the method, and its independence to a structured grid, several meshes with increasing degrees of irregularity (λ) will analysed. The order of integration and number of nodes in the influence domains will be the previously determined. As for the mesh, the same high nodal density will be adopted;

4. Convergence study - using all the above optimized parameters, the mesh density is analysed. Therefore several discretizations will be tested, each one with increasing number of nodes.

In order to validate the results, a meshless study by *Greco et al.* was selected [2]. In this study the problem of isothermal transient extrusion is studied using a fairly recent meshless method and a well-established FEM package (Deform2D) for forming processes. The problem domain depicted in Figure 4.1 is composed of a square of material, in the left border a velocity is imposed and the material is allowed to flow parallel to the symmetry line (top border) and the nozzle (bottom and right borders). In the right border a opening exists through which the material will flow. The parameters in this example are,

$$\begin{aligned} L = D &= 300\,\text{mm}, \\ v &= 3\,\text{mm/s}. \end{aligned} \tag{4.1}$$

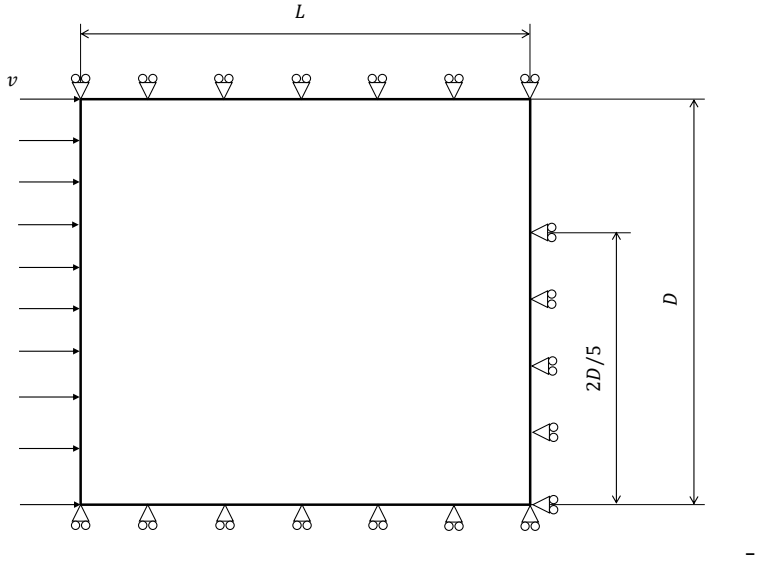


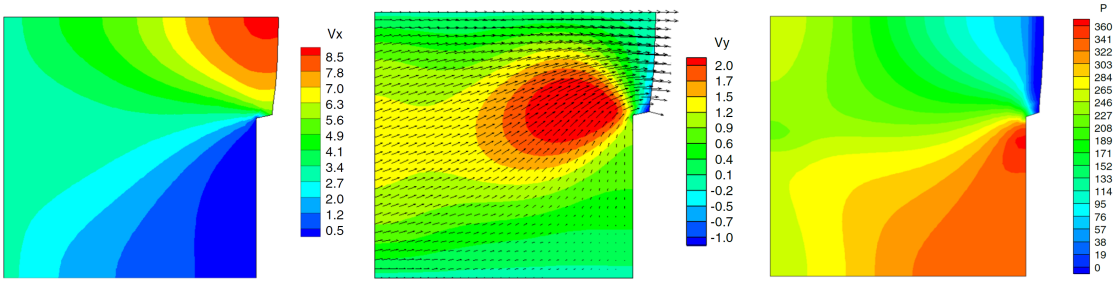
Figure 4.1: Schematic representation of model studied.

This problem will be analysed with the material law defined in equation (3.37) with the properties in Table 4.1 common for some aluminium alloys.

Table 4.1: Material properties used in simulation [2],

Parameter	Value
μ_0	150 MPa · s
n	0,2

For reference, in Figure 4.2 the results documented in literature are represented.



(a) Velocity in x [mm/s]. (b) Velocity in y [mm/s]. (c) Pressure [MPa].

Figure 4.2: Reference results from the meshless study [2].

4.1 Direct Method

4.1.1 Order of Integration

In the Direct Method it is important to study the influence of the order of integration in both variables. *Zienkiewicz et al.* recommend the use of reduced integration for the pressure calculation [20]. Thus, both types of integration will be considered and analysed.

For both schemes the nodal mesh is characterized by $divL = divD = 48$ and is represented in Figure 4.3, where each white node has only two velocity degrees of freedom. Also, the influence domains are characterized by $n_{dom} = 18$.

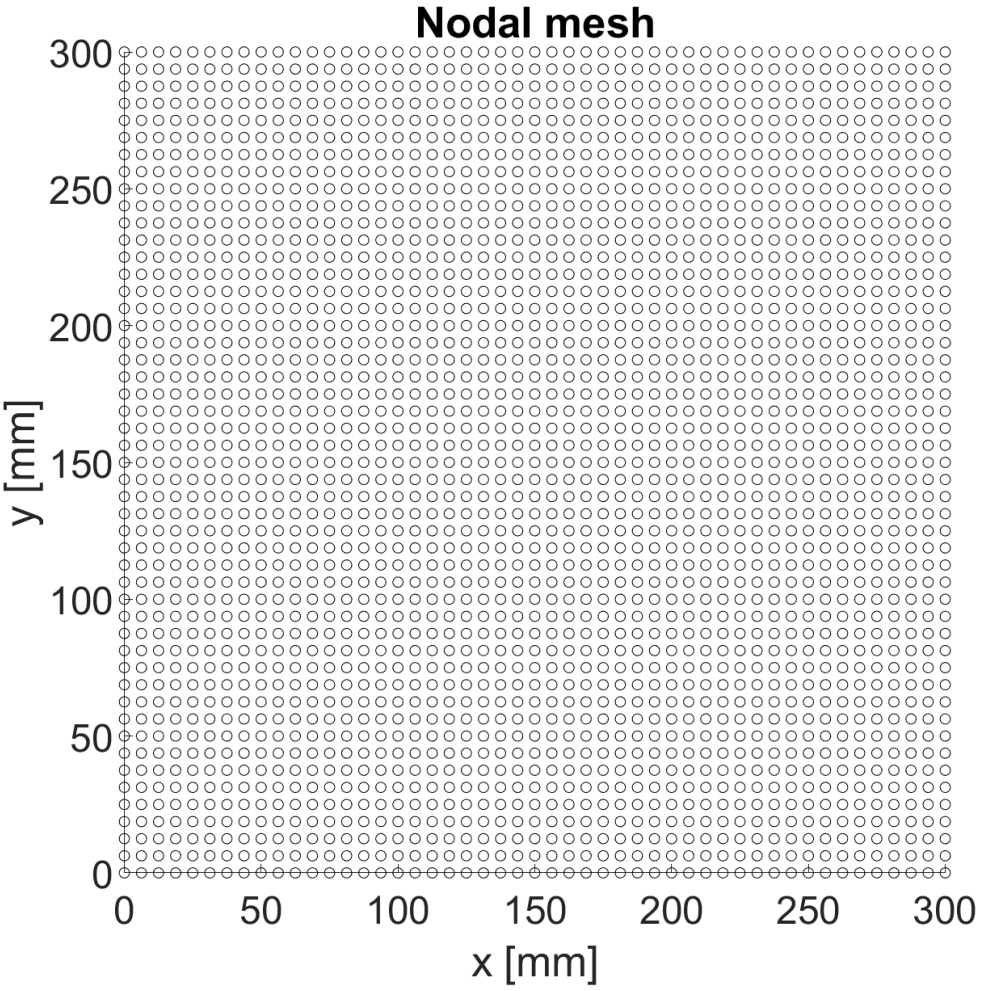
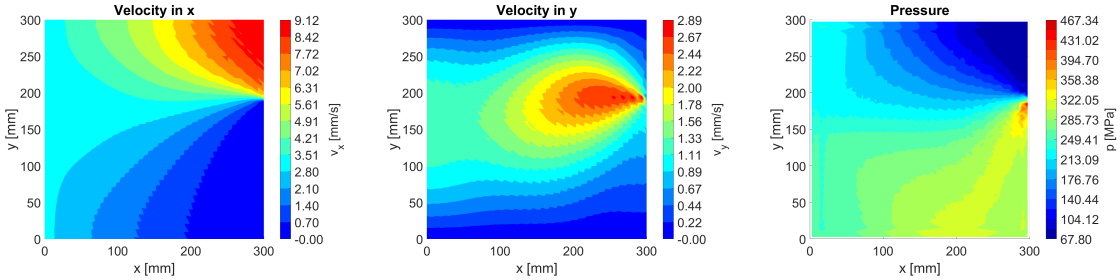


Figure 4.3: Nodal mesh analysed with the direct method $divL = divD = 48$.

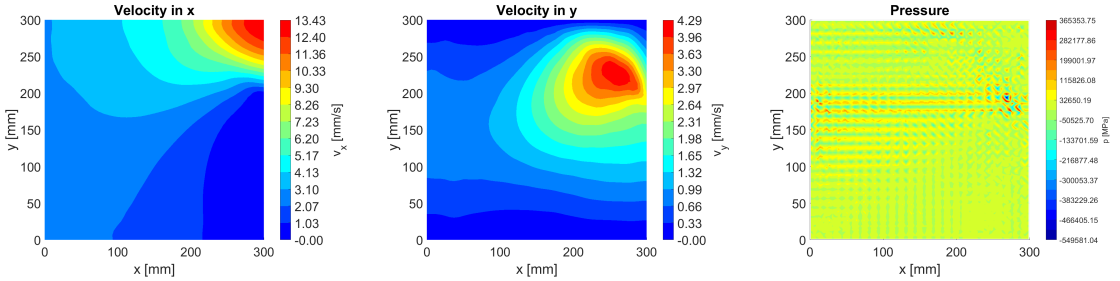
Full Integration

In this scheme of integration, both the pressure and velocity terms will have the same order of integration determined by the variable *quado*. This variable is going to vary from 2 to 10.



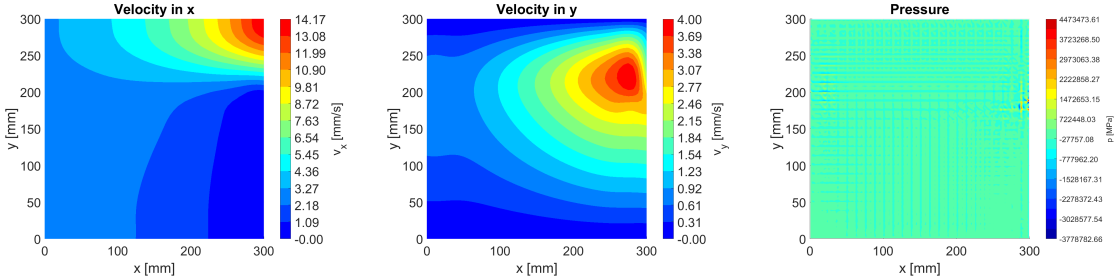
(a) Velocity in x. (b) Velocity in y. (c) Pressure.

Figure 4.4: Results obtained with full integration in the direct method and *quado* = 2.



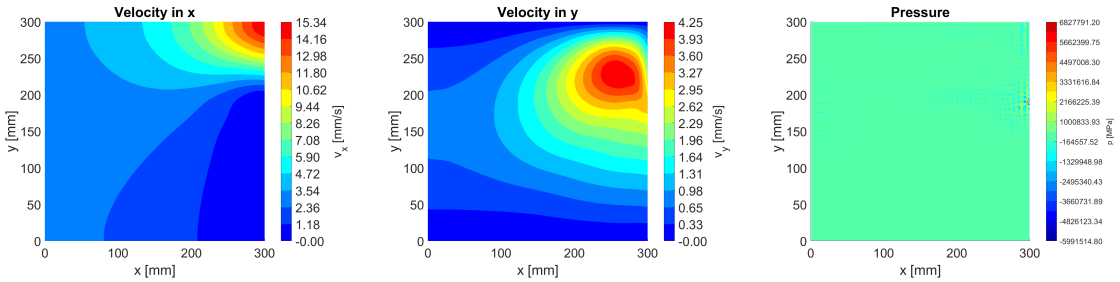
(a) Velocity in x. (b) Velocity in y. (c) Pressure.

Figure 4.5: Results obtained with full integration in the direct method and *quado* = 3.



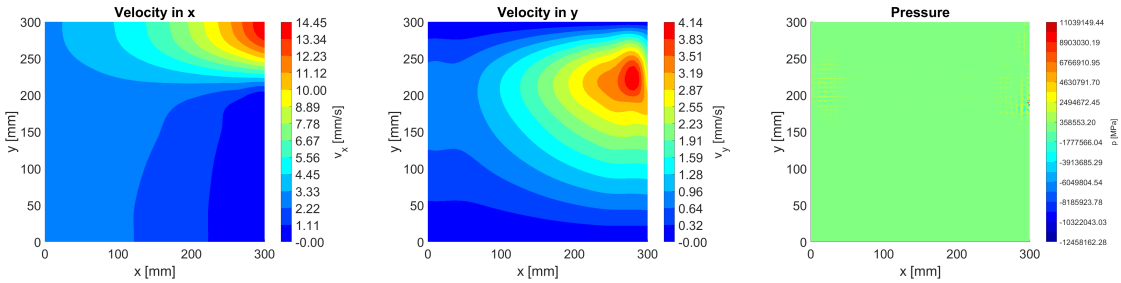
(a) Velocity in x. (b) Velocity in y. (c) Pressure.

Figure 4.6: Results obtained with full integration in the direct method and *quado* = 4.



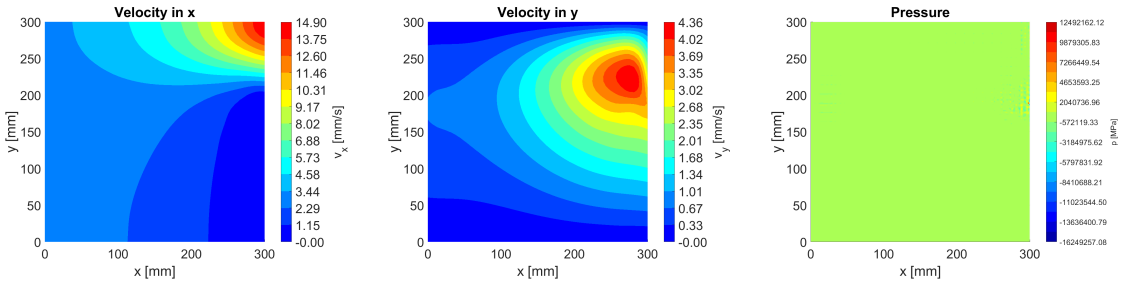
(a) Velocity in x. (b) Velocity in y. (c) Pressure.

Figure 4.7: Results obtained with full integration in the direct method and *quado* = 5.



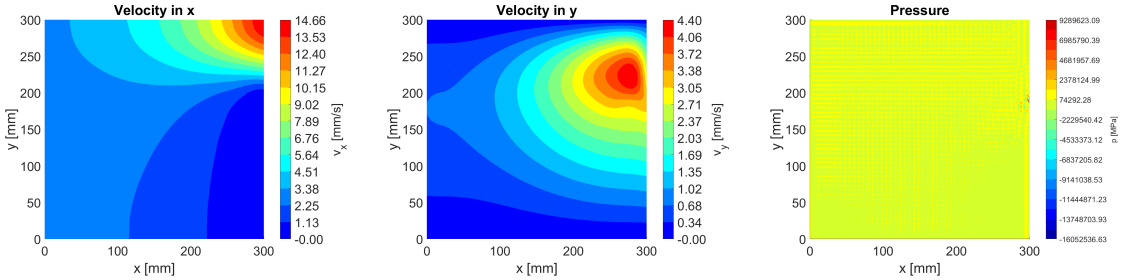
(a) Velocity in x. (b) Velocity in y. (c) Pressure.

Figure 4.8: Results obtained with full integration in the direct method and *quado* = 6.



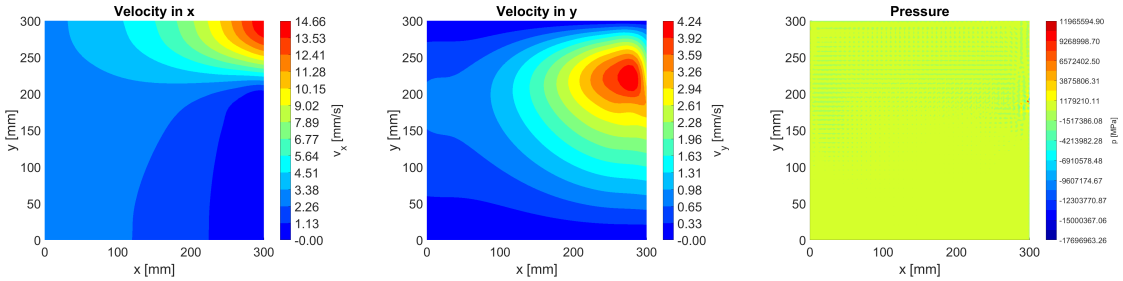
(a) Velocity in x. (b) Velocity in y. (c) Pressure.

Figure 4.9: Results obtained with full integration in the direct method and *quado* = 7.



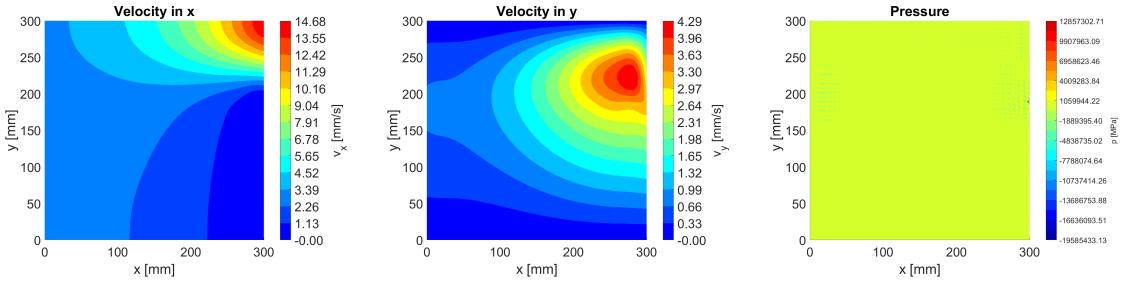
(a) Velocity in x. (b) Velocity in y. (c) Pressure.

Figure 4.10: Results obtained with full integration in the direct method and *quado* = 8.



(a) Velocity in x. (b) Velocity in y. (c) Pressure.

Figure 4.11: Results obtained with full integration in the direct method and *quado* = 9.



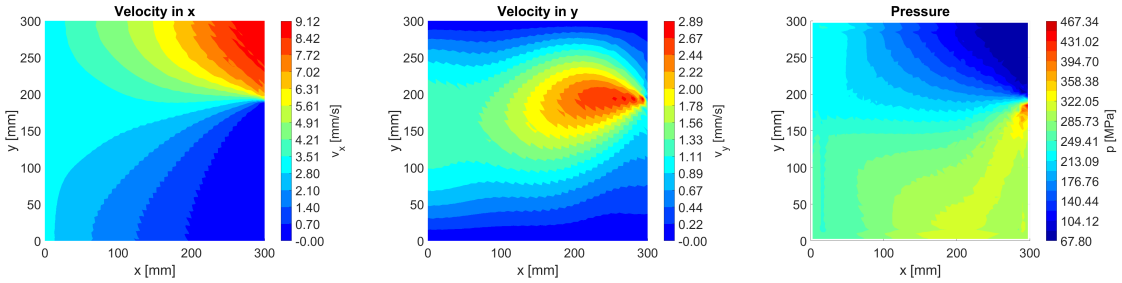
(a) Velocity in x. (b) Velocity in y. (c) Pressure.

Figure 4.12: Results obtained with full integration in the direct method and *quado* = 10.

There are two particularities that stand out in these results. The first one is the slight fluctuations in the 2^{nd} order integration visible in both the velocities and pressure. Although these fluctuations affect the quality of the results, they do not affect its numerical validity, as the results are very close to those obtained in the study [2]. These fluctuations seem to only occur in this order of integration, since the following ones do not present the mentioned fluctuations. However, the second detail to note is that from the 3^{rd} order of integration onwards the solution seems to experience a locking phenomenon. This phenomenon lead the velocity fields to report higher values than it is supposed to and regarding the pressure fields, it loses all its relevant information.

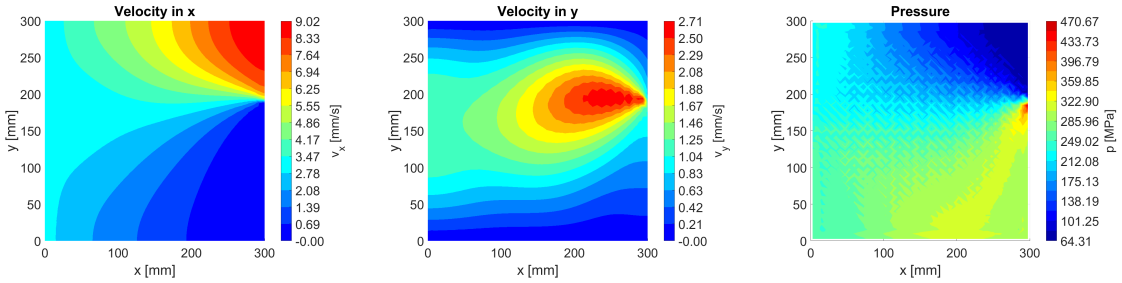
Hybrid Integration

In order to overcome the locking verified in the full integration scheme a hybrid integration scheme was studied, following the recommendation of *Zienkiewicz et al.* [20]. In this scheme, the order of integration for the velocity terms, *quado*, varies from 2 to 10 as usual, but the pressure side, $quado_{red}$, remains locked throughout the process with a 2^{nd} order integration. The results were as follows:



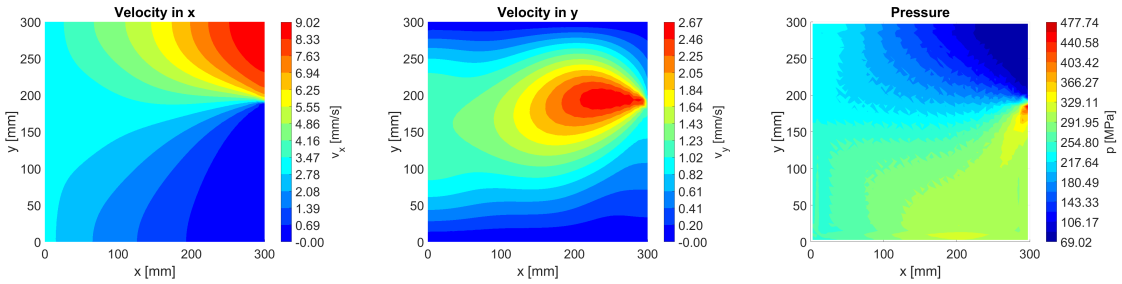
(a) Velocity in x. (b) Velocity in y. (c) Pressure.

Figure 4.13: Results obtained with hybrid integration in the direct method and $quado = 2$.



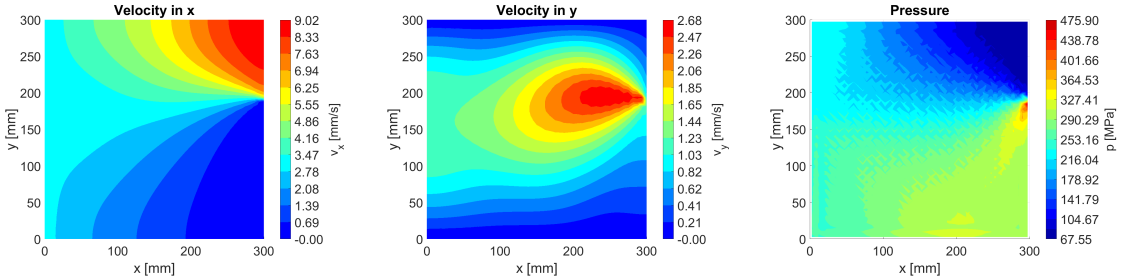
(a) Velocity in x. (b) Velocity in y. (c) Pressure.

Figure 4.14: Results obtained with hybrid integration in the direct method and $quado = 3$.



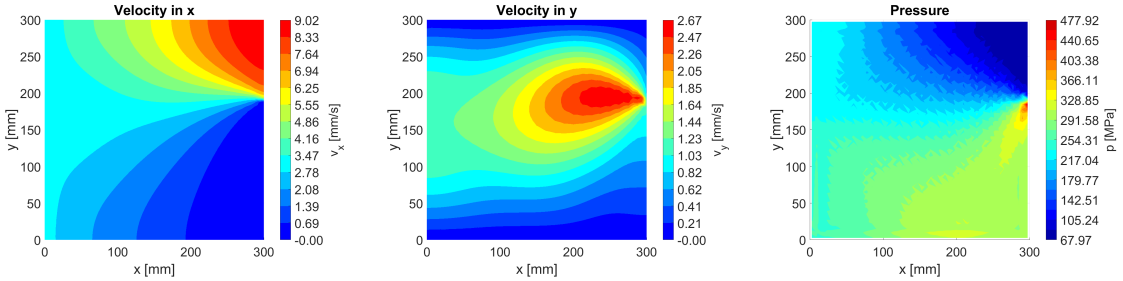
(a) Velocity in x. (b) Velocity in y. (c) Pressure.

Figure 4.15: Results obtained with hybrid integration in the direct method and $quado = 4$.



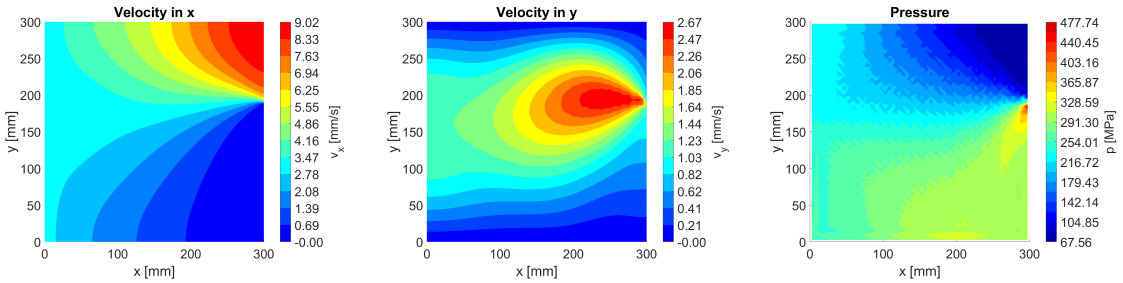
(a) Velocity in x. (b) Velocity in y. (c) Pressure.

Figure 4.16: Results obtained with hybrid integration in the direct method and $quado = 5$.



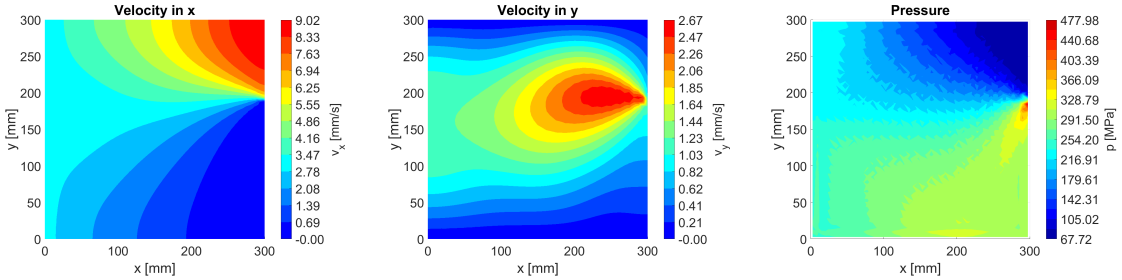
(a) Velocity in x. (b) Velocity in y. (c) Pressure.

Figure 4.17: Results obtained with hybrid integration in the direct method and $quado = 6$.



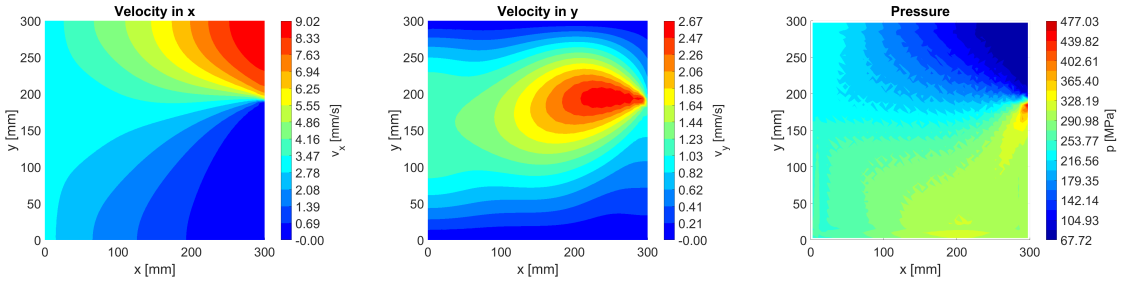
(a) Velocity in x. (b) Velocity in y. (c) Pressure.

Figure 4.18: Results obtained with hybrid integration in the direct method and $quado = 7$.



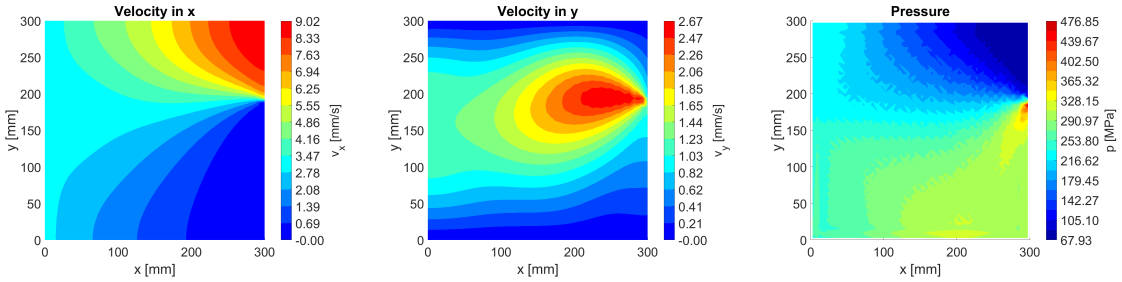
(a) Velocity in x. (b) Velocity in y. (c) Pressure.

Figure 4.19: Results obtained with hybrid integration in the direct method and $quado = 8$.



(a) Velocity in x. (b) Velocity in y. (c) Pressure.

Figure 4.20: Results obtained with hybrid integration in the direct method and $quado = 9$.



(a) Velocity in x. (b) Velocity in y. (c) Pressure.

Figure 4.21: Results obtained with hybrid integration in the direct method and $quado = 10$.

Now, from the results, it is possible to observe that the locking phenomenon is no longer an issue in the higher orders of integration. All results from order 2 to order 10 seem, in a first inspection, in accordance with the ones obtained in literature. This provides confidence in the formulation, and in the method itself. Although, it is also possible to observe that the fluctuations in the solution are still visible. They have disappeared in the velocity fields, confirming the previous hypothesis that the low order of integration was responsible for this issue. However, in the pressure fields this issue is constant, since the order of integration can't rise above 2.

The implemented technique allows to acquire acceptable results for the velocity field. However, the fact that the order of integration in the pressure terms is limited

to 2 makes the method slightly unstable. Since this formulation uses the penalty method, it is prone to verify numerical instabilities which are more frequent with lower orders of integration. This may be the cause of the visible fluctuations. As such, the previously attained confidence on the method now falls in light of this problem. On the other hand, the motivation to find an alternative method to calculate the pressure field arises.

4.2 Mixed Method

The mixed method is the next iteration on the formulation and appears as a way to overcome the pressure fluctuations due to the low integration order of the direct method and also its inherent sensitivity to mesh parameters. In this method the velocity and pressure degrees of freedom share the same nodal discretization but they may be integrated independently. Thus, it is possible to have full and hybrid integration schemes again, as in the direct method.

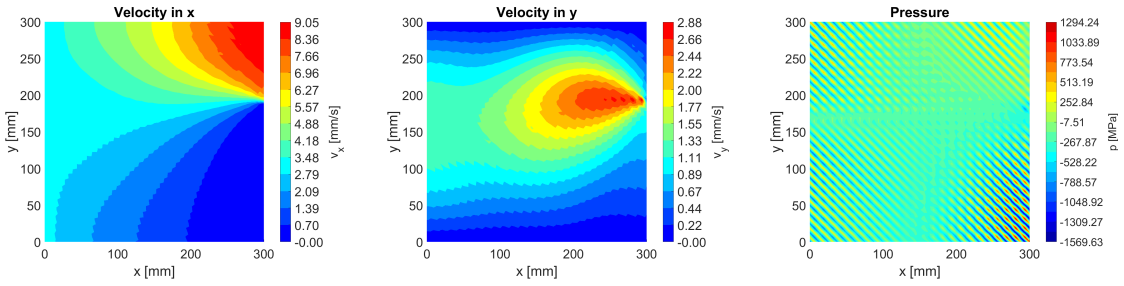
There is the possibility that full integration will lead to similar results with the direct method. It is equally possible that it will yield different results, not showing locking problems due to the fundamentally different formulation. So, once again, analyses assuming both full and hybrid integration schemes will be performed and compared.

4.2.1 Order of Integration

For both integration schemes a nodal mesh with $divL = divD = 48$ was used and can be observed in Figure 4.3. This time, every white node has three degrees of freedom, two associated with velocity and one with pressure. Also, $n_{dom} = 18$ was considered for the size of influence domains.

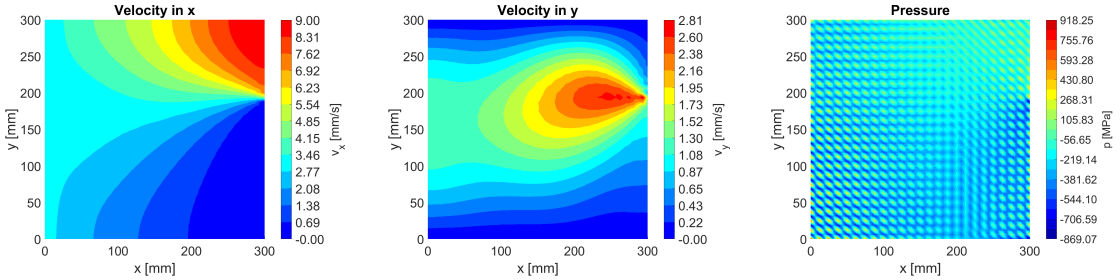
Full Integration

First, it will be considered the same order of integration for both velocity and pressure. Similarly to previous analyses, the order of integration, *quado*, is varied from 2 to 10. The results are as follows:



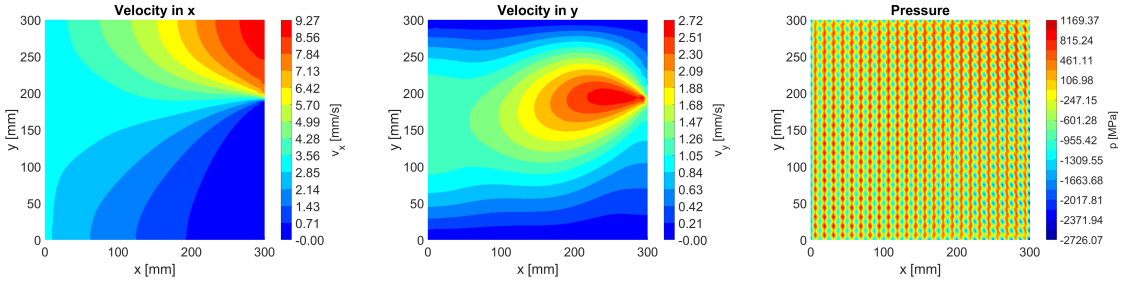
(a) Velocity in x. (b) Velocity in y. (c) Pressure.

Figure 4.22: Results obtained with full integration in the mixed method and *quado* = 2.



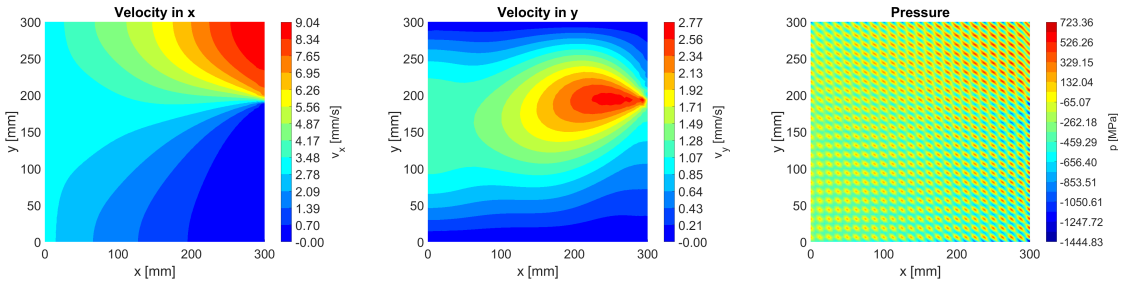
(a) Velocity in x. (b) Velocity in y. (c) Pressure.

Figure 4.23: Results obtained with full integration in the mixed method and *quado* = 3.



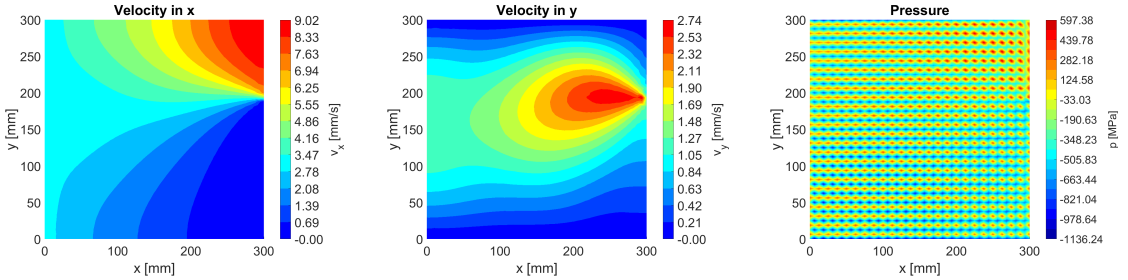
(a) Velocity in x. (b) Velocity in y. (c) Pressure.

Figure 4.24: Results obtained with full integration in the mixed method and *quado* = 4.



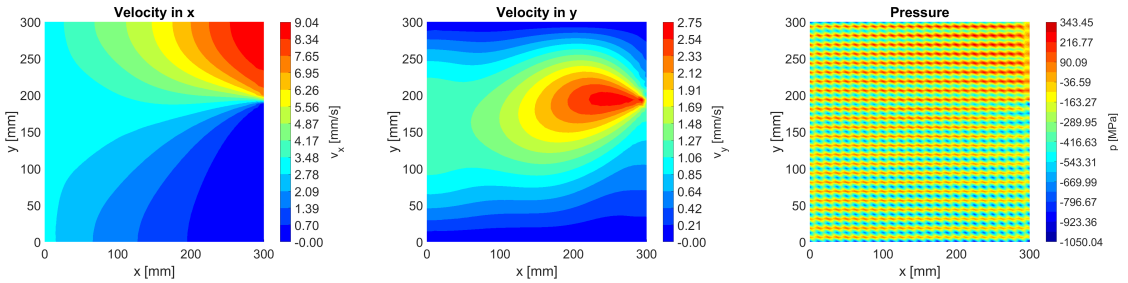
(a) Velocity in x. (b) Velocity in y. (c) Pressure.

Figure 4.25: Results obtained with full integration in the mixed method and *quado* = 5.



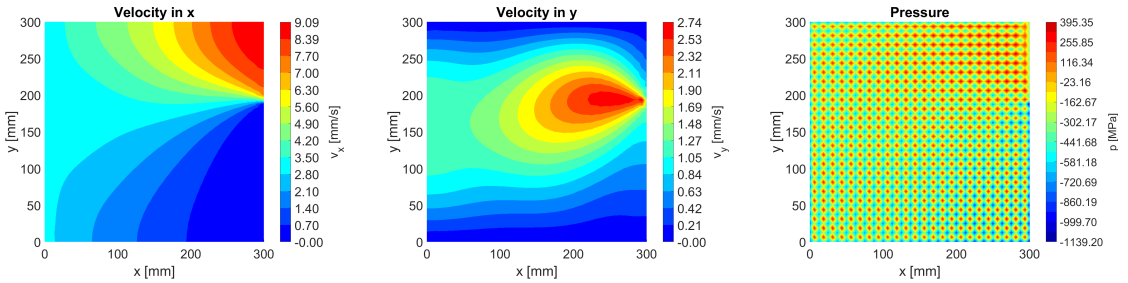
(a) Velocity in x. (b) Velocity in y. (c) Pressure.

Figure 4.26: Results obtained with full integration in the mixed method and *quado* = 6.



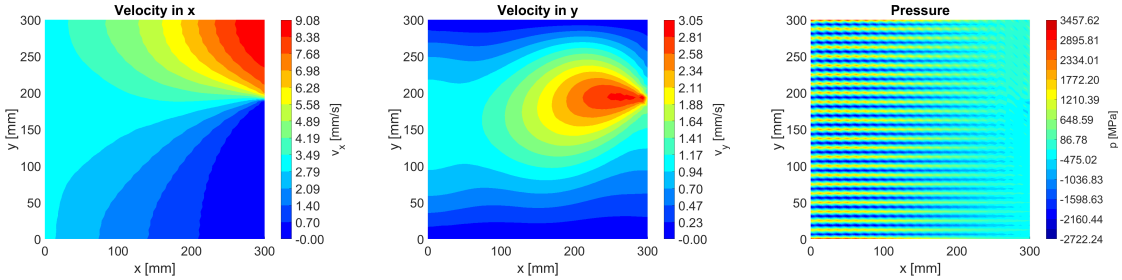
(a) Velocity in x. (b) Velocity in y. (c) Pressure.

Figure 4.27: Results obtained with full integration in the mixed method and *quado* = 7.



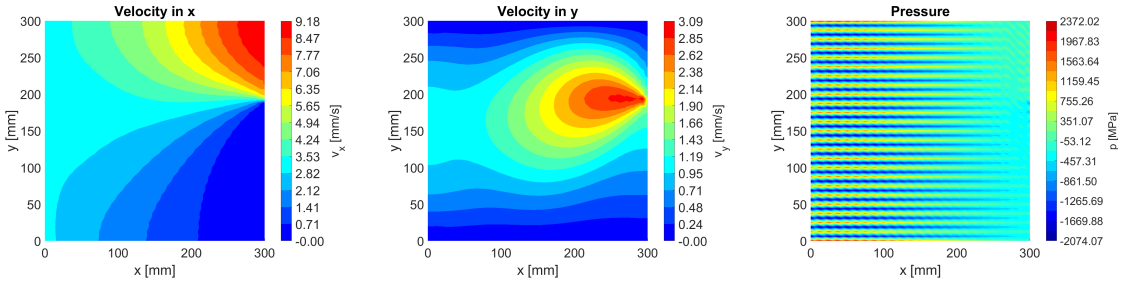
(a) Velocity in x. (b) Velocity in y. (c) Pressure.

Figure 4.28: Results obtained with full integration in the mixed method and *quado* = 8.



(a) Velocity in x. (b) Velocity in y. (c) Pressure.

Figure 4.29: Results obtained with full integration in the mixed method and $quado = 9$.



(a) Velocity in x. (b) Velocity in y. (c) Pressure.

Figure 4.30: Results obtained with full integration in the mixed method and $quado = 10$.

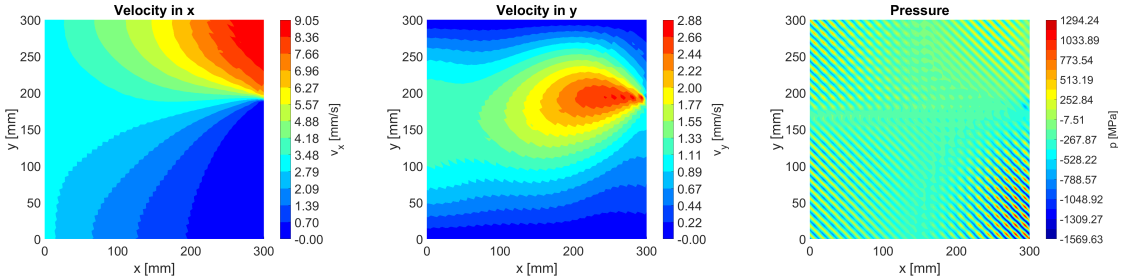
With these results it is possible to observe some peculiarities. First of all, in what concerns the velocity fields, there was some fluctuation in the results of the integration of order 2, which subsided as the integration order increased. The velocity fields appear to be close to the ones previously obtained in the direct method and reported in the literature. Although, an increase in maximum values can be noted as the order increases. This deviation from the expected value can constitute a slight locking problem.

Secondly, and perhaps most notably, is the fact that the pressure fields throughout the entire range of orders of integration did not present one physically valid solution. The results seem to suffer from severe numerical instability regardless of the number of Gauss points available for integration.

In contrast to what was observed in the direct method's results, in which there was a trend after the 2^{nd} order of integration, in this case this is not verified. Thus, the choice of orders of integration for the hybrid scheme is not as easy and obvious as the previous one.

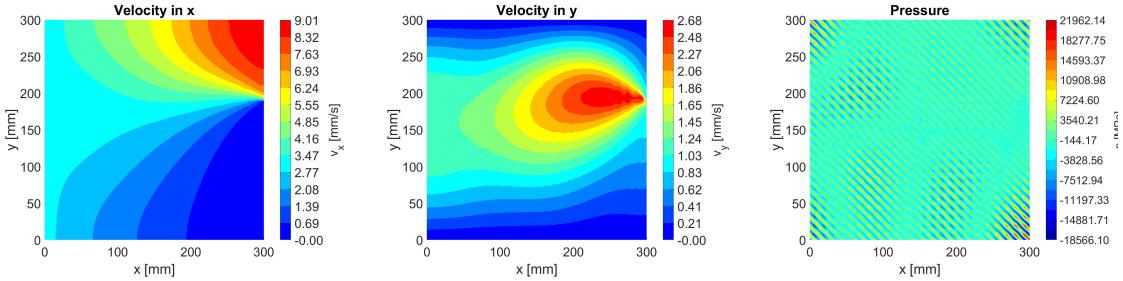
Hybrid Integration

In the absence of further criteria to choose the form of this integration scheme, it seems only right to use the scheme that proved to work previously in the direct method: the pressure terms have its order of integration, $quado_{red}$, locked at 2 while the velocity terms, $quado$, range from the usual 2 to 10.



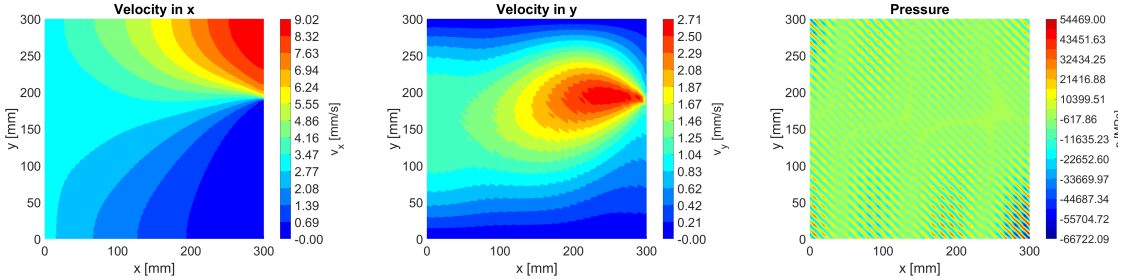
(a) Velocity in x. (b) Velocity in y. (c) Pressure.

Figure 4.31: Results obtained with hybrid integration in the mixed method and $quado = 2$.



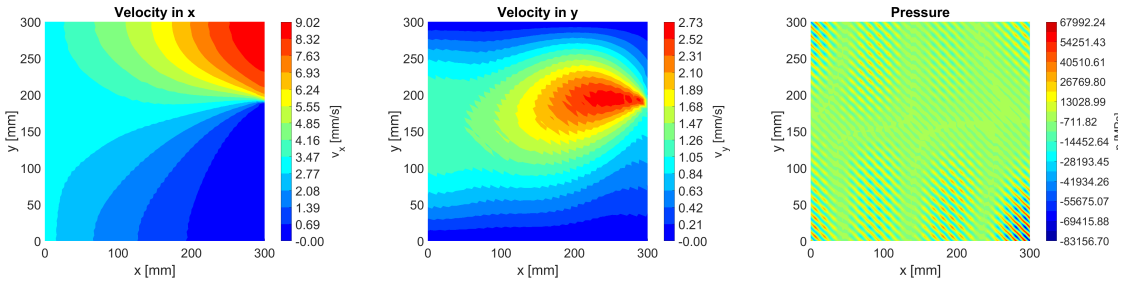
(a) Velocity in x. (b) Velocity in y. (c) Pressure.

Figure 4.32: Results obtained with hybrid integration in the mixed method and $quado = 3$.



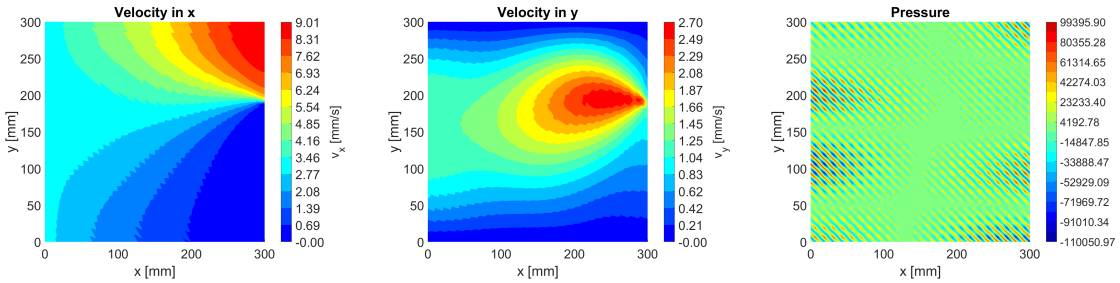
(a) Velocity in x. (b) Velocity in y. (c) Pressure.

Figure 4.33: Results obtained with hybrid integration in the mixed method and $quado = 4$.



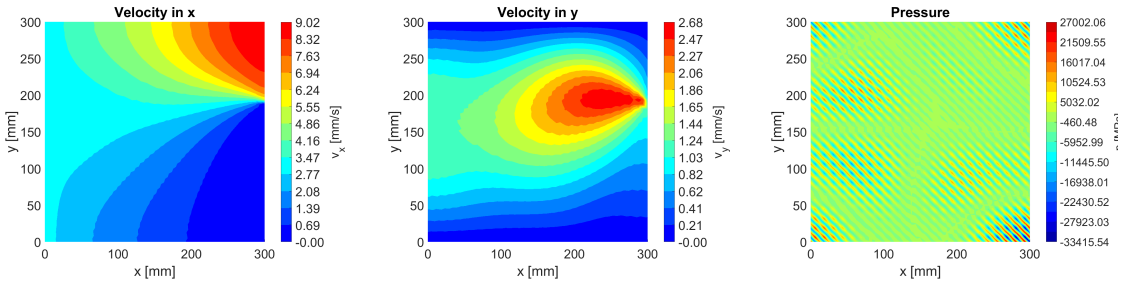
(a) Velocity in x. (b) Velocity in y. (c) Pressure.

Figure 4.34: Results obtained with hybrid integration in the mixed method and $quado = 5$.



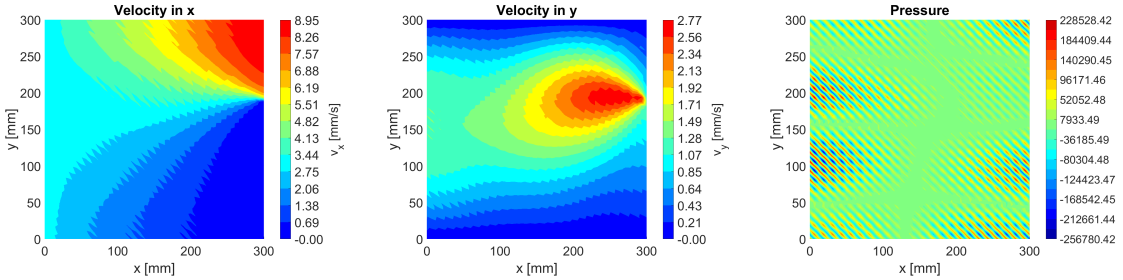
(a) Velocity in x. (b) Velocity in y. (c) Pressure.

Figure 4.35: Results obtained with hybrid integration in the mixed method and $quado = 6$.



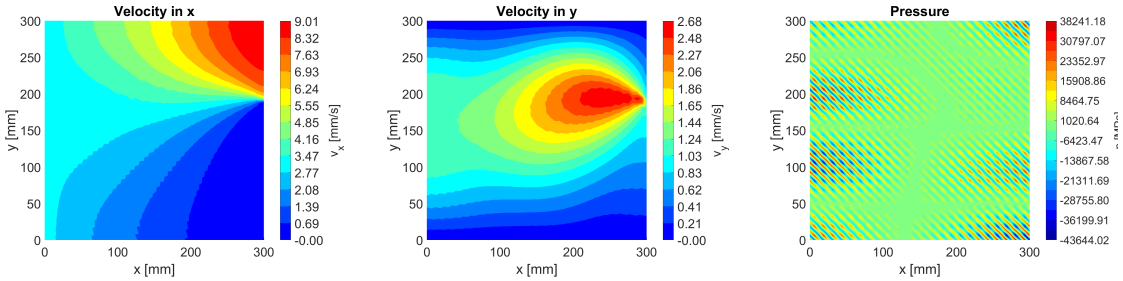
(a) Velocity in x. (b) Velocity in y. (c) Pressure.

Figure 4.36: Results obtained with hybrid integration in the mixed method and $quado = 7$.



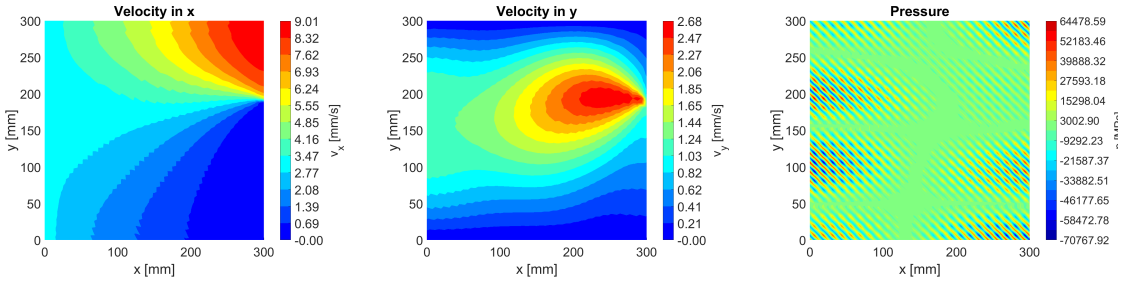
(a) Velocity in x. (b) Velocity in y. (c) Pressure.

Figure 4.37: Results obtained with hybrid integration in the mixed method and $quado = 8$.



(a) Velocity in x. (b) Velocity in y. (c) Pressure.

Figure 4.38: Results obtained with hybrid integration in the mixed method and $quado = 9$.



(a) Velocity in x. (b) Velocity in y. (c) Pressure.

Figure 4.39: Results obtained with hybrid integration in the mixed method and $quado = 10$.

Comparing to the full integration scheme, it is noteworthy to mention that the increase in the maximum values of the velocities is no longer present. The velocity fields once again look in accordance to the expectations, although some minor fluctuations are present in the higher orders of integration, mostly the even numbered ones. These fluctuations are expected due to the choice of low order of integration on the pressure side.

Similarly to what was observed before, the pressure fields failed to present physically valid results throughout the entire range of integration. It appears as though this version of the formulation is as sensitive, if not more, to the numerical instabilities common to a penalty-based formulation. For this reason, this method will

be abandoned in search of another solution for the calculation of both the pressure and velocity fields showing a stable and smooth distribution.

4.3 Mixed Dual Method

This version of the formulation comes as another attempt with the objective to stabilize the solution, particularly the pressure side of the solution. Similarly to the mixed formulation, the pressure is a degree of freedom of the analysis as well as the velocity, but they don't share a nodal discretization this time. In fact, each part has its own nodal mesh and its the integration mesh that is shared. For this reason, there is no longer the distinction between full and hybrid integration schemes, as the order of integration is automatically established due to the different nodal densities in both nodal discretizations.

4.3.1 Order of Integration

Due to the nature of the formulation the order of integration is governed by only one variable, *quado*, and as usual its value will range from 2 to 10, as to study the evolution of the solution with the increase of density of integration points.

The nodal mesh used is the one represented in Figure 4.40 with $divL = divD = 48$ and the nodes with velocity and pressure as degrees of freedom are represented in black and the nodes with just velocity as degree of freedom are represented in white. Also, $n_{dom} = 18$.

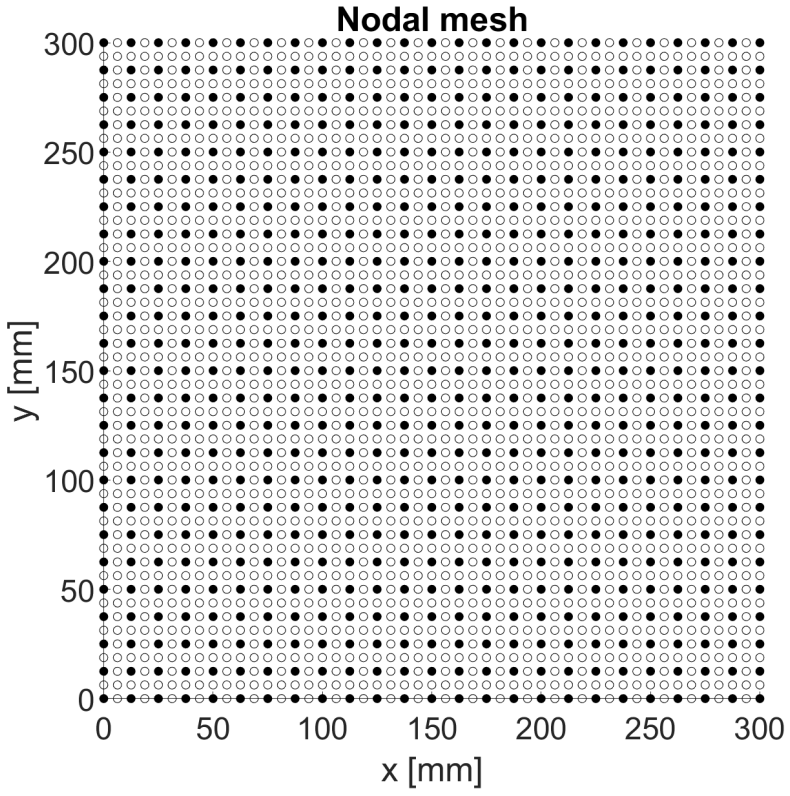
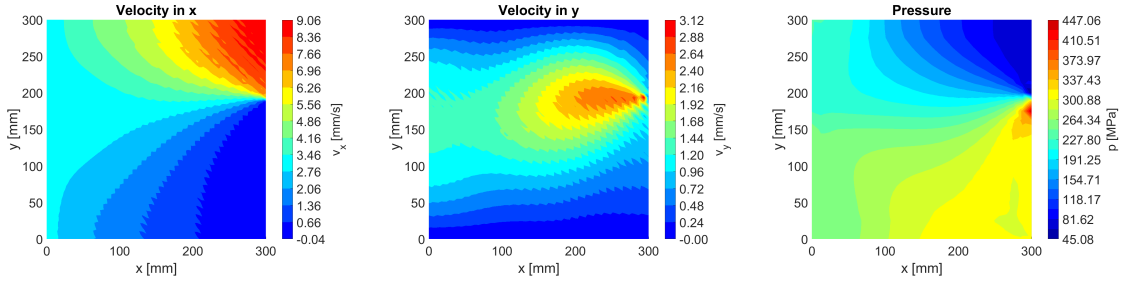


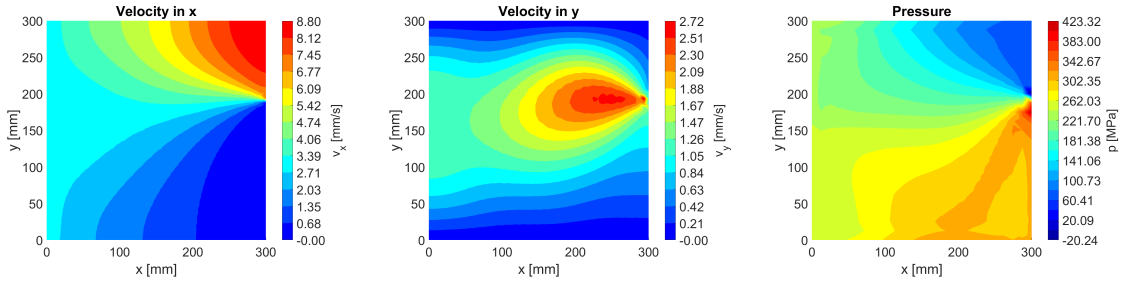
Figure 4.40: Nodal mesh analysed with the mixed dual method.

The solutions came as follows:



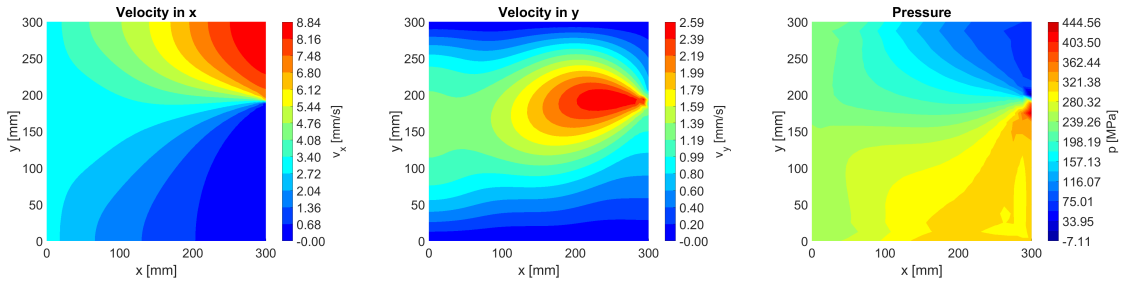
(a) Velocity in x. (b) Velocity in y. (c) Pressure.

Figure 4.41: Results obtained with the mixed dual method and $quado = 2$.



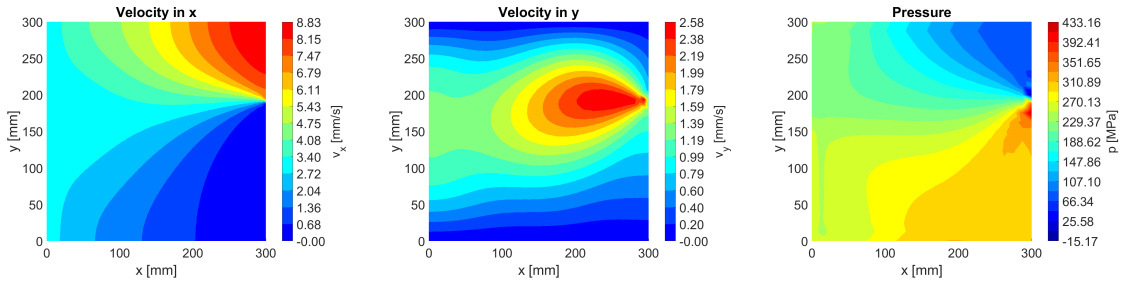
(a) Velocity in x. (b) Velocity in y. (c) Pressure.

Figure 4.42: Results obtained with the mixed dual method and $quado = 3$.



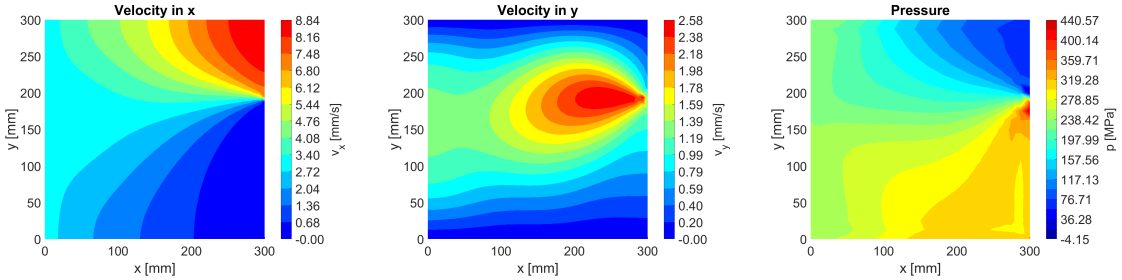
(a) Velocity in x. (b) Velocity in y. (c) Pressure.

Figure 4.43: Results obtained with the mixed dual method and $quado = 4$.



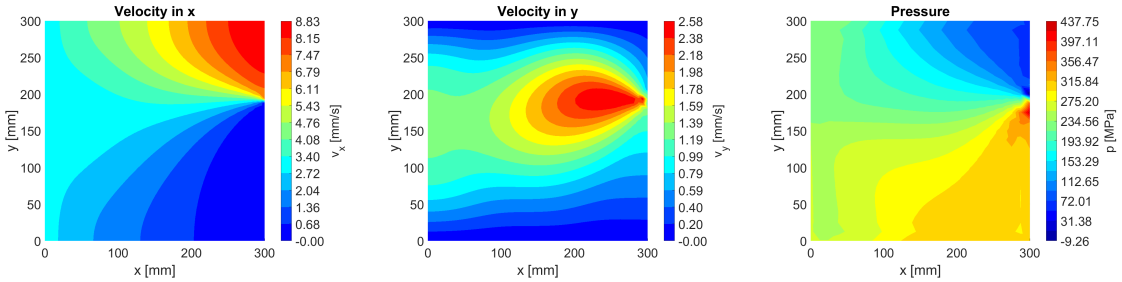
(a) Velocity in x. (b) Velocity in y. (c) Pressure.

Figure 4.44: Results obtained with the mixed dual method and $quado = 5$.



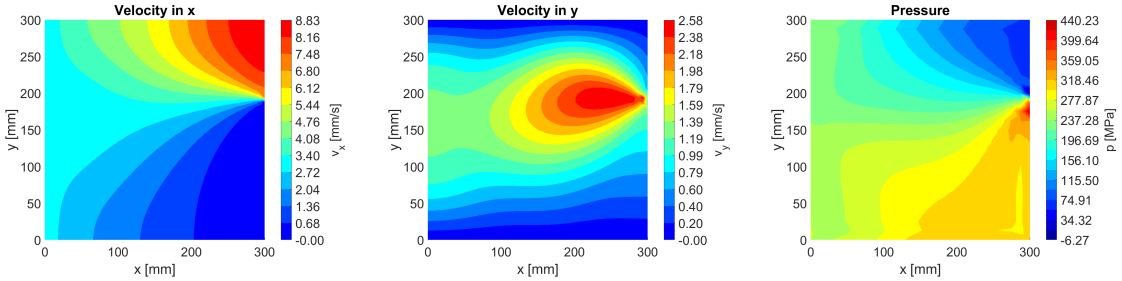
(a) Velocity in x. (b) Velocity in y. (c) Pressure.

Figure 4.45: Results obtained with the mixed dual method and $quado = 6$.



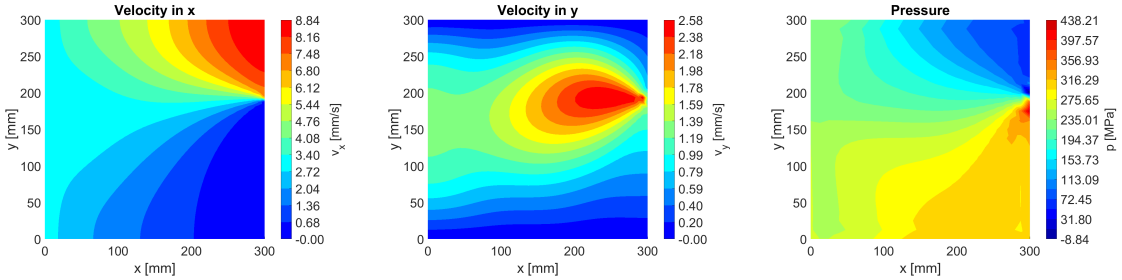
(a) Velocity in x. (b) Velocity in y. (c) Pressure.

Figure 4.46: Results obtained with the mixed dual method and $quado = 7$.



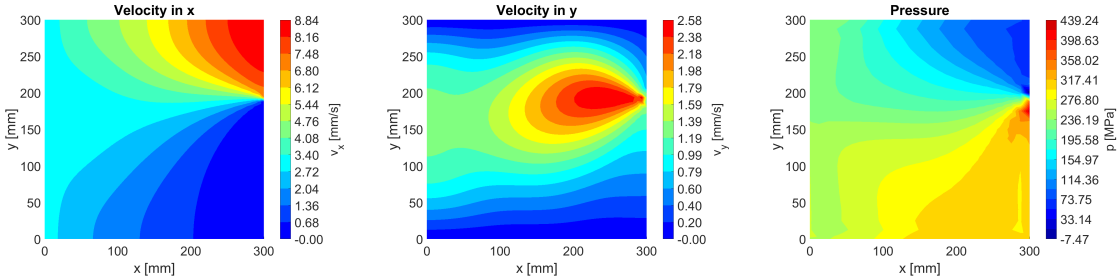
(a) Velocity in x. (b) Velocity in y. (c) Pressure.

Figure 4.47: Results obtained with the mixed dual method and $quado = 8$.



(a) Velocity in x. (b) Velocity in y. (c) Pressure.

Figure 4.48: Results obtained with the mixed dual method and $quado = 9$.



(a) Velocity in x. (b) Velocity in y. (c) Pressure.

Figure 4.49: Results obtained with the mixed dual method and *quado* = 10.

In this set of results, the velocity and pressure fields are closer to the literature results than any other previously attempted formulation within this work. The velocity and pressure gradients are as expected from the physical standpoint. Furthermore, from the visual point of view, no fluctuations are present in neither degree of freedom, except in the lowest order of integration.

It is important now to understand and quantify the evolution of the solution with the increase in the order of integration. Thus, some data was collected from each of the analyses in order to compare the different orders. For this collection, the top most right point was chosen as well as two lines, one horizontal and one vertical as depicted in Figure 4.50.

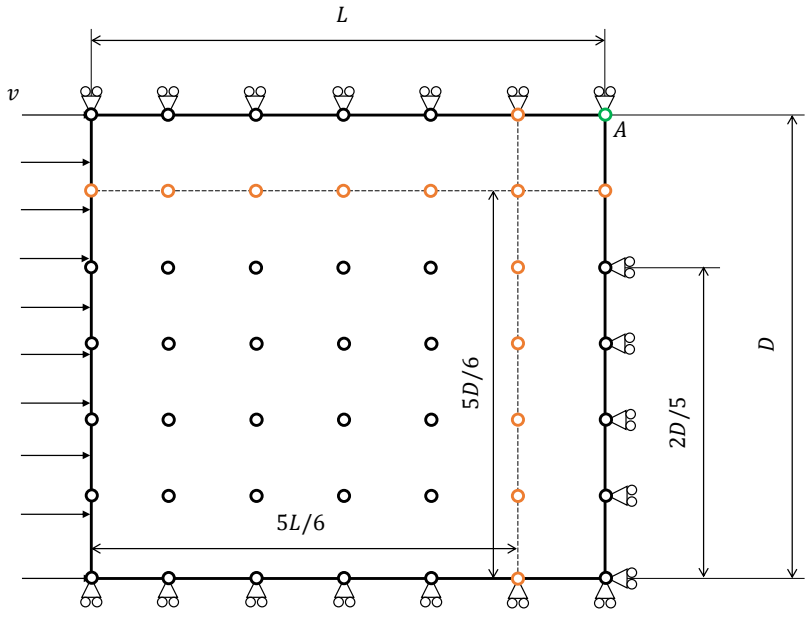


Figure 4.50: Schematic representation of model with the interest point A (green) and lines (orange).

Considering the velocity at point A, and the time it took the program to analyse each order of integration, the plots in Figure 4.51 are obtained.

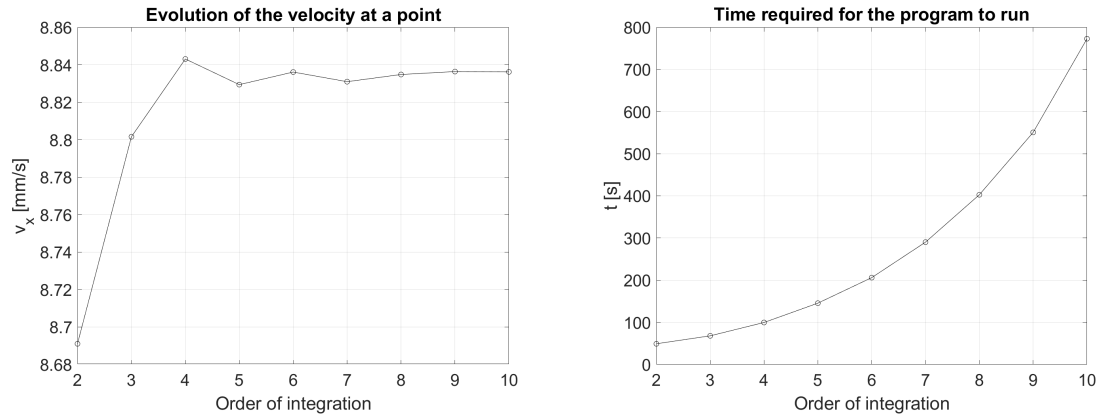
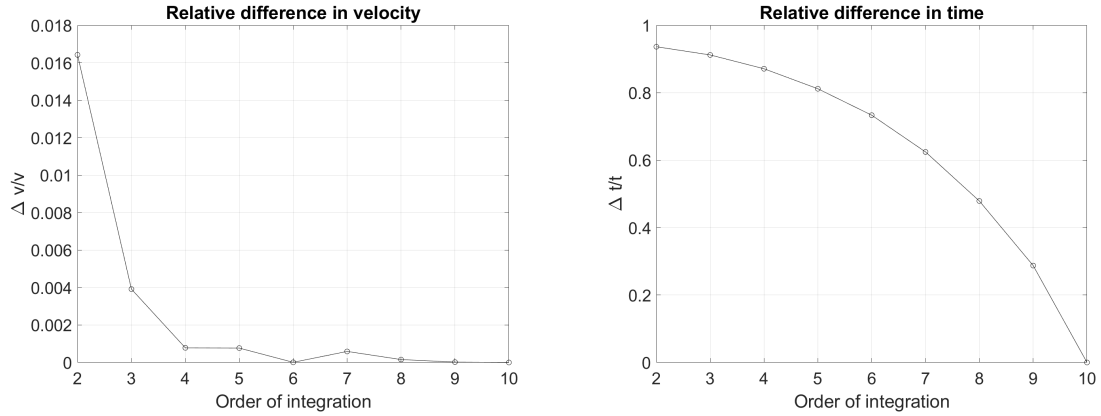


Figure 4.51: Evolution of velocity at a point and the time of computation for each order of integration.

It is possible to observe that the velocity seems to stabilize rapidly after the 4^{th} order of integration and the time of computation follows, as expected, an exponential trend.

One could pose the argument that since the solution appears to converge to a definite value, that using the 10^{th} order of integration is the best way to ensure appropriate results. While this argument as its merit, it is important to remember the time required to compute such order of integration and how that time addition compares to the gain in solution accuracy. To better visualize this effect, the 10^{th} order of integration was considered as reference, and the relative differences (in both velocity and computation time) were calculated. The results are as follows,



(a) Relative difference in velocity. (b) Relative difference in time.

Figure 4.52: Differences in velocity and time relative to the 10^{th} order of integration

It is possible to observe from the 4^{th} order onward the relative difference in velocity gets below $0,2\%$, with the 6^{th}, 8^{th} and 9^{th} being the closest ones to the zero line. Apart from the 10^{th}, which is naturally zero because the computation is in relation to itself.

Although, a good order of integration can be easily selected from Figure 4.52a, the same cannot be said from Figure 4.52b, where a continuous progression is observed and no peaks or notorious jumps stand out. Taking into account the initially

expected values, it can be concluded that in terms of velocity, it is desired the smallest relative difference possible, which would mean a closer value to the reference one. However, in terms of computation time the opposite is preferred, i.e., a large relative difference is desirable since it means it is much smaller than the reference time (which was taken to be the largest of the set).

Thus, it is possible to create a ratio in which both of those factors come in. Defining the relative difference in velocity as $a = \frac{\Delta v}{v}$. And defining the relative difference in time as $b = \frac{\Delta t}{t}$, it is possible to write the following,

$$\text{ratio} = \frac{b}{a} \tag{4.2}$$

Thus, ideally, the relative difference in velocity should be low, which is accomplished with a low a. Also, the relative difference in time should be high, which is achieved with a high b. Therefore, it is aimed to select an integration order leading to a high value of the ratio, equation (4.2). Plotting the ratio, it is possible to obtain the graph of Figure 4.53.

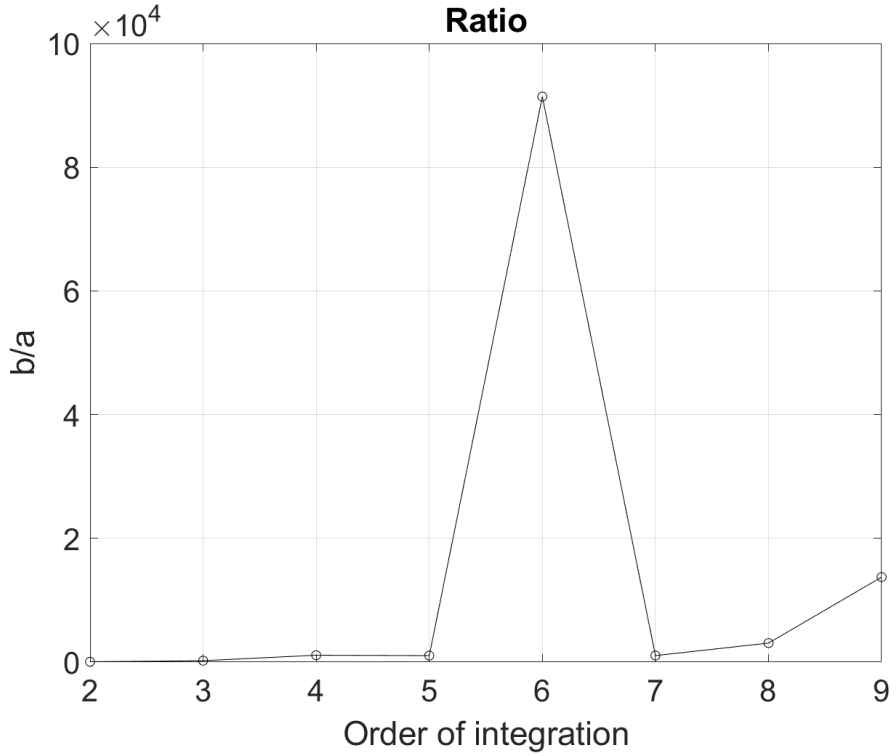


Figure 4.53: Ratio between relative difference in time and relative difference in velocity.

Note that the 10^{th} order is not included because the way this ratio was constructed would mean its ratio would be 0/0. Other than that, the order of integration that stands outs as being the best compromise between solution accuracy and solution computation time is the 6^{th} order of integration. Consequently, this is the order of integration that will be used from this point forward in further analyses.

So far, the results have only been analysed quantitatively. But it is as important to analyse the quality of the results, which can be achieved by comparing (visually) the obtained color maps or by plotting the velocities at the lines earlier specified.

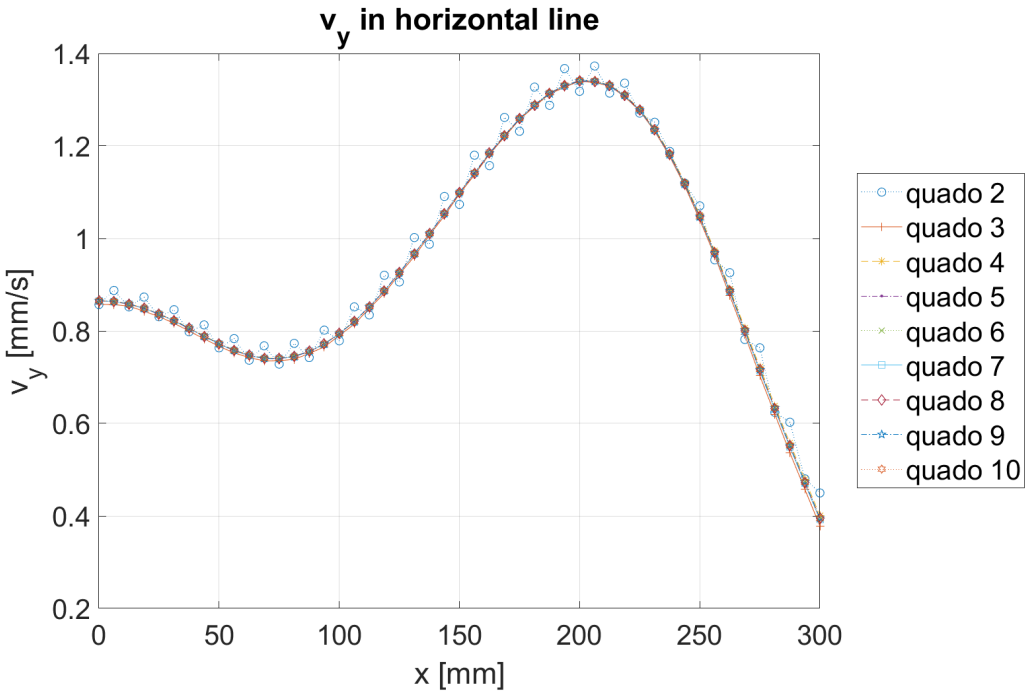


Figure 4.54: Vertical velocity component on the same horizontal line for each order of integration.

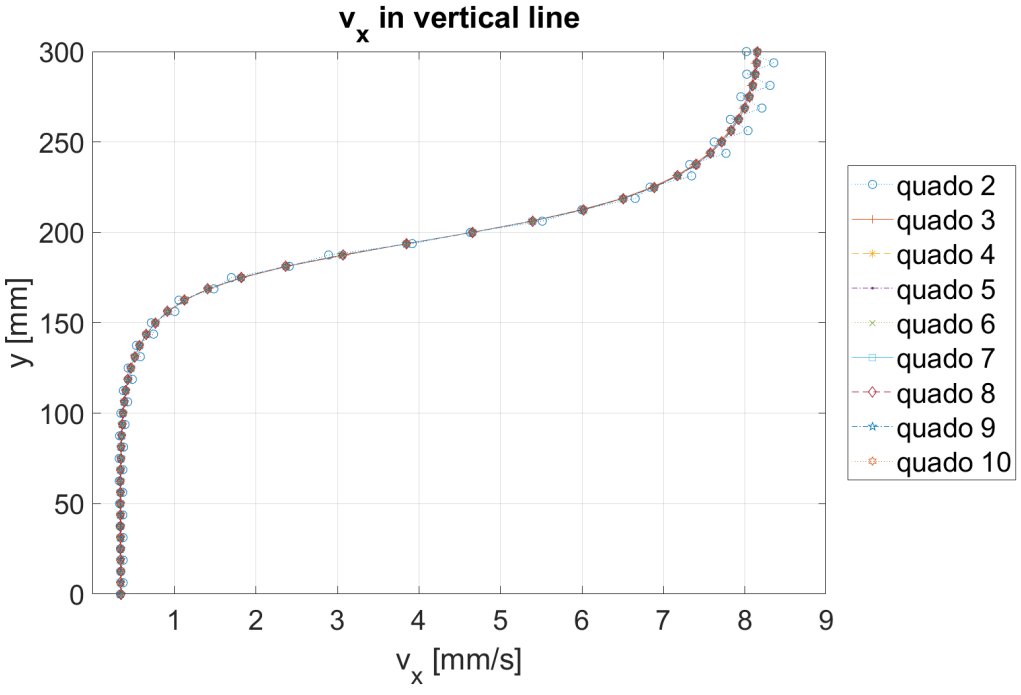


Figure 4.55: Velocity profiles for each order of integration in the same vertical line.

From Figures 4.54 and 4.55 it can observed that the solution of the 2^{nd} order of integration oscillates significantly, which is in accordance with the fluctuations observed in the color maps. Also, it is possible to visualize that the other solutions seem coincident, although this is not the case. To showcase the mentioned difference with more detail, Figure 4.56 zooms in the velocity profiles,

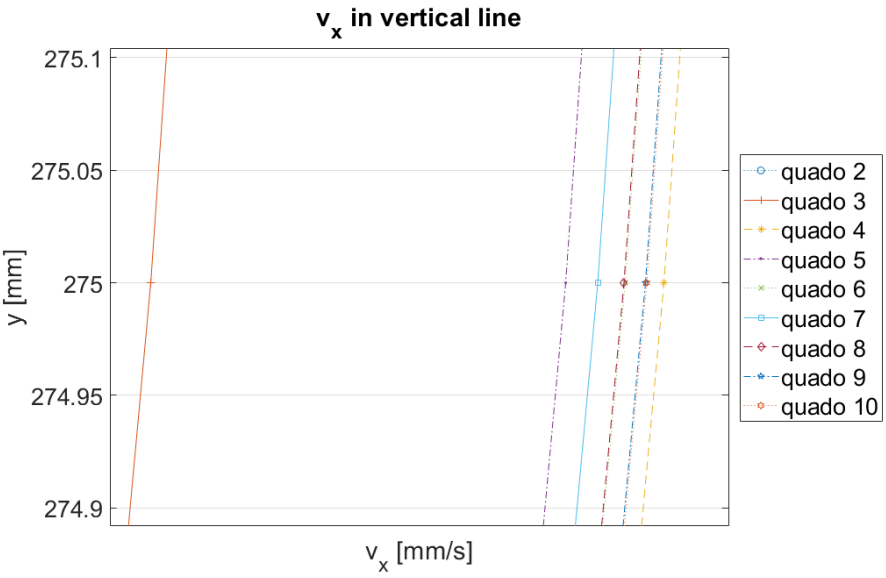


Figure 4.56: Detail of the velocity profiles.

4.3.2 Nodes Inside the Influence Domains

The next step to find the optimum analysis parameters is figuring out a good number of nodes to include in the influence domain. Due to the nature of the mixed dual method, it is only possible to control the number of nodes inside the velocity influence domains, because the pressure ones are built based on the first ones by removing nodes. Therefore, the evolution of the number of nodes inside the influence domain of the velocity variable will be studied, with n_{dom} ranging from 10 to 32.

The nodal mesh used can be observed in Figure 4.57 and has $divL = divD = 48$.

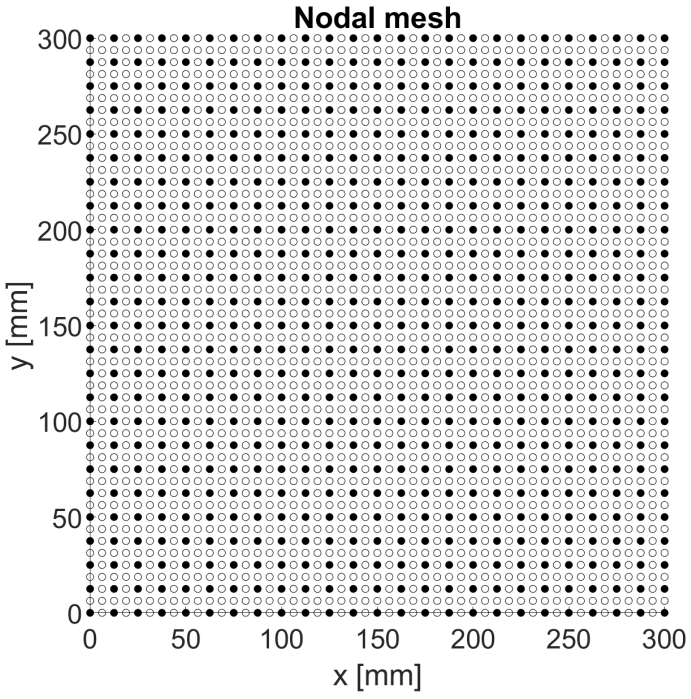
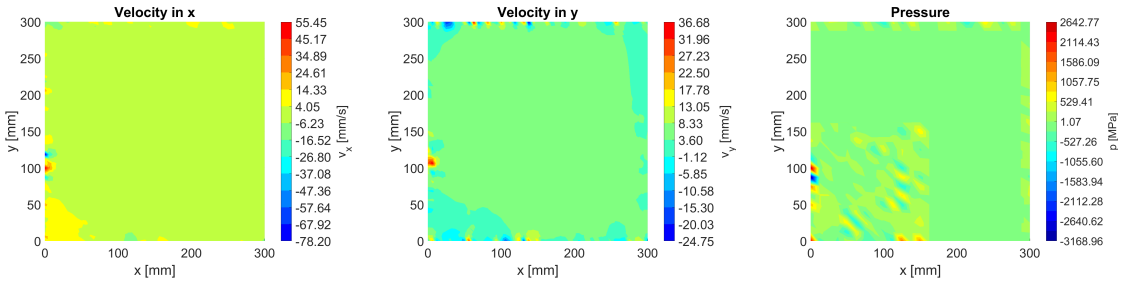
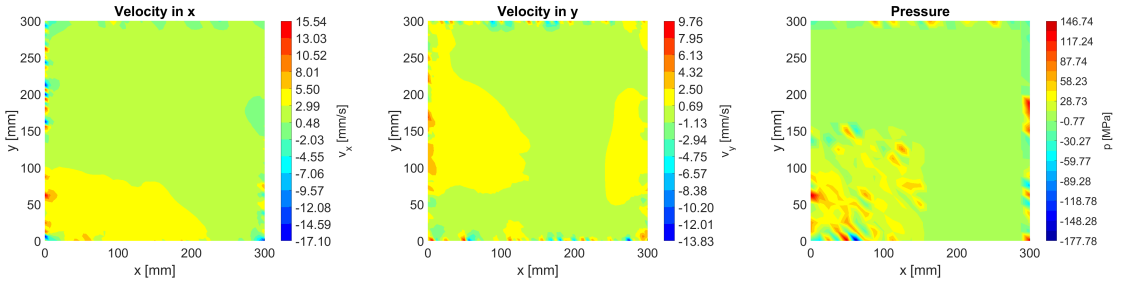


Figure 4.57: Nodal mesh analysed with the mixed dual method.



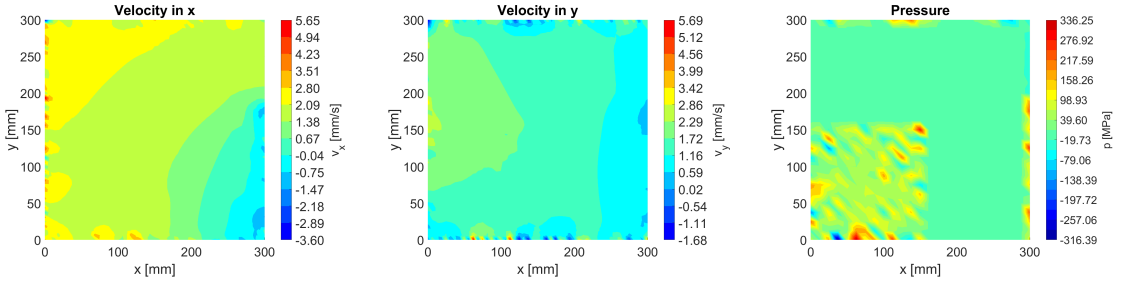
(a) Velocity in x. (b) Velocity in y. (c) Pressure.

Figure 4.58: Results obtained with the mixed dual method and $n_{dom} = 10$.



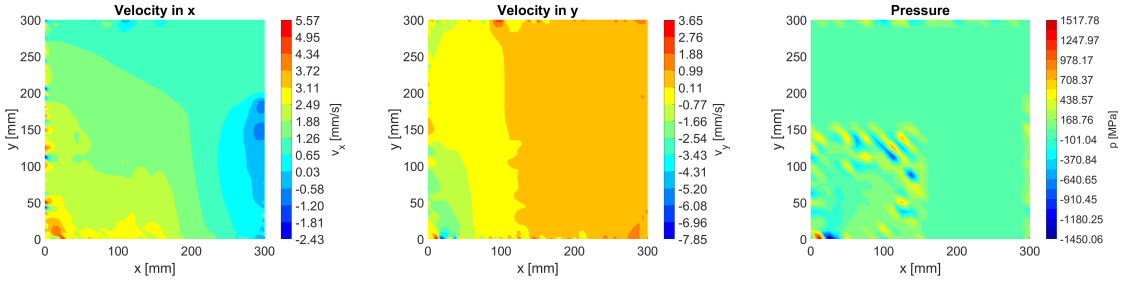
(a) Velocity in x. (b) Velocity in y. (c) Pressure.

Figure 4.59: Results obtained with the mixed dual method and $n_{dom} = 11$.



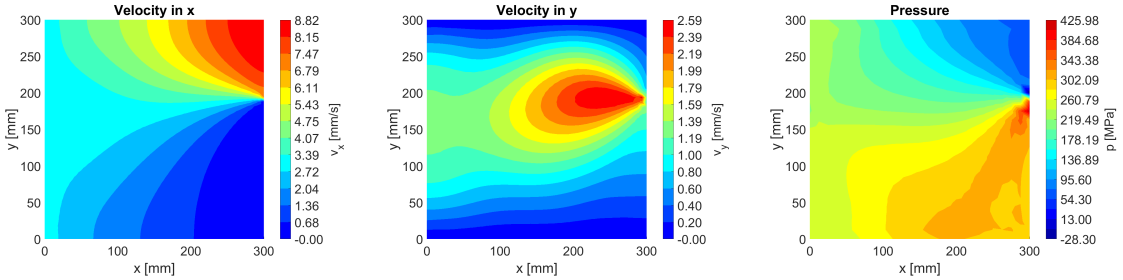
(a) Velocity in x. (b) Velocity in y. (c) Pressure.

Figure 4.60: Results obtained with the mixed dual method and $n_{dom} = 12$.



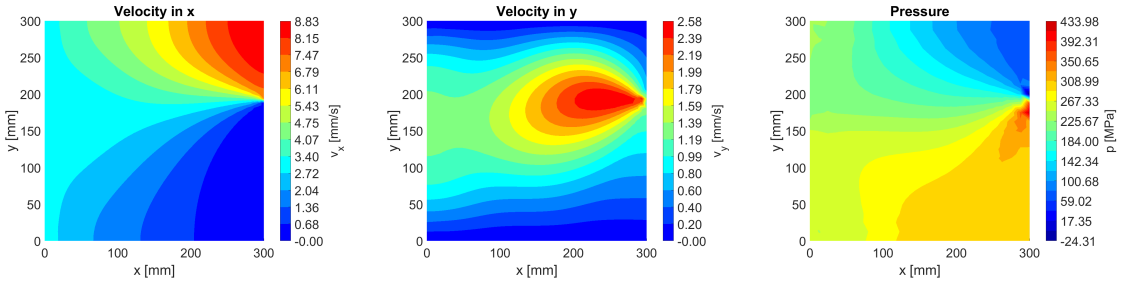
(a) Velocity in x. (b) Velocity in y. (c) Pressure.

Figure 4.61: Results obtained with the mixed dual method and $n_{dom} = 13$.



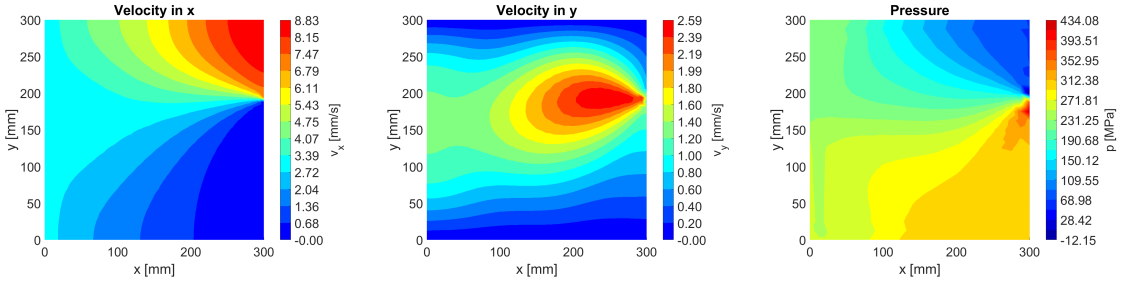
(a) Velocity in x. (b) Velocity in y. (c) Pressure.

Figure 4.62: Results obtained with the mixed dual method and $n_{dom} = 14$.



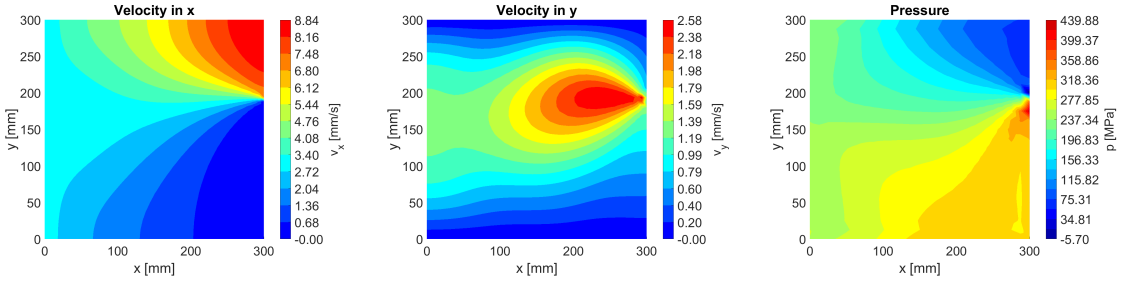
(a) Velocity in x. (b) Velocity in y. (c) Pressure.

Figure 4.63: Results obtained with the mixed dual method and $n_{dom} = 15$.



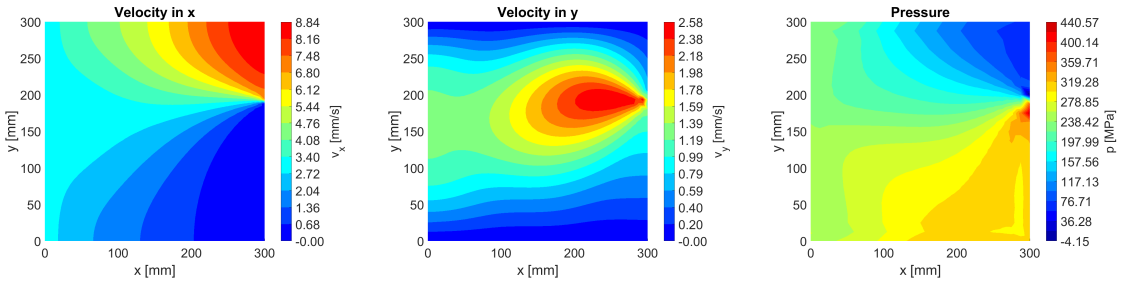
(a) Velocity in x. (b) Velocity in y. (c) Pressure.

Figure 4.64: Results obtained with the mixed dual method and $n_{dom} = 16$.



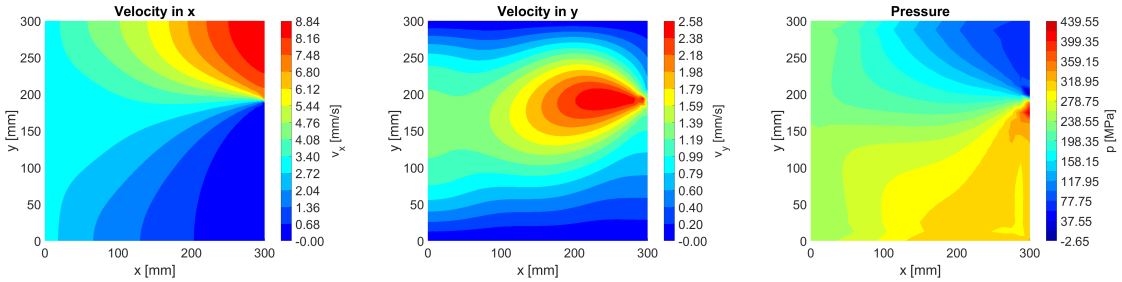
(a) Velocity in x. (b) Velocity in y. (c) Pressure.

Figure 4.65: Results obtained with the mixed dual method and $n_{dom} = 17$.



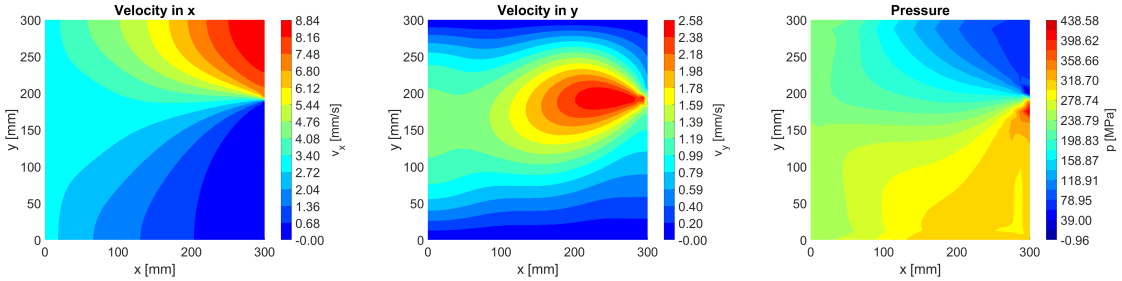
(a) Velocity in x. (b) Velocity in y. (c) Pressure.

Figure 4.66: Results obtained with the mixed dual method and $n_{dom} = 18$.



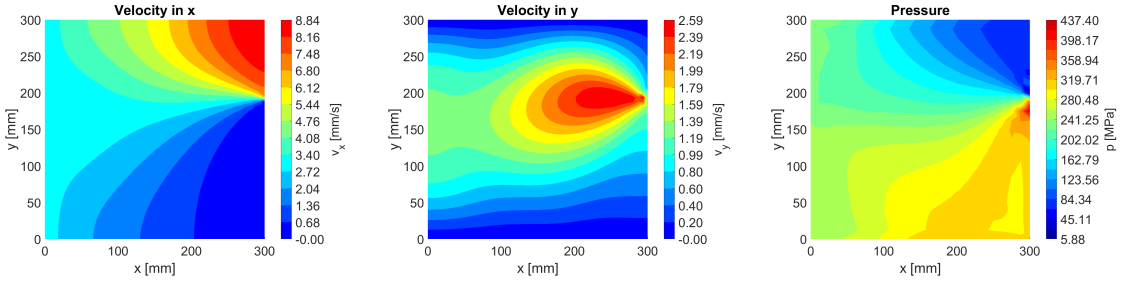
(a) Velocity in x. (b) Velocity in y. (c) Pressure.

Figure 4.67: Results obtained with the mixed dual method and $n_{dom} = 19$.



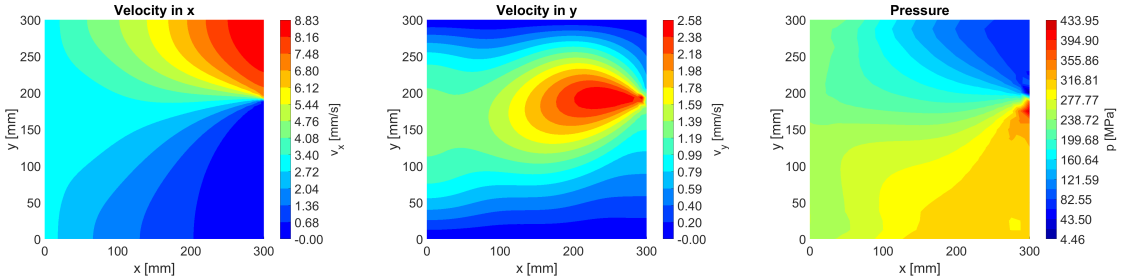
(a) Velocity in x. (b) Velocity in y. (c) Pressure.

Figure 4.68: Results obtained with the mixed dual method and $n_{dom} = 20$.



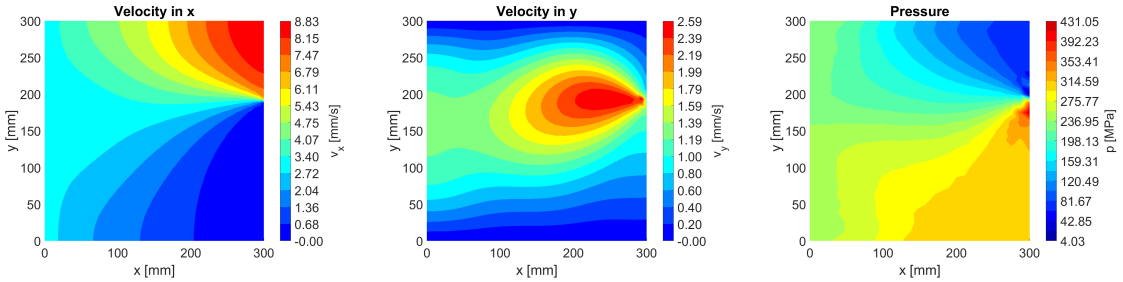
(a) Velocity in x. (b) Velocity in y. (c) Pressure.

Figure 4.69: Results obtained with the mixed dual method and $n_{dom} = 21$.



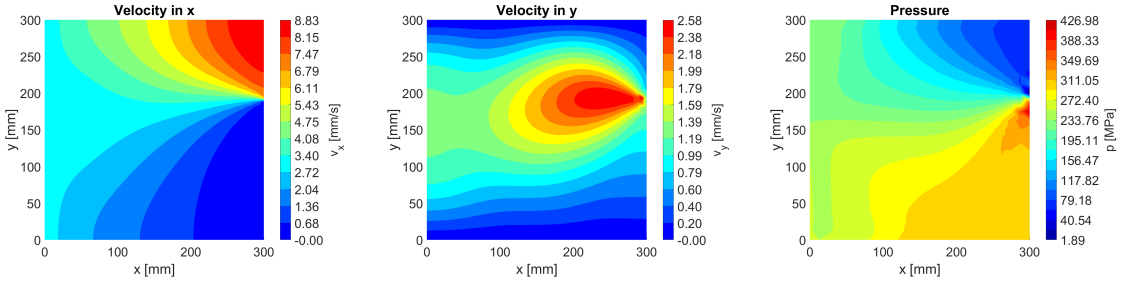
(a) Velocity in x. (b) Velocity in y. (c) Pressure.

Figure 4.70: Results obtained with the mixed dual method and $n_{dom} = 22$.



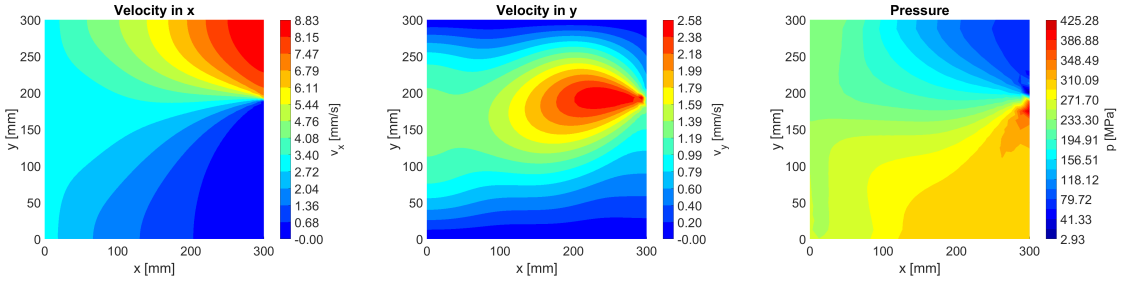
(a) Velocity in x. (b) Velocity in y. (c) Pressure.

Figure 4.71: Results obtained with the mixed dual method and $n_{dom} = 23$.



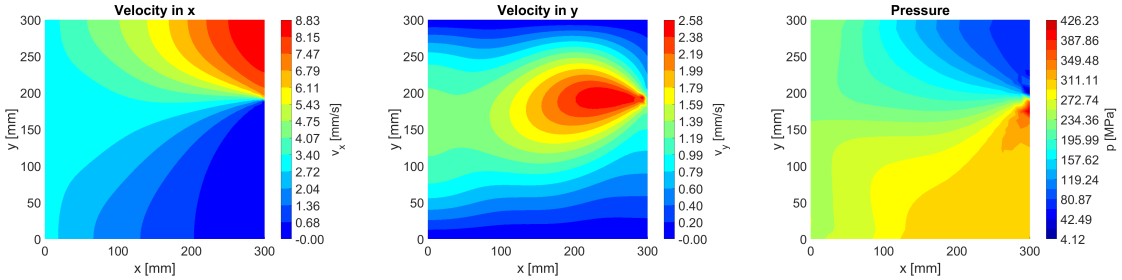
(a) Velocity in x. (b) Velocity in y. (c) Pressure.

Figure 4.72: Results obtained with the mixed dual method and $n_{dom} = 24$.



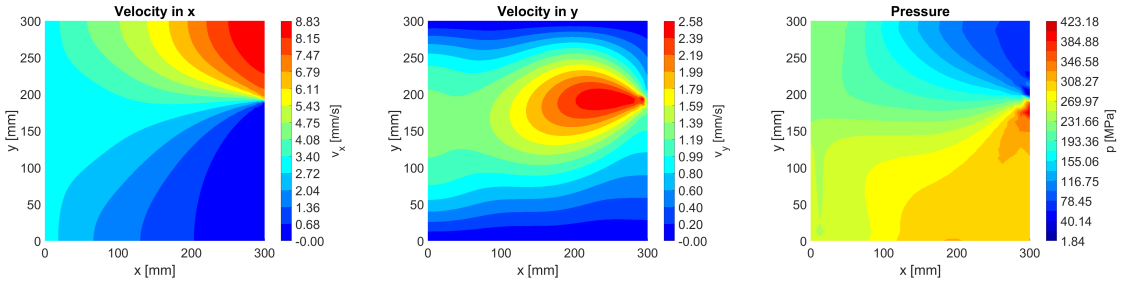
(a) Velocity in x. (b) Velocity in y. (c) Pressure.

Figure 4.73: Results obtained with the mixed dual method and $n_{dom} = 25$.



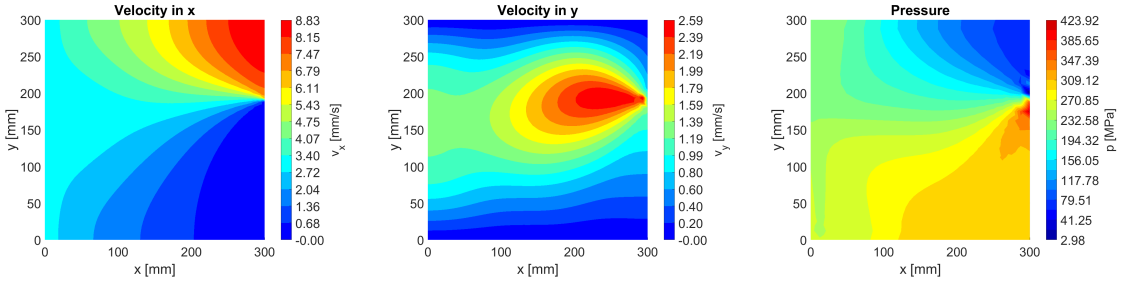
(a) Velocity in x. (b) Velocity in y. (c) Pressure.

Figure 4.74: Results obtained with the mixed dual method and $n_{dom} = 26$.



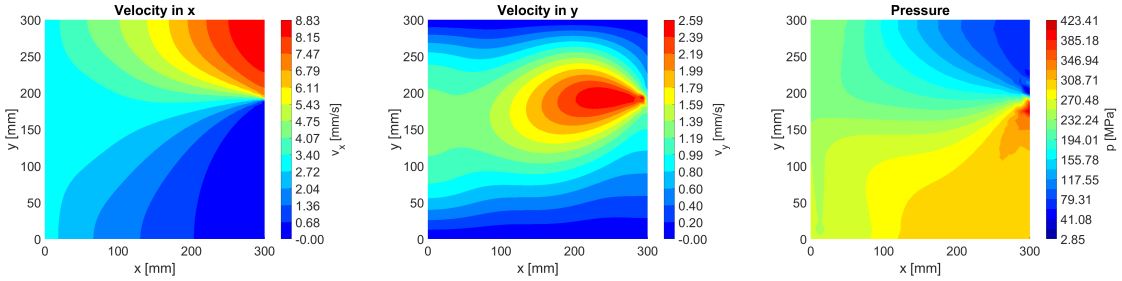
(a) Velocity in x. (b) Velocity in y. (c) Pressure.

Figure 4.75: Results obtained with the mixed dual method and $n_{dom} = 27$.



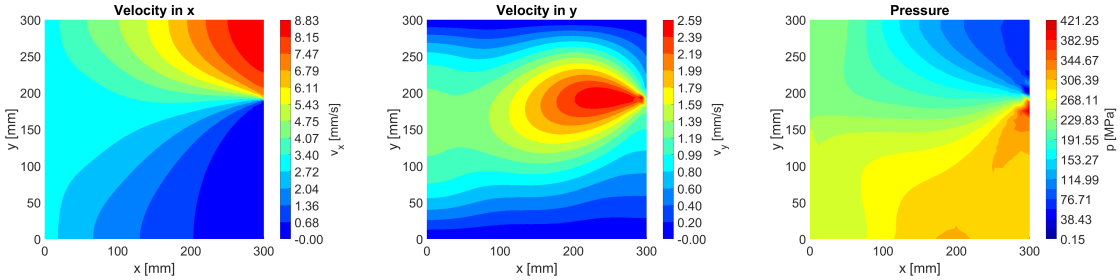
(a) Velocity in x. (b) Velocity in y. (c) Pressure.

Figure 4.76: Results obtained with the mixed dual method and $n_{dom} = 28$.



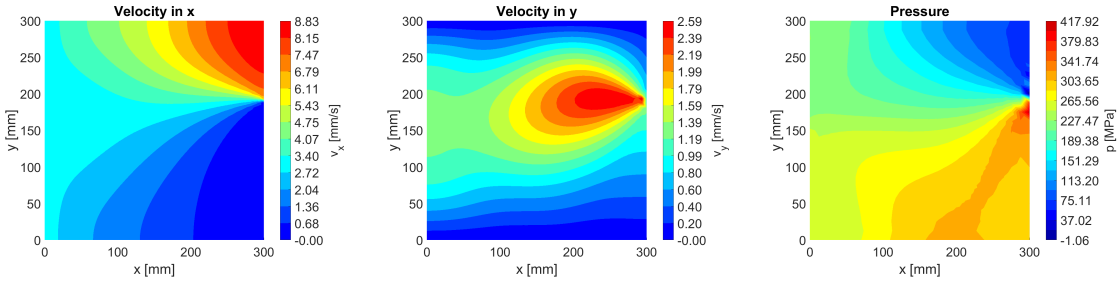
(a) Velocity in x. (b) Velocity in y. (c) Pressure.

Figure 4.77: Results obtained with the mixed dual method and $n_{dom} = 29$.



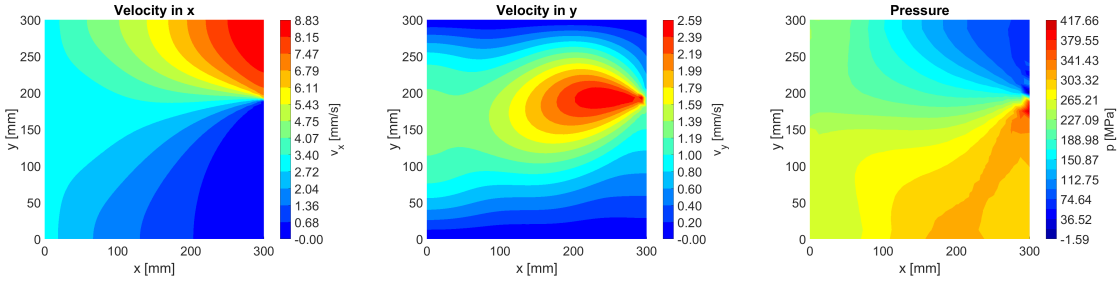
(a) Velocity in x. (b) Velocity in y. (c) Pressure.

Figure 4.78: Results obtained with the mixed dual method and $n_{dom} = 30$.



(a) Velocity in x. (b) Velocity in y. (c) Pressure.

Figure 4.79: Results obtained with the mixed dual method and $n_{dom} = 31$.



(a) Velocity in x. (b) Velocity in y. (c) Pressure.

Figure 4.80: Results obtained with the mixed dual method and $n_{dom} = 32$.

Although, values under 10 nodes inside each influence-domain would be of interest, in this method in particular, it was not possible to obtain solution due to the resulting low number of nodes inside the pressure influence domains. If the velocity influence domains were comprised of less than 10 nodes, then there would always exist one pressure influence domain with no nodes at all, which resulted in a singularity, ending the program abruptly.

Above 10 nodes possible solutions are obtained, but it is possible to observe that from 10 to 13 the results are incorrect. This is, once again, due to the low number of nodes inside the pressure influence domains. Although no influence domain is empty, some of them have just 1 or 2 nodes inside them, leading to low quality solutions.

Other than that, solutions looked right after the level of 14 nodes and the subsequent solutions were very similar with just slight variations as the number of nodes increased. These variations are more visible on the pressure fields.

Similarly to what was done for the order of integration, the data of these analyses was collected in same point and lines. This allows to better visualize the evolution of these solutions. Plotting the point information Figure 4.81 is obtained.

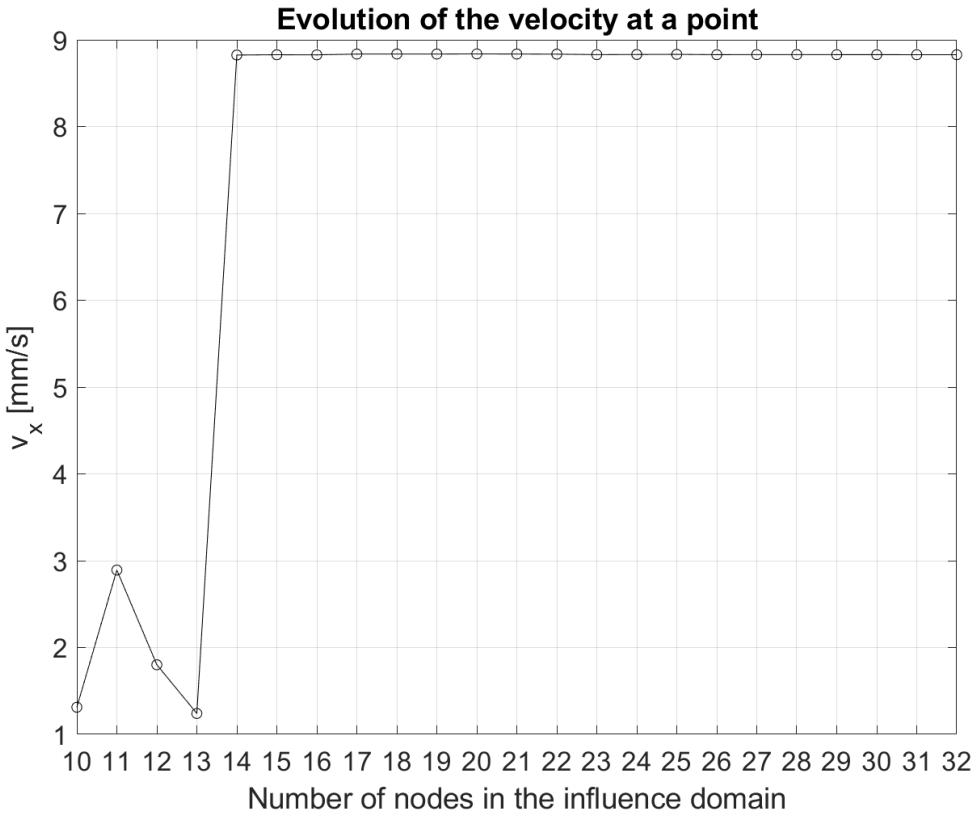


Figure 4.81: Evolution of the velocity a point with the number of nodes inside the influence domain.

In Figure 4.81 it is possible to observe that despite the variations in the first four solutions, the rest of the evolution appears to be constant. Since these four solutions were the ones showing invalid results, it was expected some kind of difference to the others. Also, observing the velocity axis, it becomes apparent that the range of values is too large and some information may be lost. Thus, plotting the same information considering only a number of nodes greater than 13, Figure 4.82 is obtained.

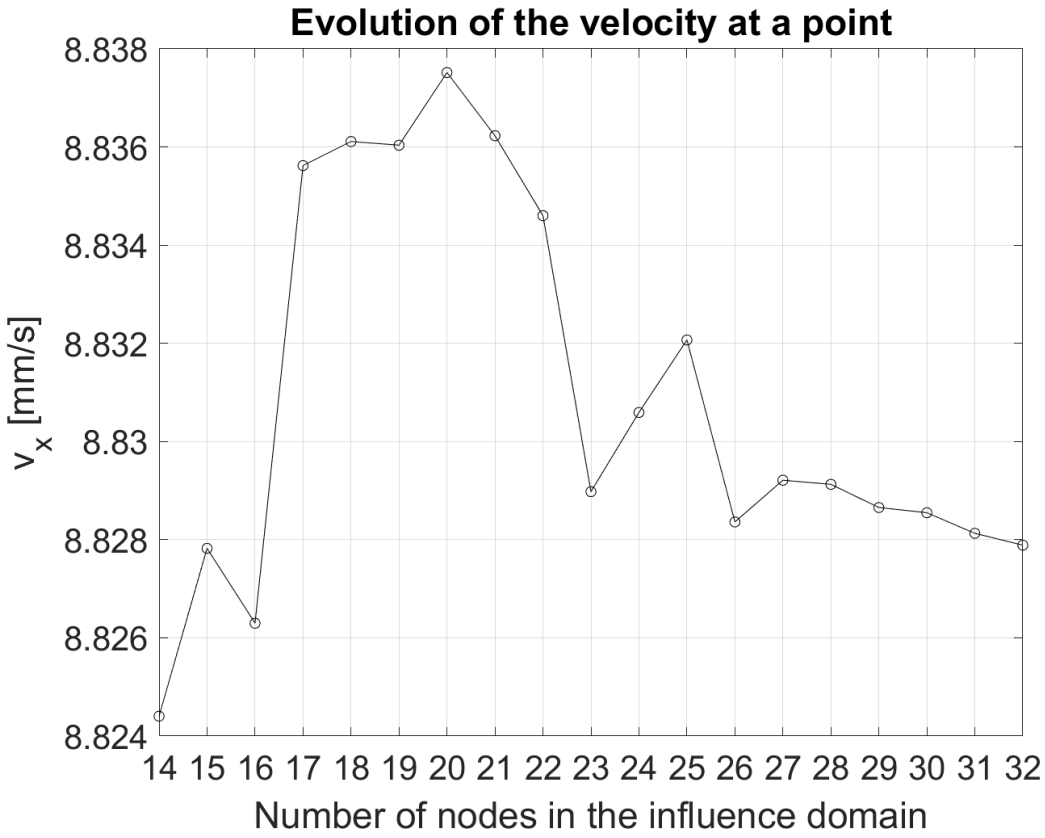


Figure 4.82: Evolution of the velocity with number of nodes considering only the valid solutions.

Figure 4.82 shows with better detail the numerical evolution of the solution with the increase in the number of nodes inside the influence domain. In this plot, it is important to identify the first stable horizontal step, because this indicates that the solution has stabilized around that dimension of influence domain. And concerning the choice of the first step, this is only motivated by the computation cost associated with the increase of the number of nodes inside each influence domain.

Figure 4.82 shows that the solutions obtained with 17, 18 and 19 nodes inside the influence-domain are very close between each other. Thus, it can be assumed that 18 nodes inside the influence domain is an efficient choice. Hence, further examples will be analysed considering 18 nodes inside each influence domain.

4.3.3 Mesh Independence

At this point, both the integration scheme and the size of the influence domains are set. The next step concerns the ability for the method to run effectively in irregular meshes. For this, eight irregular meshes, with $divL = divD = 48$, will be tested, each with a different levels of irregularity (Figures 4.83 to 4.90). Each one of the meshes was analysed 10 times and the average was used for comparison purposes. The irregularity is defined in equation (3.72) and controlled by λ which will take the following values,

$$\lambda = \{1000;\ 100;\ 10;\ 7,5;\ 5;\ 4;\ 3;\ 2\} \tag{4.3}$$

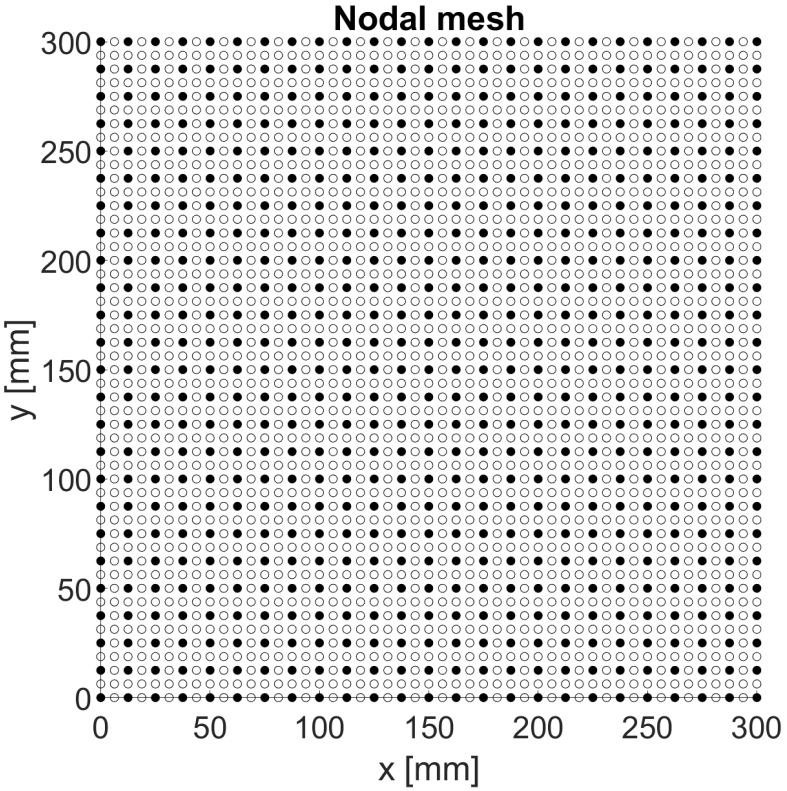


Figure 4.83: Nodal mesh analysed with $\lambda = 1000$.

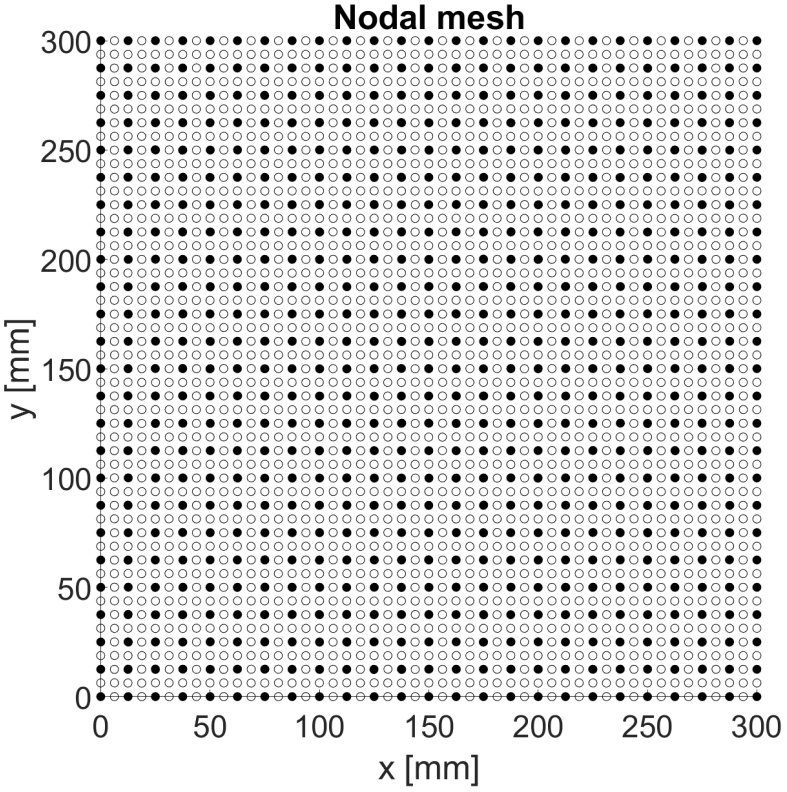


Figure 4.84: Nodal mesh analysed with $\lambda = 100$.

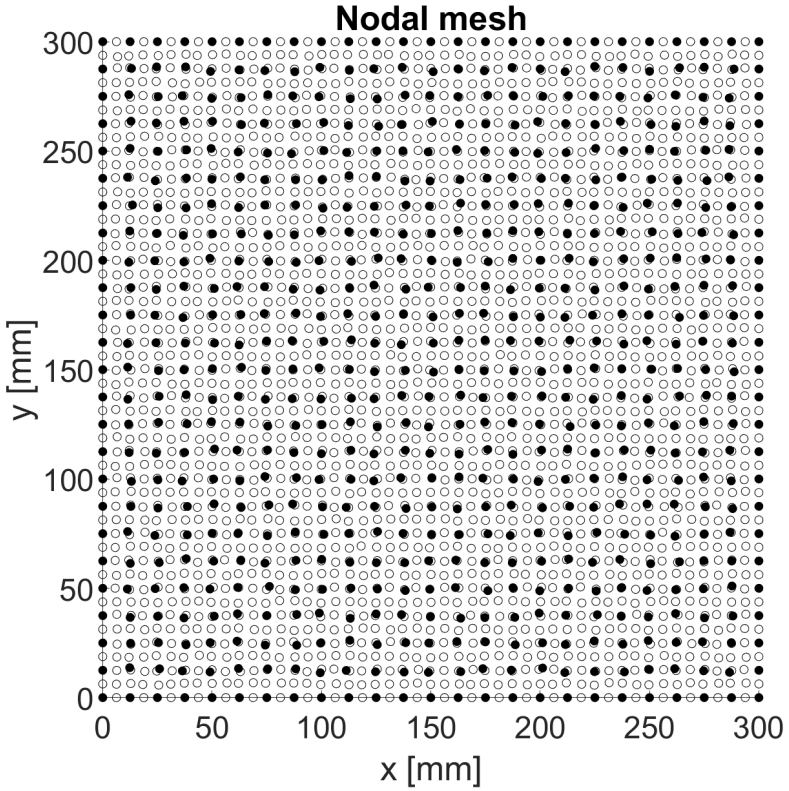


Figure 4.85: Nodal mesh analysed with $\lambda = 10$.

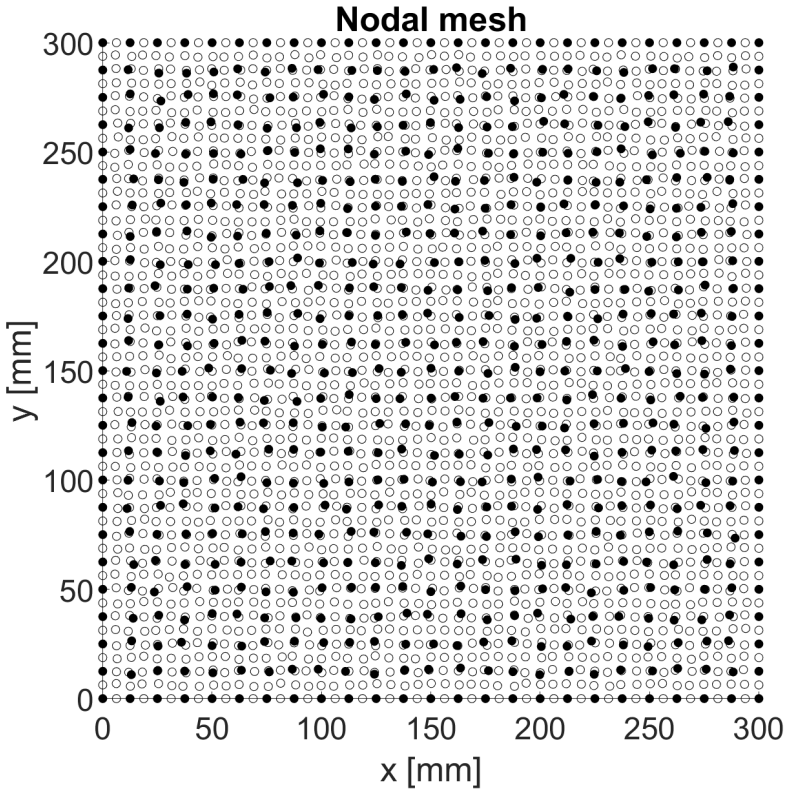


Figure 4.86: Nodal mesh analysed with $\lambda = 7,5$.

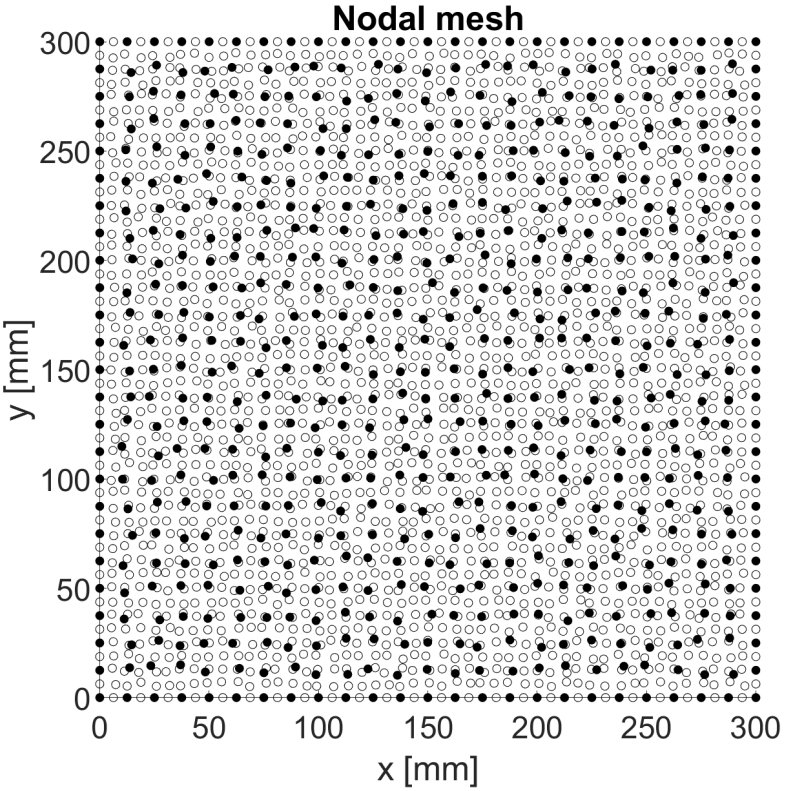


Figure 4.87: Nodal mesh analysed with $\lambda = 5$.

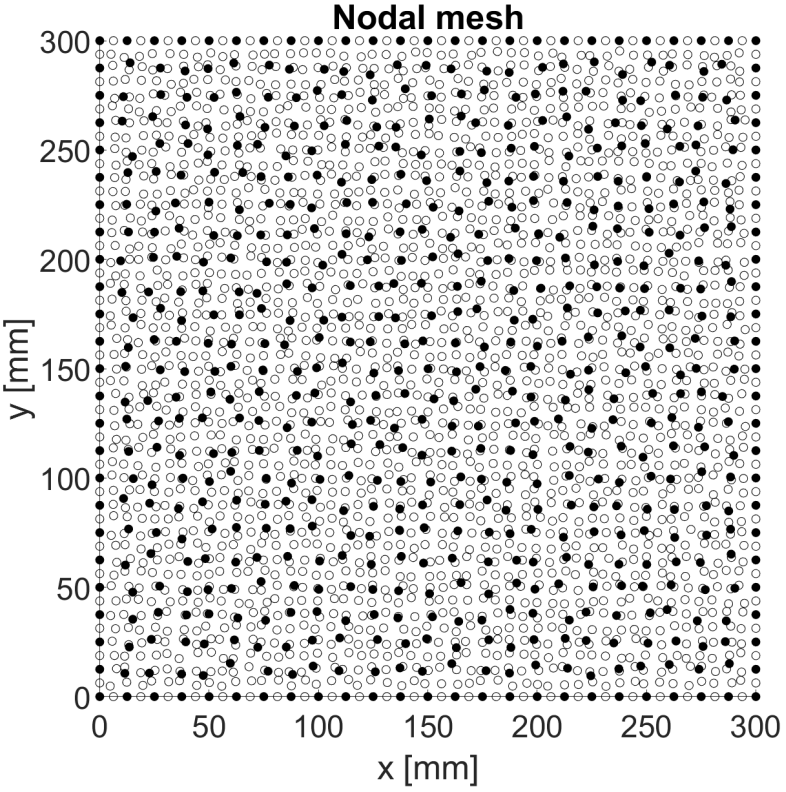


Figure 4.88: Nodal mesh analysed with $\lambda = 4$.

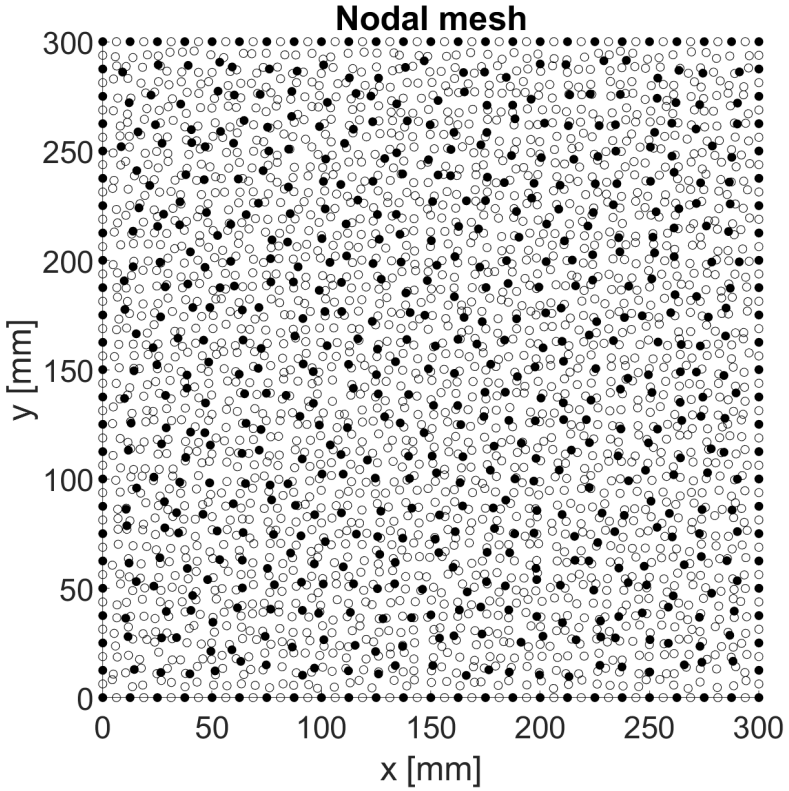


Figure 4.89: Nodal mesh analysed with $\lambda = 3$.

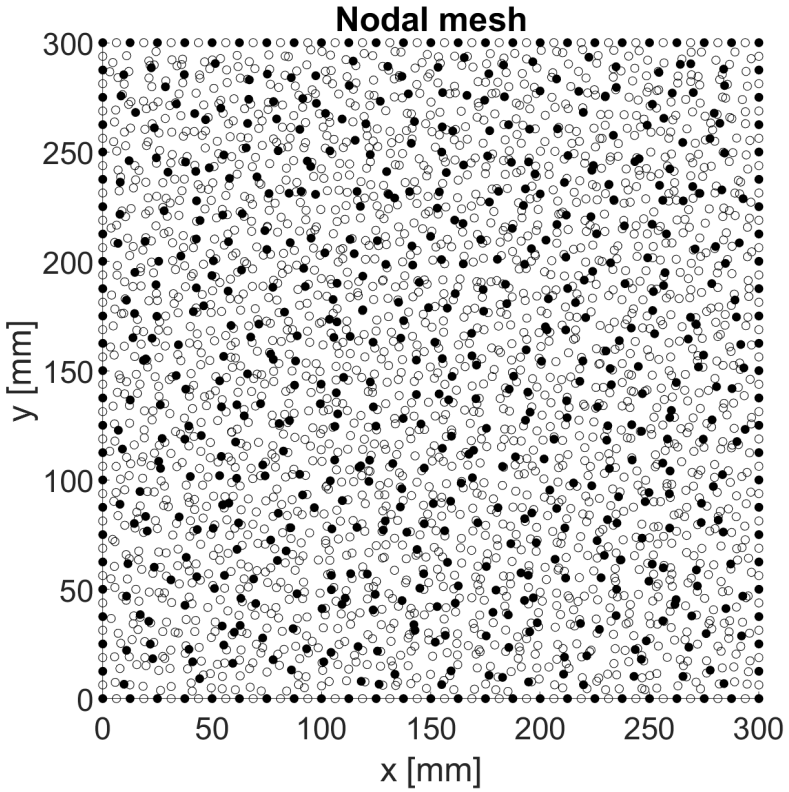
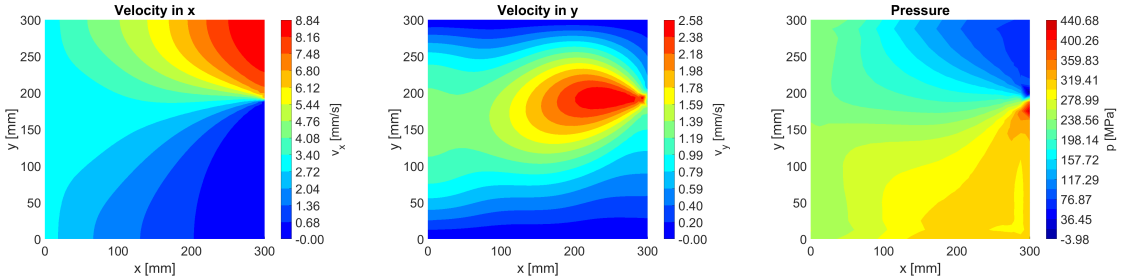
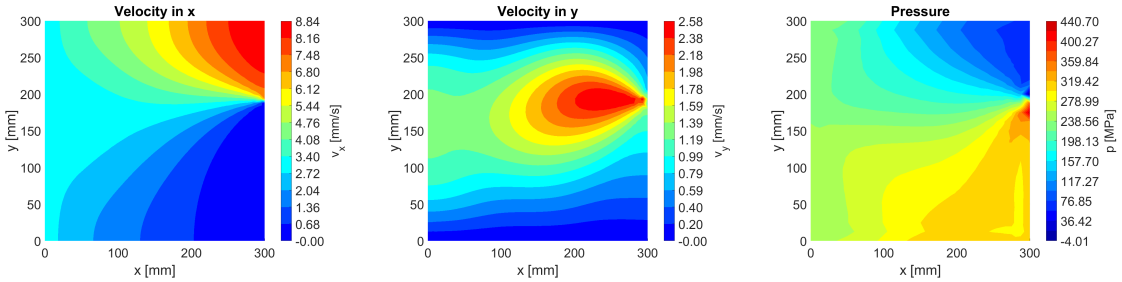


Figure 4.90: Nodal mesh analysed with $\lambda = 2$.



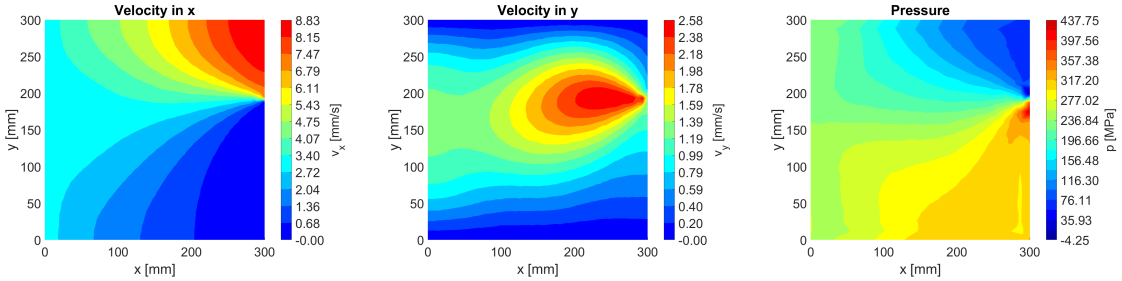
(a) Velocity in x. (b) Velocity in y. (c) Pressure.

Figure 4.91: Results obtained with the mixed dual method and $\lambda = 1000$.



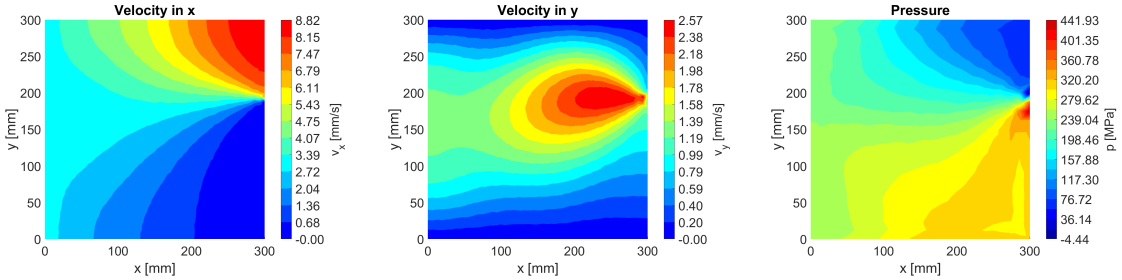
(a) Velocity in x. (b) Velocity in y. (c) Pressure.

Figure 4.92: Results obtained with the mixed dual method and $\lambda = 100$.



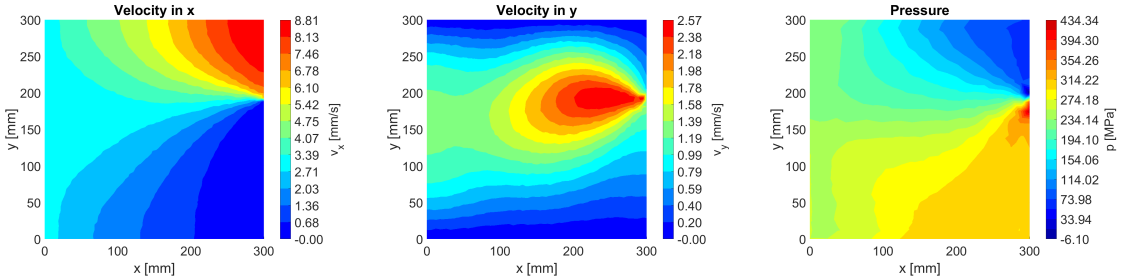
(a) Velocity in x. (b) Velocity in y. (c) Pressure.

Figure 4.93: Results obtained with the mixed dual method and $\lambda = 10$.



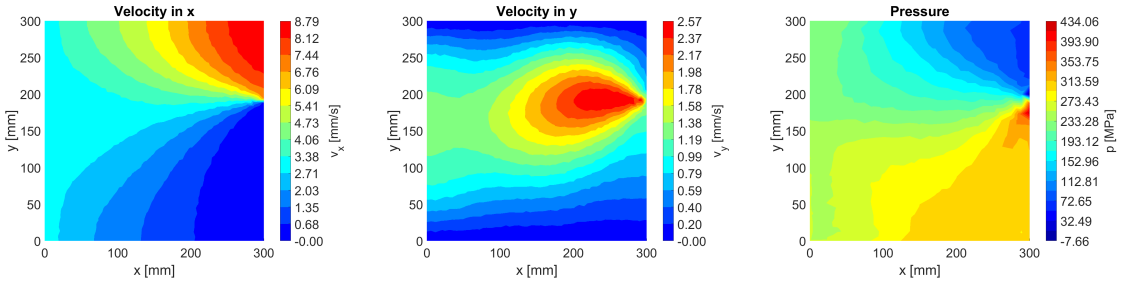
(a) Velocity in x. (b) Velocity in y. (c) Pressure.

Figure 4.94: Results obtained with the mixed dual method and $\lambda = 7,5$.



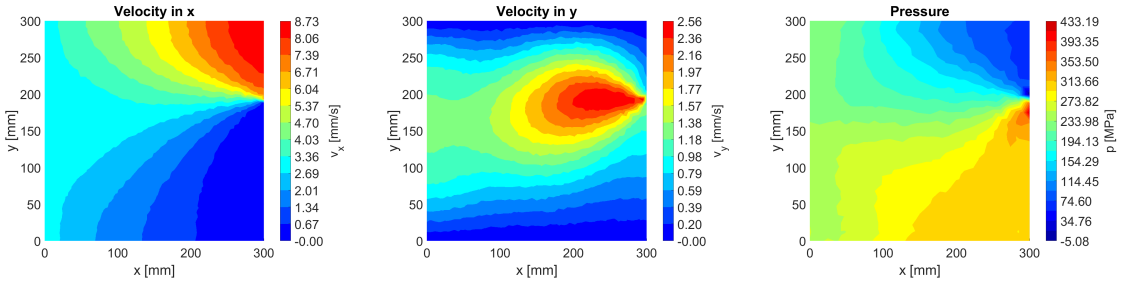
(a) Velocity in x. (b) Velocity in y. (c) Pressure.

Figure 4.95: Results obtained with the mixed dual method and $\lambda = 5$.



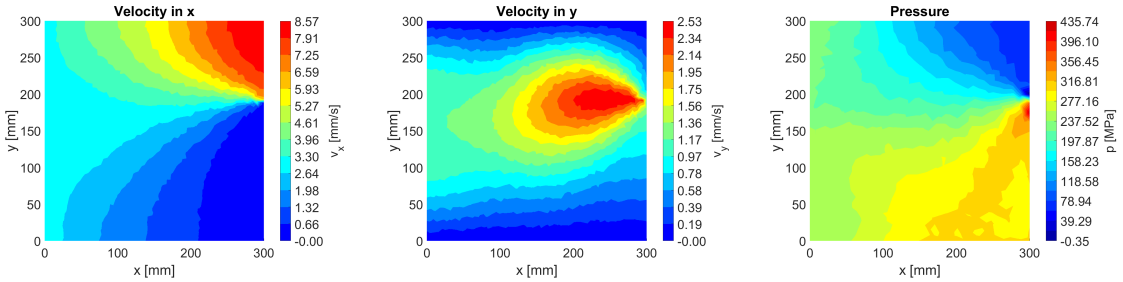
(a) Velocity in x. (b) Velocity in y. (c) Pressure.

Figure 4.96: Results obtained with the mixed dual method and $\lambda = 4$.



(a) Velocity in x. (b) Velocity in y. (c) Pressure.

Figure 4.97: Results obtained with the mixed dual method and $\lambda = 3$.



(a) Velocity in x. (b) Velocity in y. (c) Pressure.

Figure 4.98: Results obtained with the mixed dual method and $\lambda = 2$.

From the results depicted in Figures 4.91 to 4.98, it is possible to observe that all solutions have similar distributions with the exception of some slight numerical

variations and the appearance of visible fluctuations as the irregularity increases, i.e., the randomizer parameter decreases.

Visually, it is immediate that the quality of the results decreases with the increase of irregularity of the mesh. Despite this conclusion, it is important to measure the error that this irregularity introduces in the analysis. Therfore, the evolution of the velocity is plotted as a functions of the randomizer parameter in Figure 4.99.

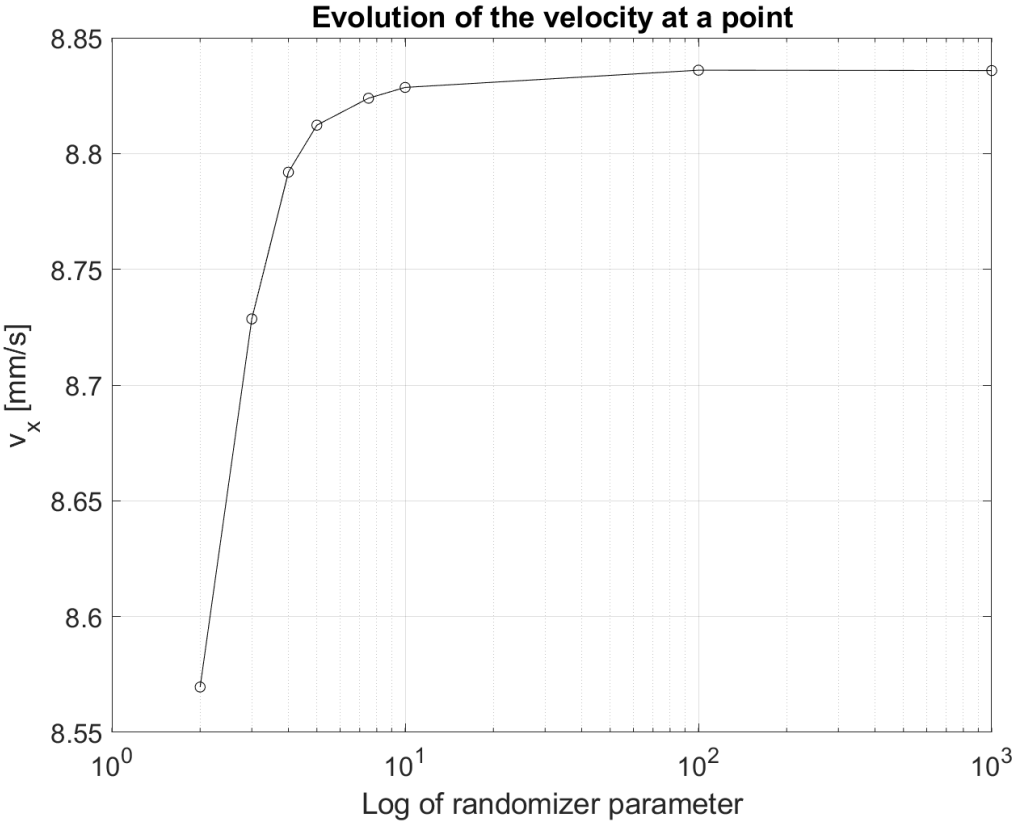


Figure 4.99: Evolution of the solution as the mesh becomes more regular.

In Figure 4.99 the randomizer parameter is represented in a logarithmic scale to aid in the visualization. It is possible to observe that as the regularity increases (the randomizer parameter increases), the solution becomes closer to a constant value. It is important to recognize how close this constant value is from the regular mesh's solution and how every degree of irregularity compares to it. For that, the relative difference was calculated with the reference value being the solution of the regular mesh, $v_x = 8,83611\, mm/s$. Thus, Figure 4.100 represents such difference with respect to the randomizer parameter.

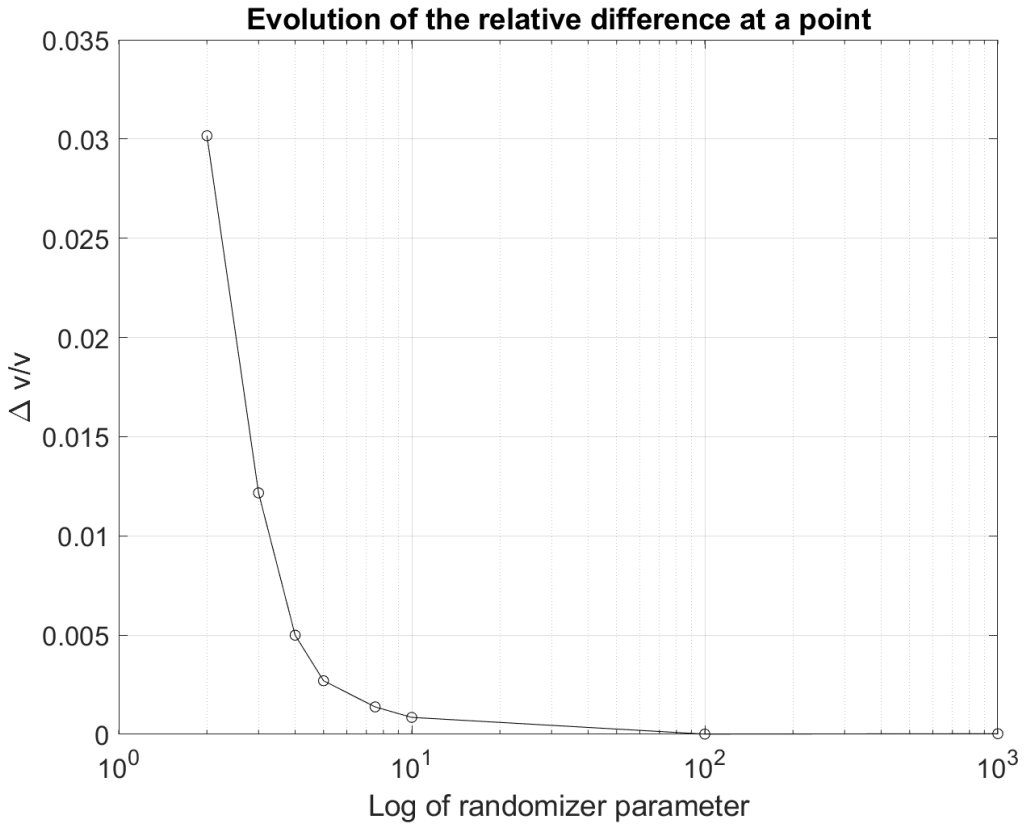


Figure 4.100: Error associated with every degree of irregularity.

In Figure 4.100 it is possible to visualize that, as expected, as the regularity increases the solution becomes closer to the solution of the regular mesh with the last two degrees of irregularity being almost at the zero line. On the other side of the spectrum, the most irregular mesh yields a solution that was within 3% of the expected solution. This low error value gives confidence that the method is capable of producing acceptable results even for highly irregular discretizations.

4.3.4 Convergence Study

Having all the other mesh parameters fixed and optimized it is time to understand how is the convergence performance of the technique. This study will allow to find if the solution is converging or not. For this, the mesh density is varied through five meshes with these number of grid divisions,

$$divL = divD = \{6;\ 12;\ 24;\ 48;\ 96\} \tag{4.4}$$

This is applied to both a regular mesh and an irregular mesh with $\lambda = 10$. The nodal meshes analysed are represented in Figures 4.101 to 4.110.

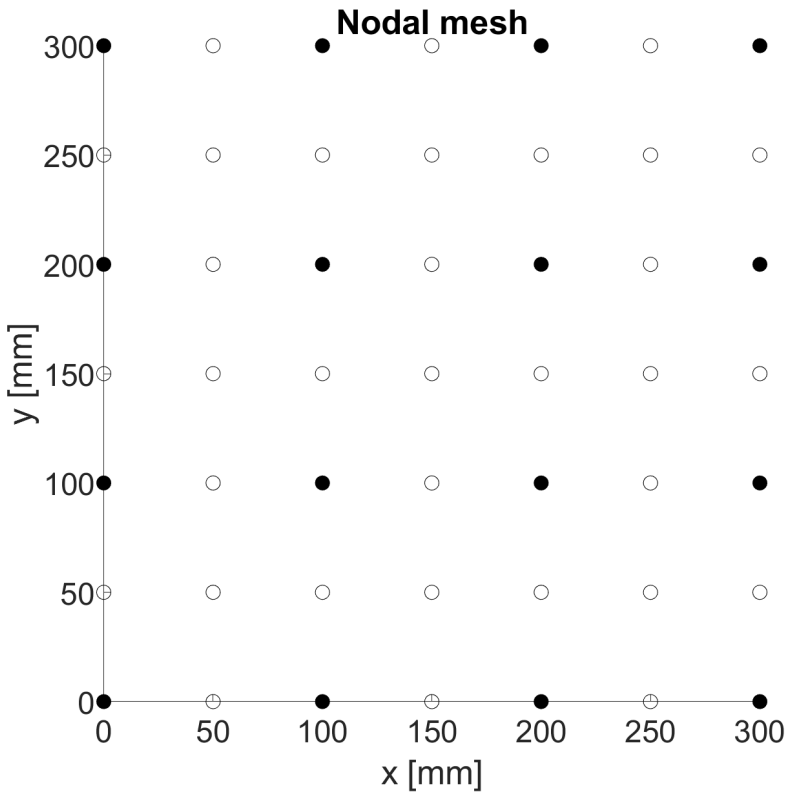


Figure 4.101: Nodal mesh analysed with $divL = divD = 6$ and $\lambda = \infty$.

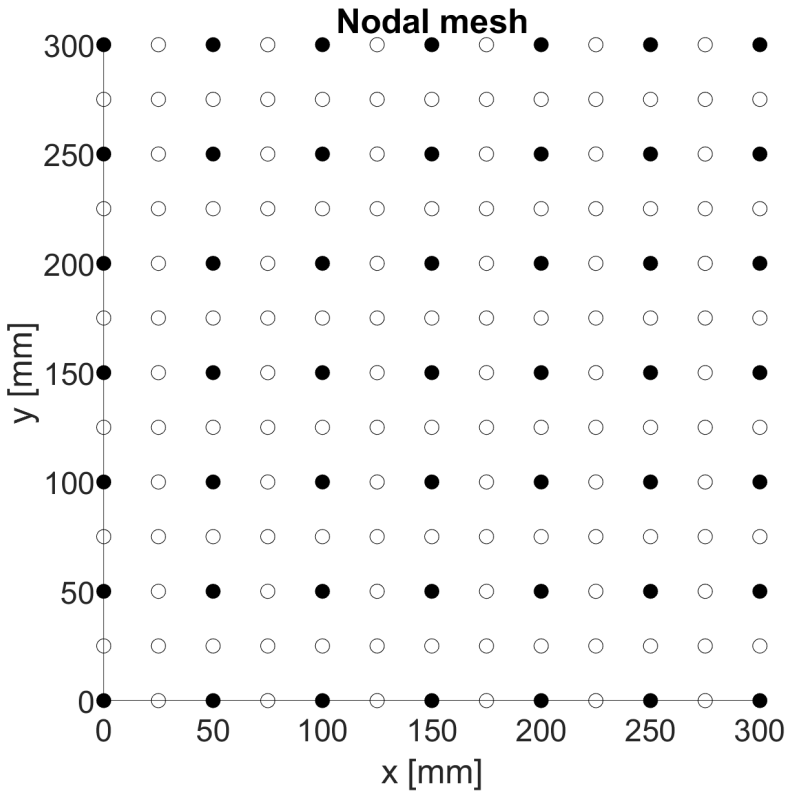


Figure 4.102: Nodal mesh analysed with $divL = divD = 12$ and $\lambda = \infty$.

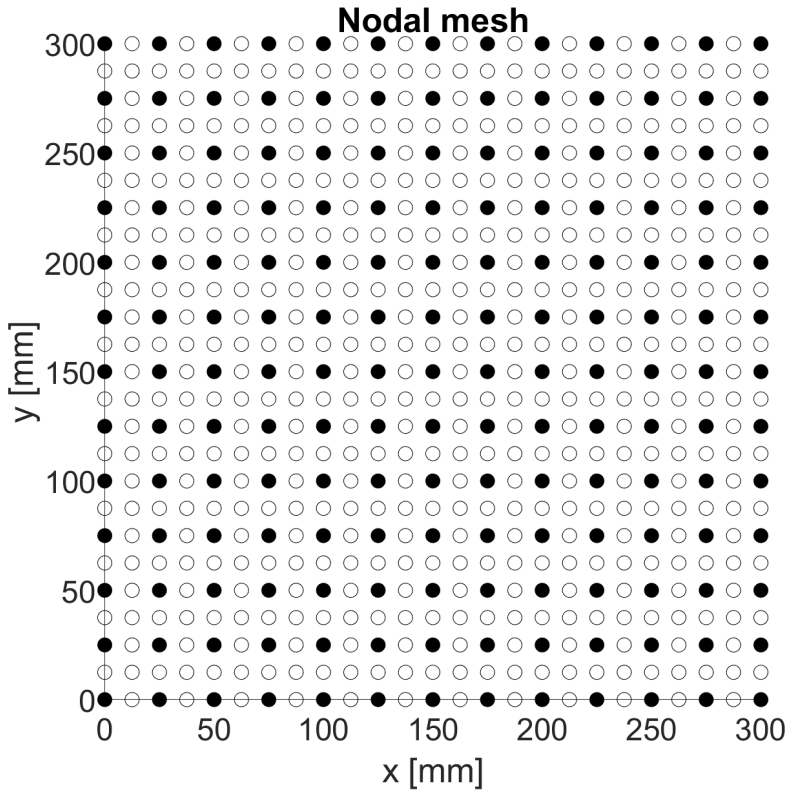


Figure 4.103: Nodal mesh analysed with $divL = divD = 12$ and $\lambda = \infty$.

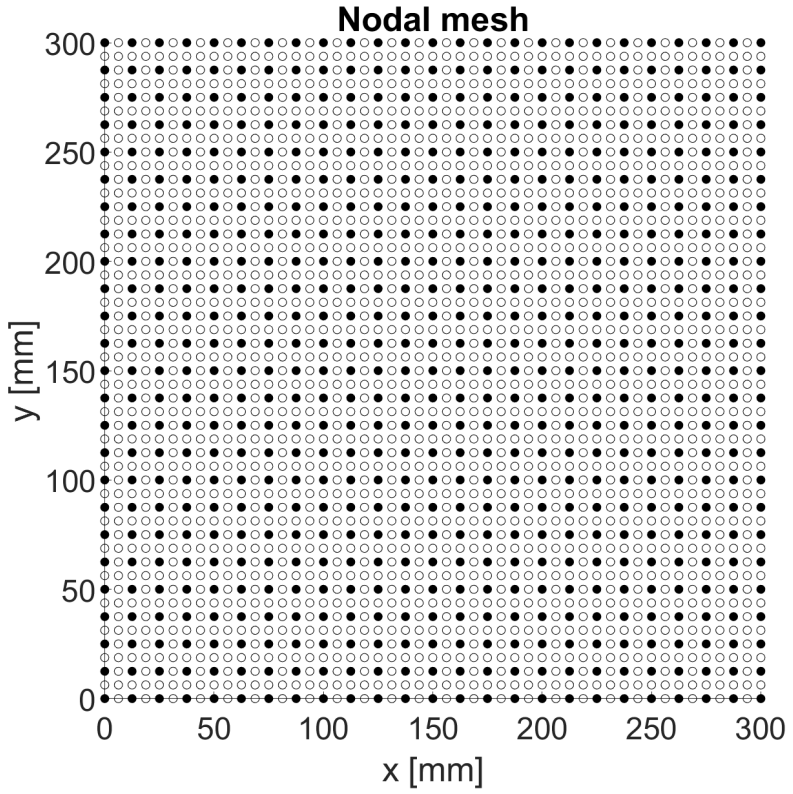


Figure 4.104: Nodal mesh analysed with $divL = divD = 12$ and $\lambda = \infty$.

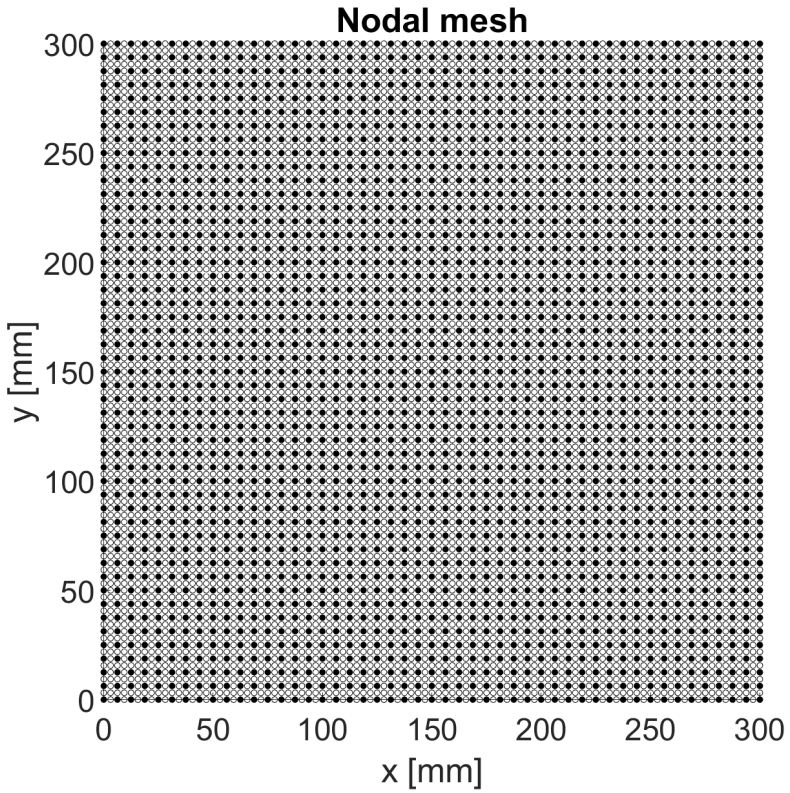


Figure 4.105: Nodal mesh analysed with $divL = divD = 12$ and $\lambda = \infty$.

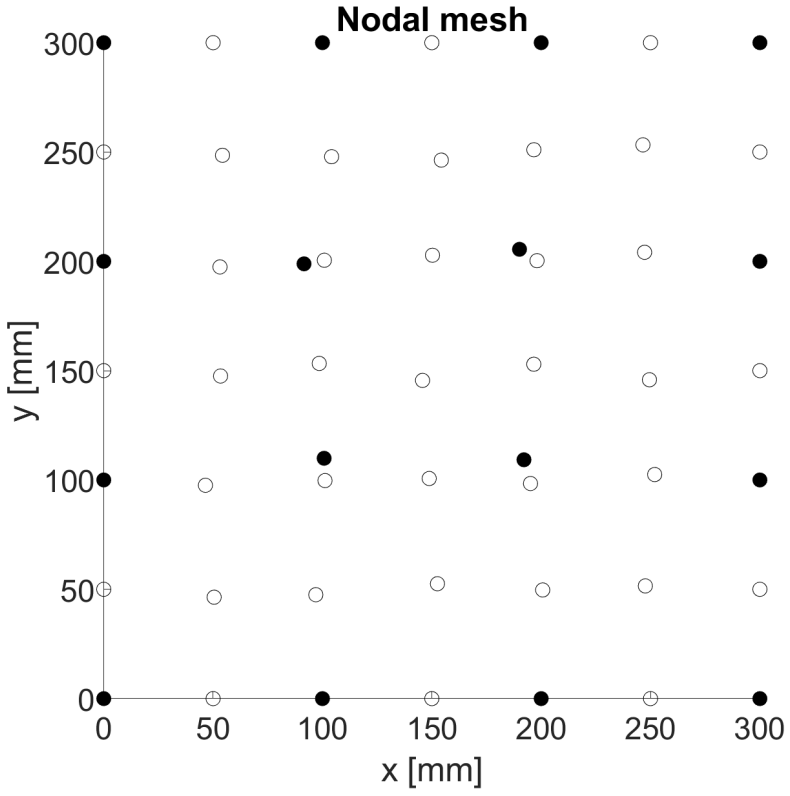


Figure 4.106: Nodal mesh analysed with $divL = divD = 6$ and $\lambda = 10$.

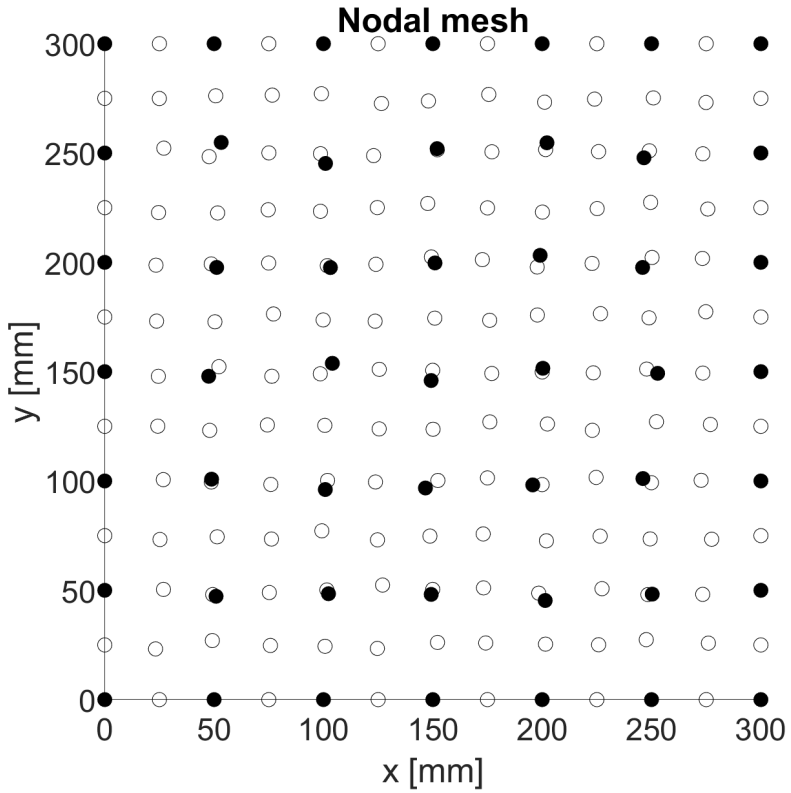


Figure 4.107: Nodal mesh analysed with $divL = divD = 12$ and $\lambda = 10$.

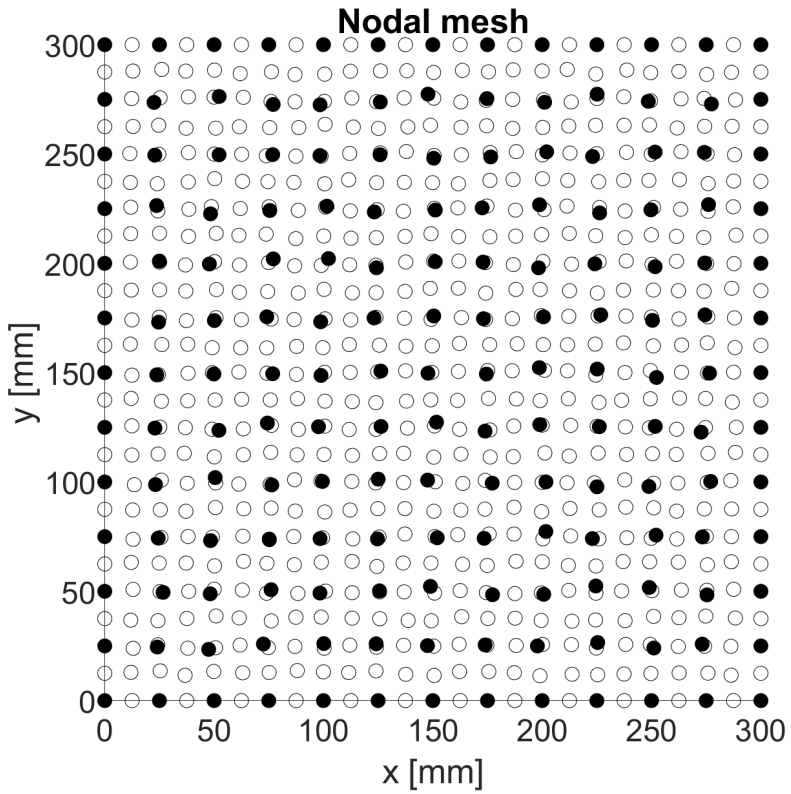


Figure 4.108: Nodal mesh analysed with $divL = divD = 12$ and $\lambda = 10$.

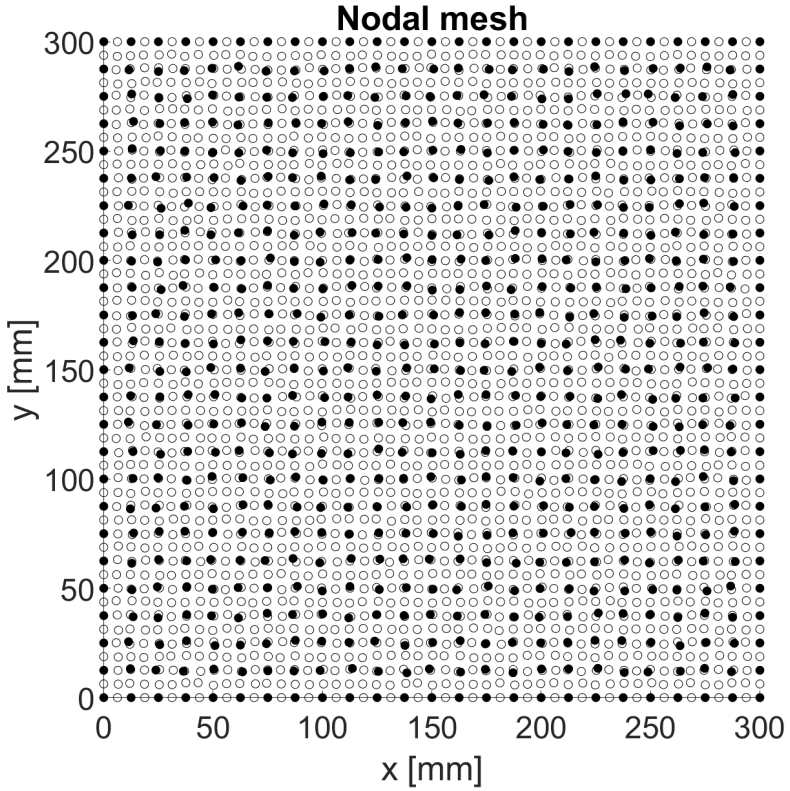


Figure 4.109: Nodal mesh analysed with $divL = divD = 12$ and $\lambda = 10$.

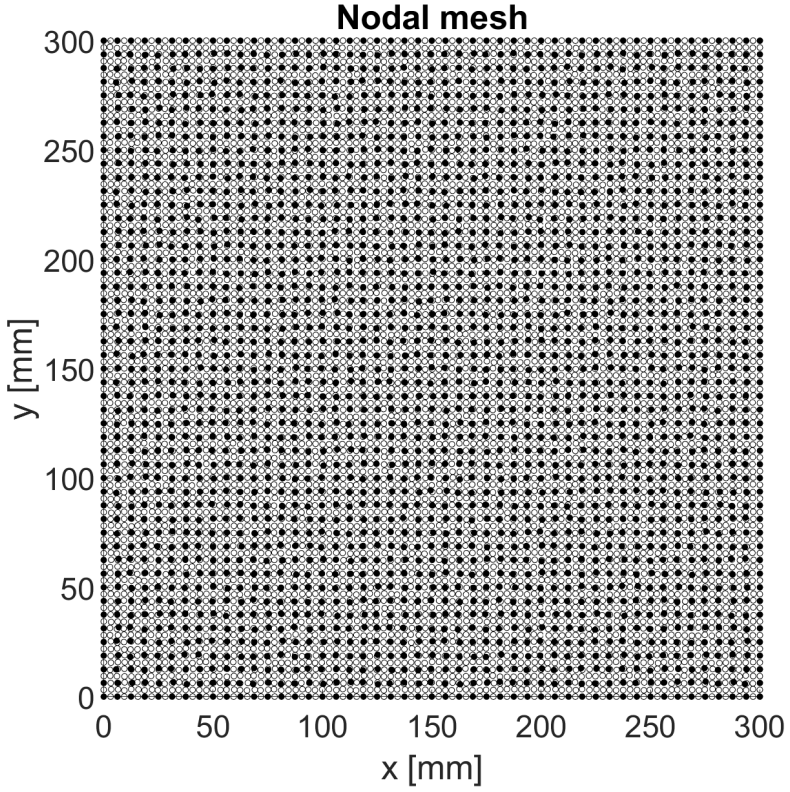
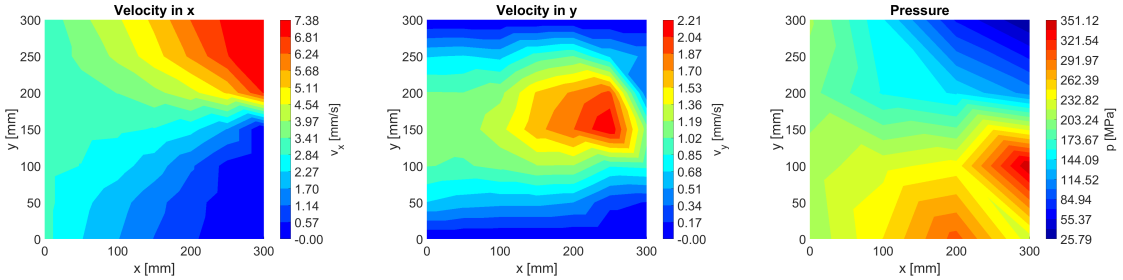
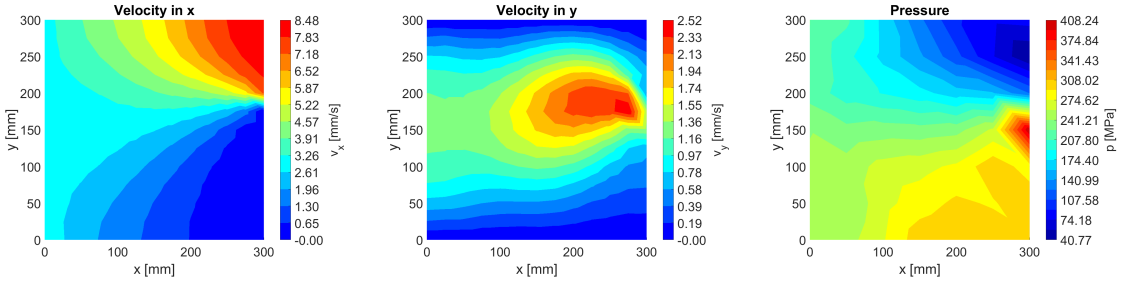


Figure 4.110: Nodal mesh analysed with $divL = divD = 12$ and $\lambda = 10$.



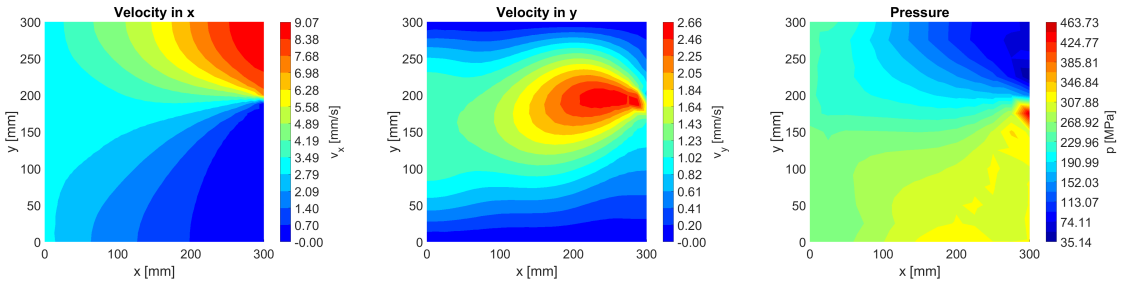
(a) Velocity in x. (b) Velocity in y. (c) Pressure.

Figure 4.111: Results obtained with the mixed dual method and a regular mesh with $divL = divD = 6$.



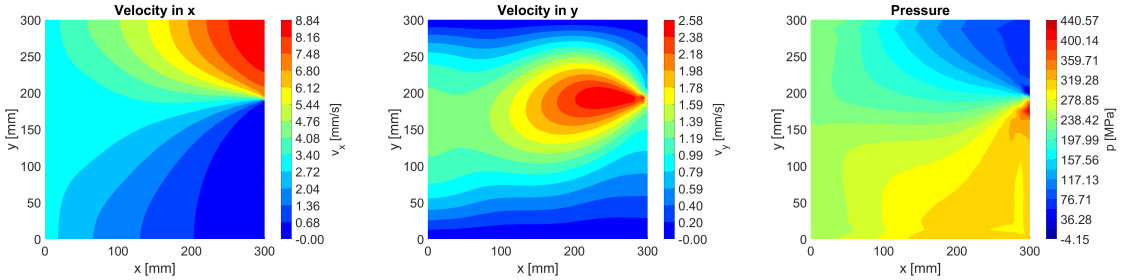
(a) Velocity in x. (b) Velocity in y. (c) Pressure.

Figure 4.112: Results obtained with the mixed dual method and a regular mesh with $divL = divD = 12$.



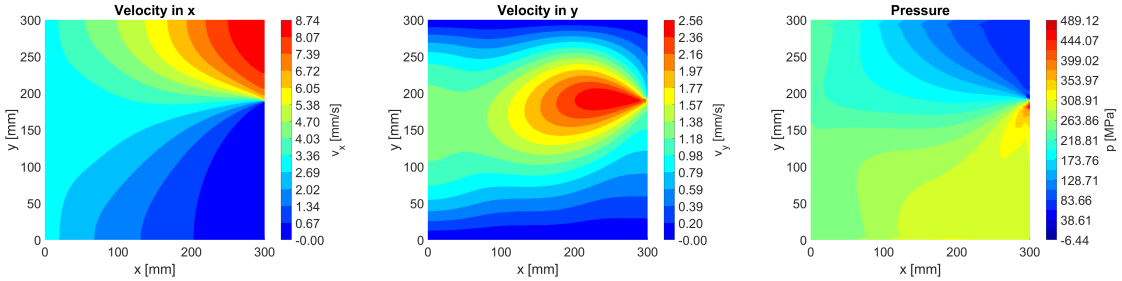
(a) Velocity in x. (b) Velocity in y. (c) Pressure.

Figure 4.113: Results obtained with the mixed dual method and a regular mesh with $divL = divD = 24$.



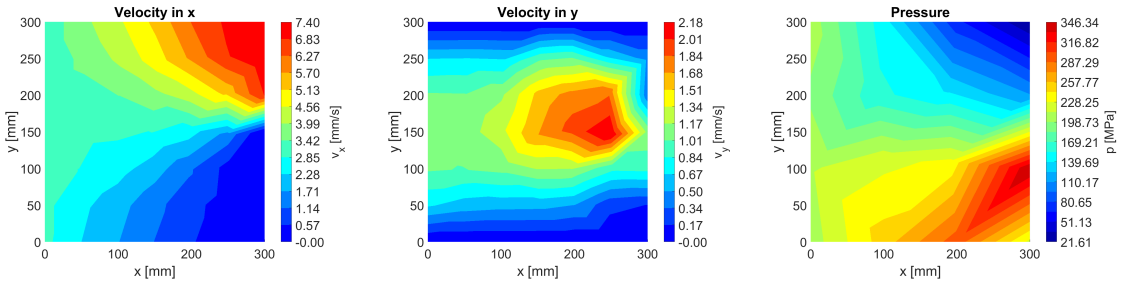
(a) Velocity in x. (b) Velocity in y. (c) Pressure.

Figure 4.114: Results obtained with the mixed dual method and a regular mesh with $divL = divD = 48$.



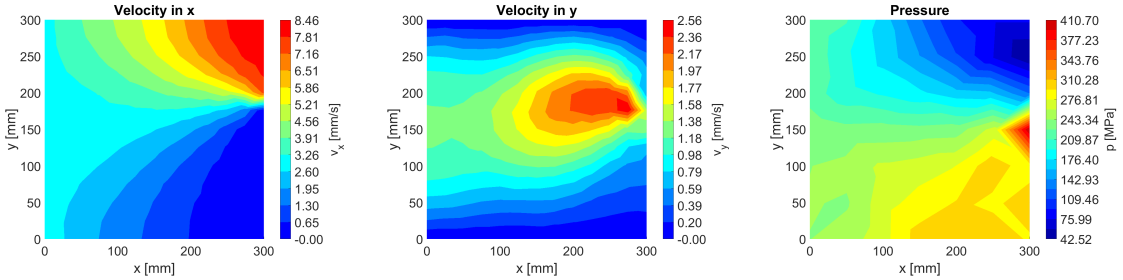
(a) Velocity in x. (b) Velocity in y. (c) Pressure.

Figure 4.115: Results obtained with the mixed dual method and a regular mesh with $divL = divD = 96$.



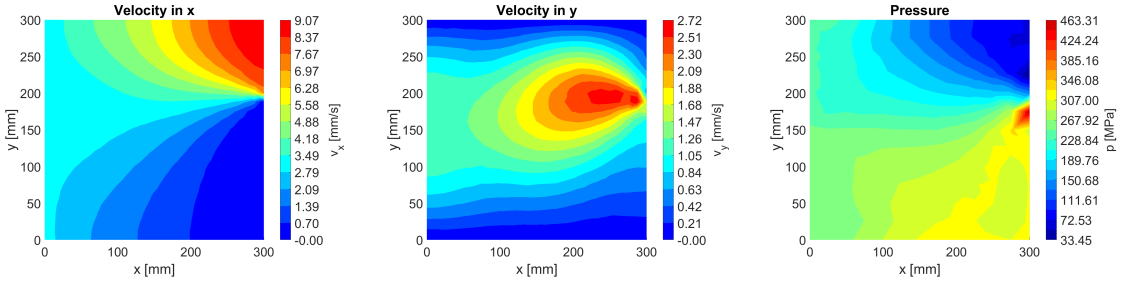
(a) Velocity in x. (b) Velocity in y. (c) Pressure.

Figure 4.116: Results obtained with the mixed dual method and an irregular mesh with $divL = divD = 6$.



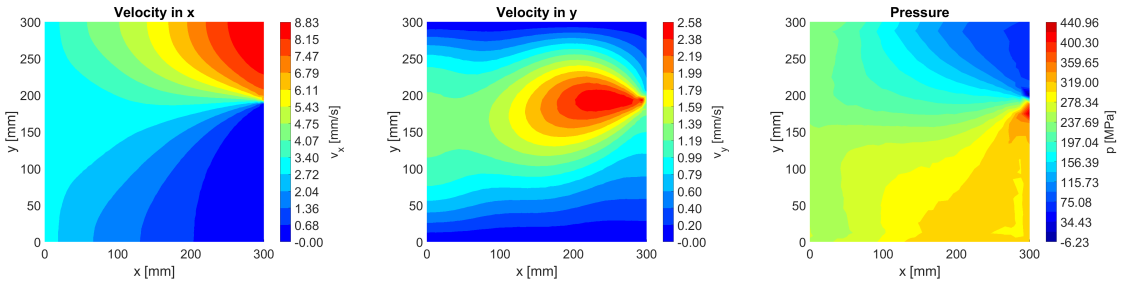
(a) Velocity in x. (b) Velocity in y. (c) Pressure.

Figure 4.117: Results obtained with the mixed dual method and an irregular mesh with $divL = divD = 12$.



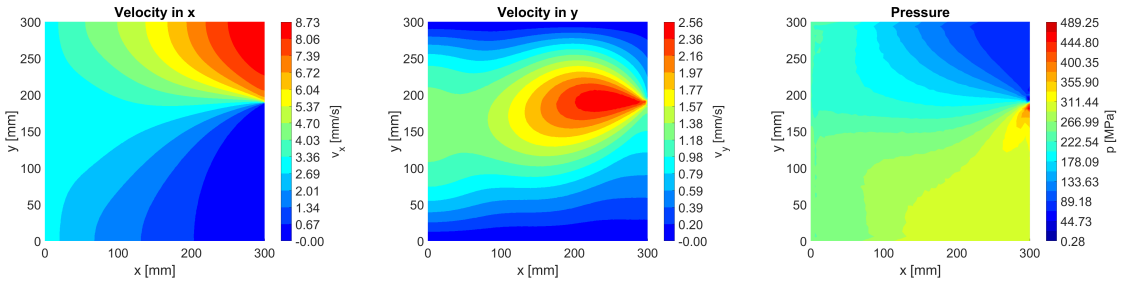
(a) Velocity in x. (b) Velocity in y. (c) Pressure.

Figure 4.118: Results obtained with the mixed dual method and an irregular mesh with $divL = divD = 24$.



(a) Velocity in x. (b) Velocity in y. (c) Pressure.

Figure 4.119: Results obtained with the mixed dual method and an irregular mesh with $divL = divD = 48$.



(a) Velocity in x. (b) Velocity in y. (c) Pressure.

Figure 4.120: Results obtained with the mixed dual method and an irregular mesh with $divL = divD = 96$.

From the set of results represented herein it is possible to visualize that both the regular meshes and irregular meshes produce similar results. This was expected, since the error that the irregular mesh introduces is very low. Also, is possible to observe the detail of the solution evolving as the mesh becomes more and more refined, with the first three densities presenting some visual cues of lack of accuracy.

In order to quantify the convergence of the mesh, the velocity in one point (with respect to the corresponding nodal discretization) must be documented.

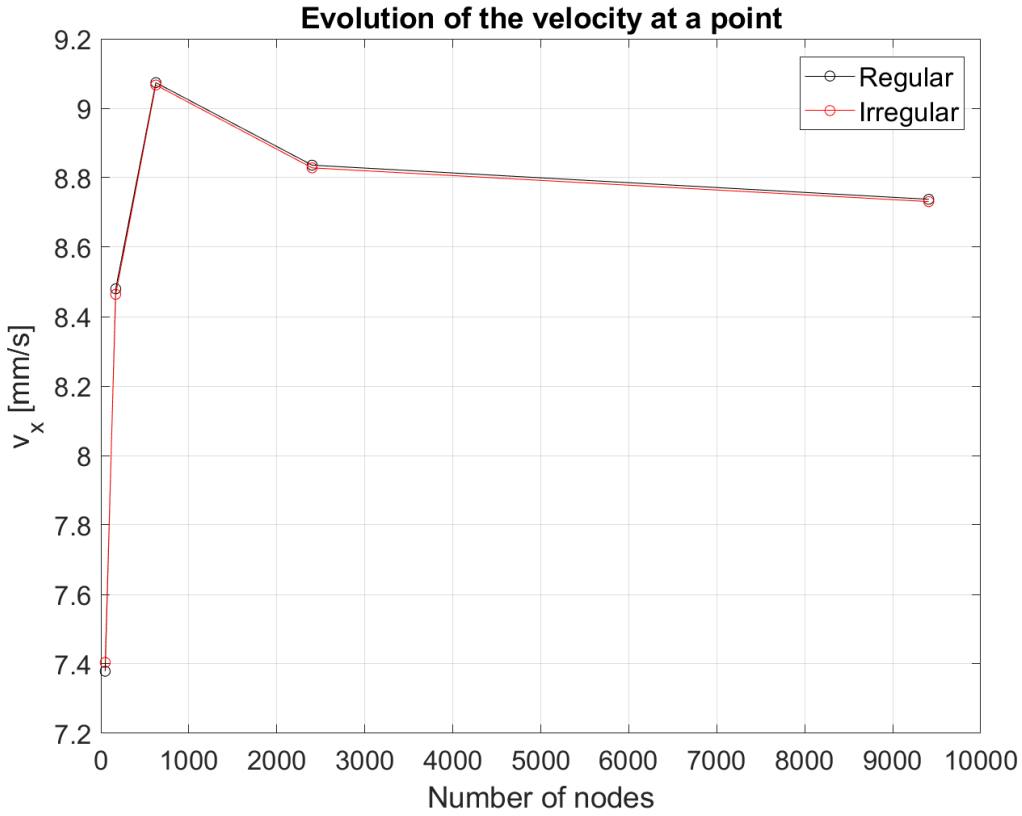


Figure 4.121: Evolution of the solution as the mesh becomes denser.

In Figure 4.121 it is possible to visualize that the solution converges as the number of nodes increase. In fact, it can be noticed that the last two nodal densities produce results very close to each other, indicating that the solution is actually converging.

In addition, a denser regular mesh was tested with 120 divisions on each side (14641 nodes). This value is used as a reference value to build an error or relative difference plot of the velocity. Thus, figure 4.122 shows the evolution of the relative velocity difference between the solutions of the distinct nodal distributions analysed.

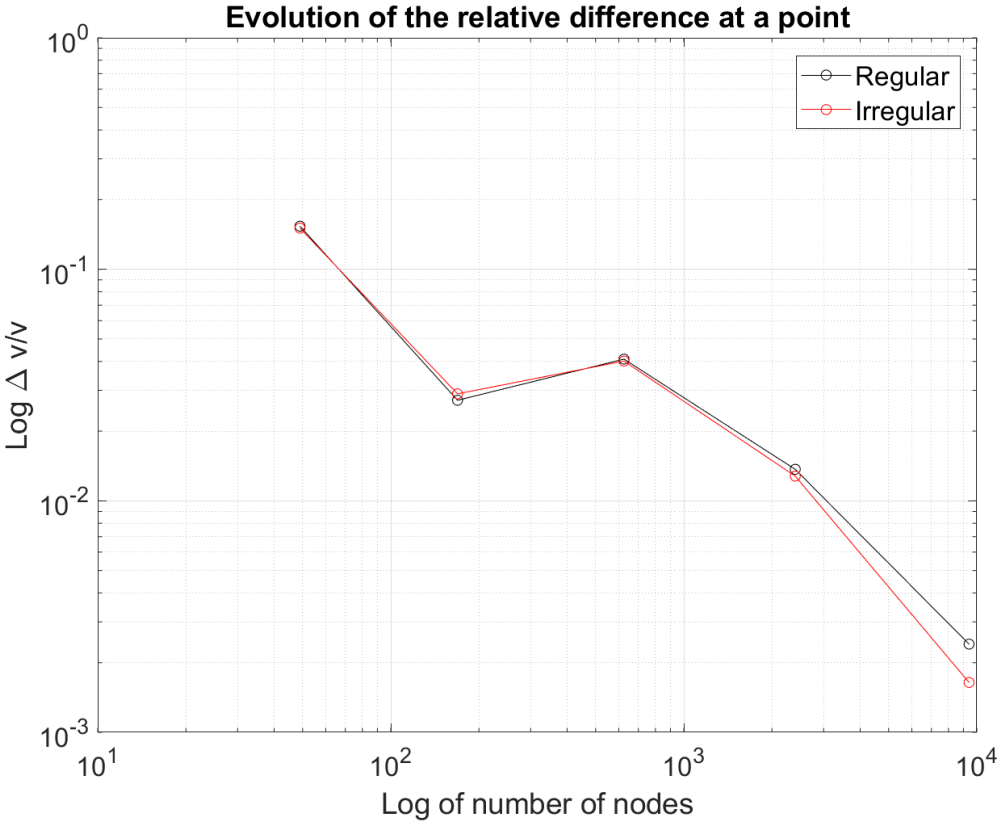
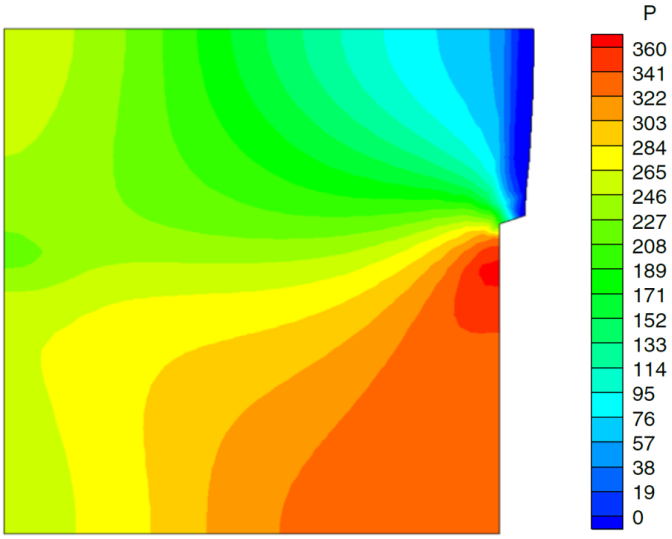


Figure 4.122: Evolution of the relative difference as the mesh becomes denser.

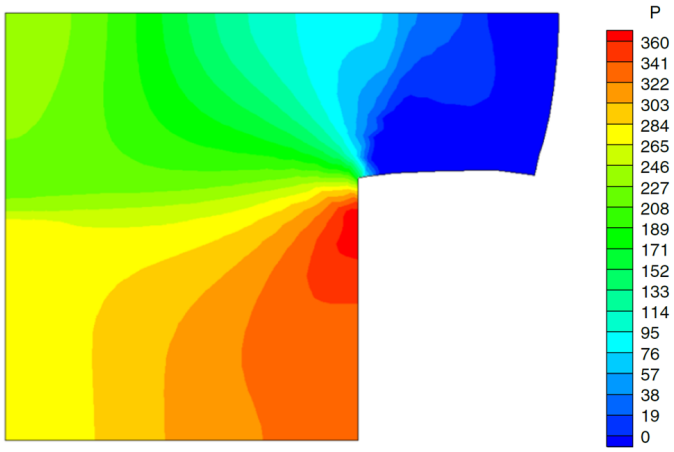
The plot in Figure 4.122 uses log-log scale in order to identify a possible asymptotic convergence. For this to be the case a straight line must be observed. In fact, looking at the last three nodal densities, the trend defined by them closely resembles a straight line, indicating an asymptotic convergence. Furthermore, this straight line has a relatively high slope which is often associated with a fast convergence.

4.3.5 Time Stepped Results

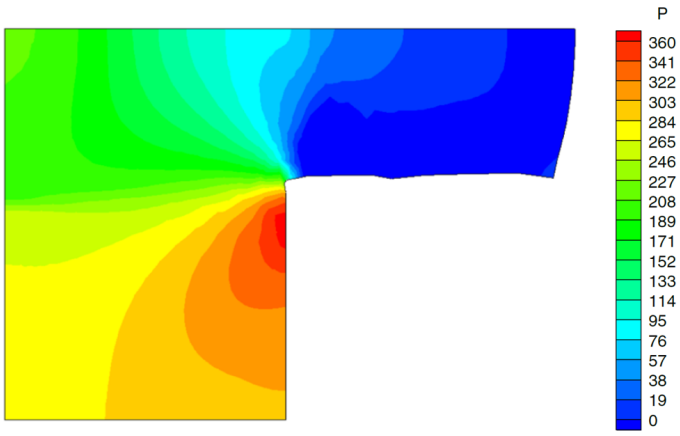
In this section, the process is simulated over time. Considering $\Delta t = 0,05\,s$ and 350 time steps the total process time simulated was a total of $17,5\,s$.



(a) Pressure at $t \approx 2,5s$.

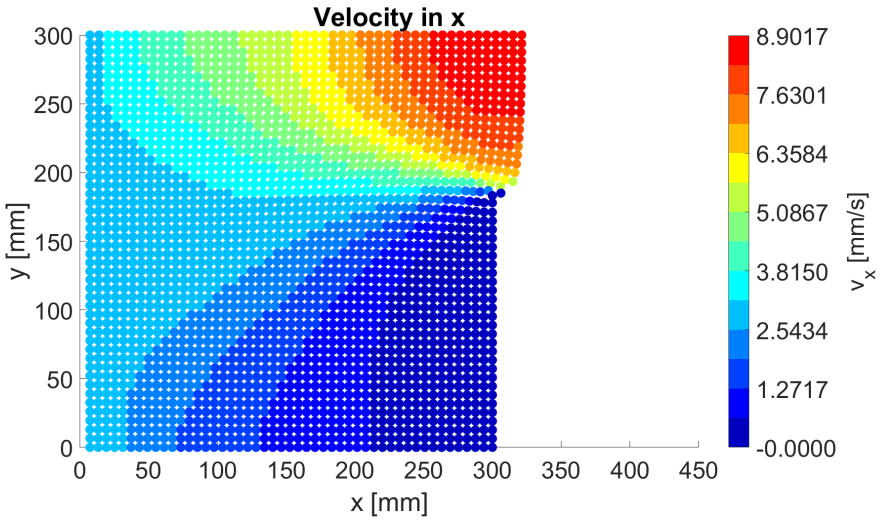


(b) Pressure at $t \approx 12,5s$.

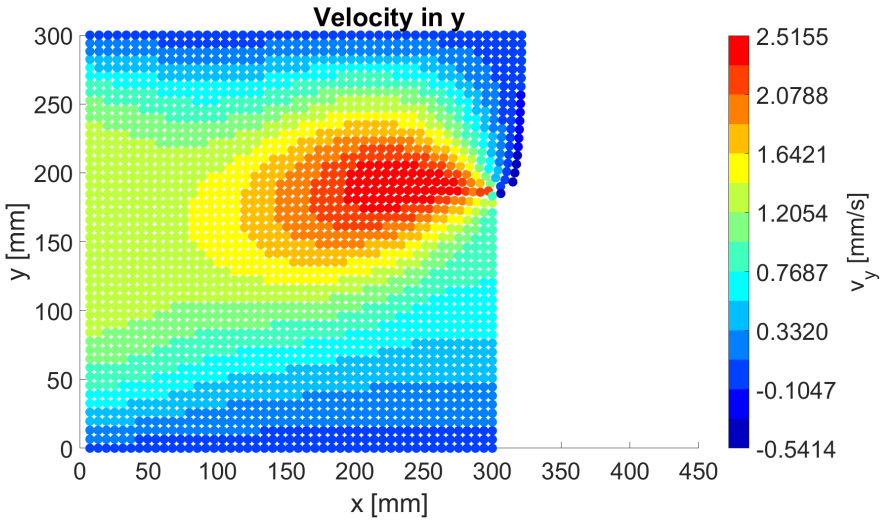


(c) Pressure at $t \approx 17,5s$.

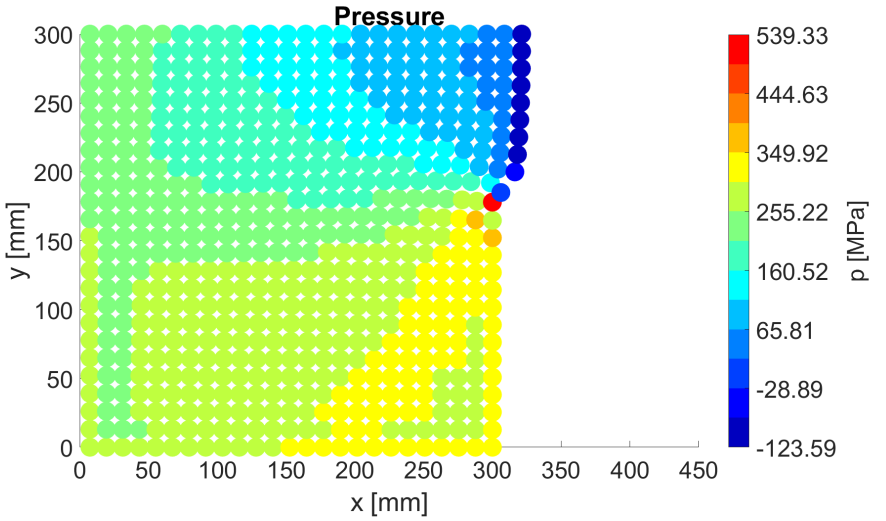
Figure 4.123: Reference results over time from the meshless study [2].



(a) Velocity in x.

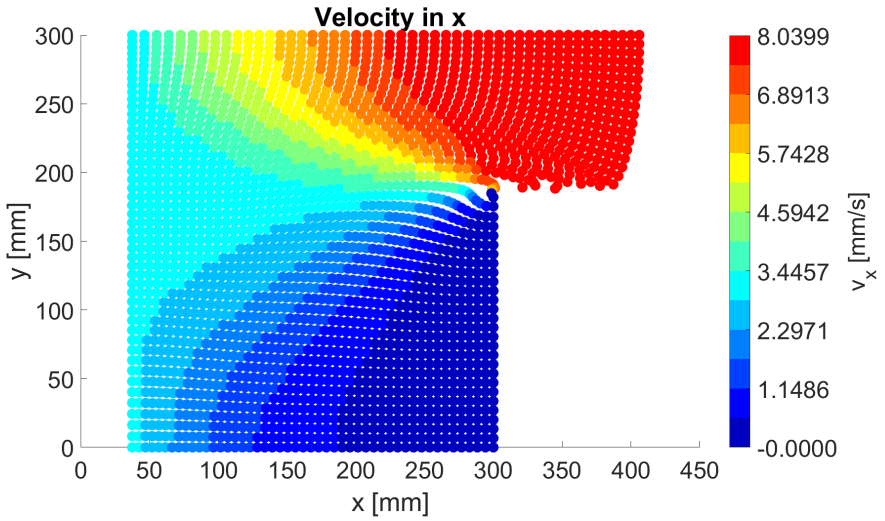


(b) Velocity in y.

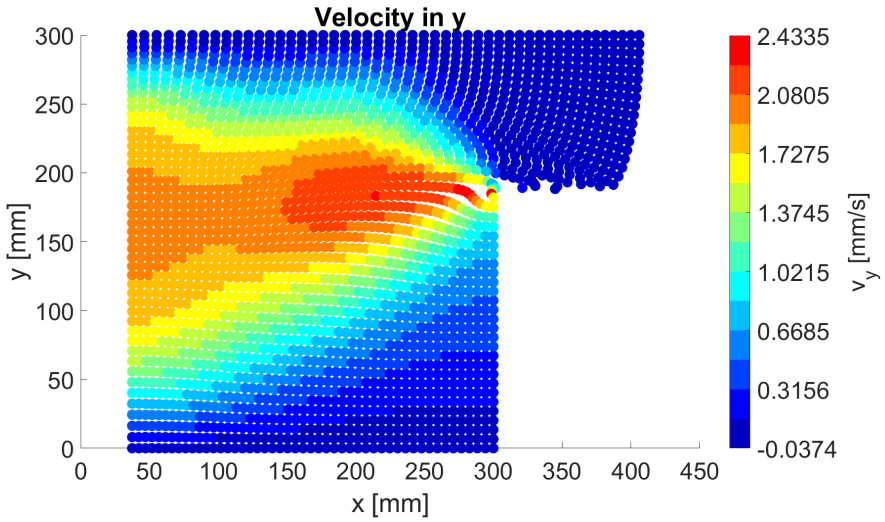


(c) Pressure.

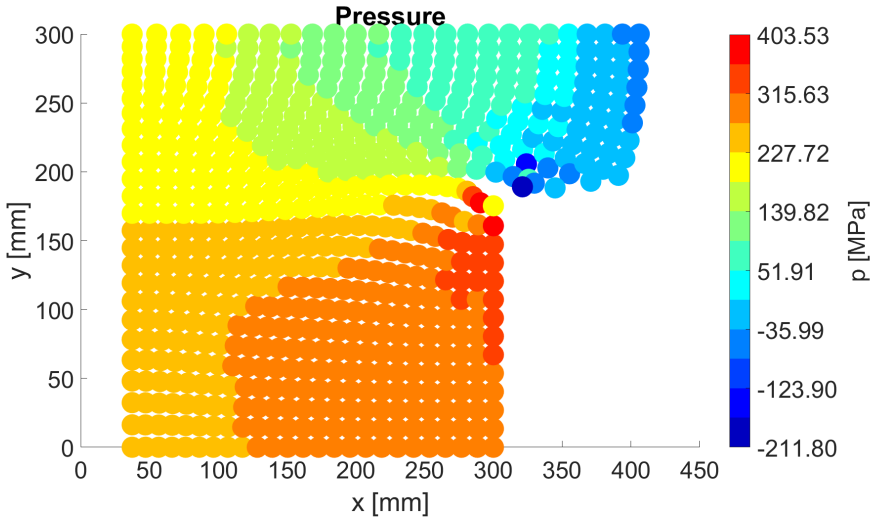
Figure 4.124: Results from the mixed dual method at $t = 2,5$.



(a) Velocity in x.

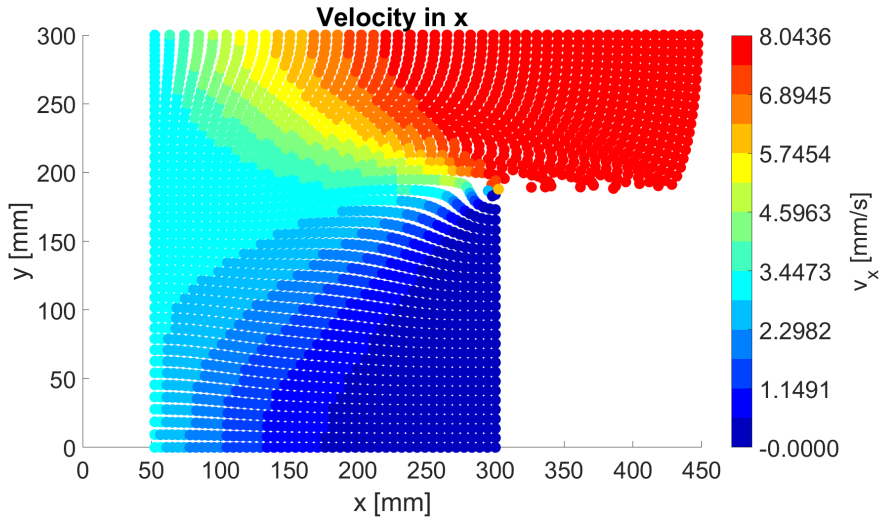


(b) Velocity in y.

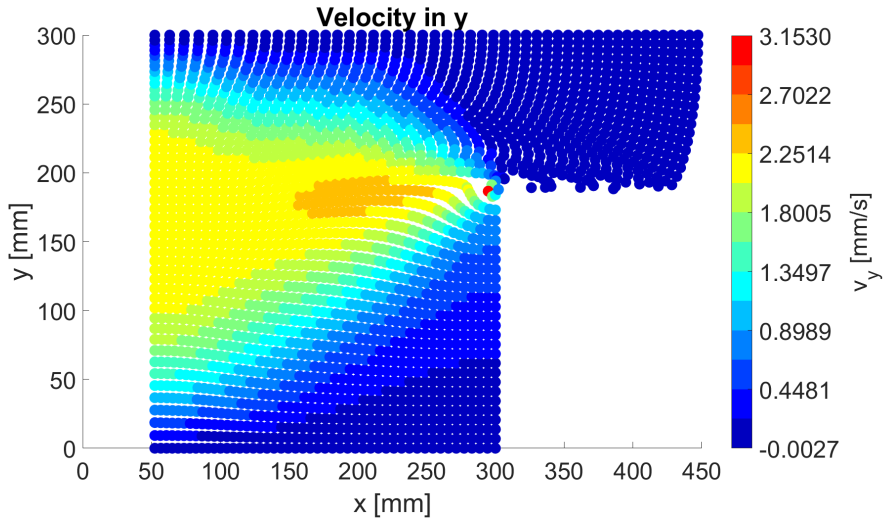


(c) Pressure.

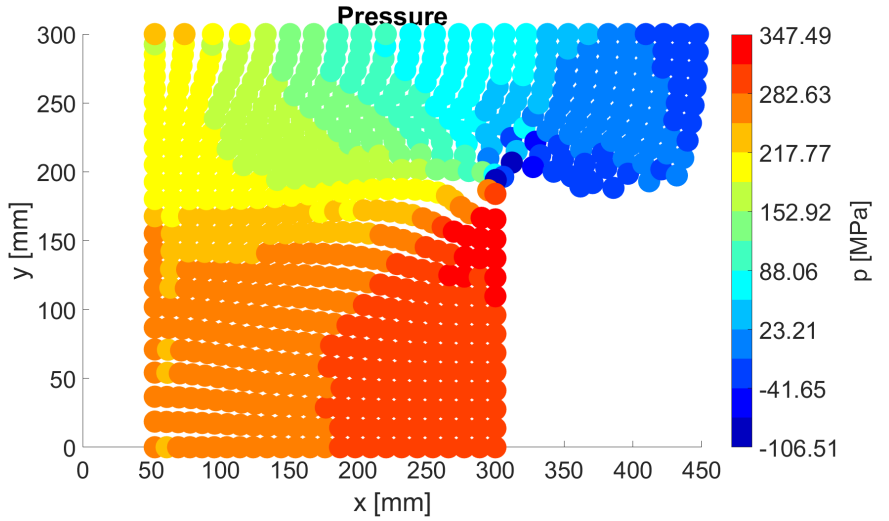
Figure 4.125: Results from the mixed dual method at $t = 12,5$.



(a) Velocity in x.



(b) Velocity in y.



(c) Pressure.

Figure 4.126: Results from the mixed dual method at $t = 17,5$.

From Figure 4.124, 4.125 and 4.126 , it is possible to understand how the solution

evolves. It is possible to observe in both the velocities and pressure fields that there are some numerical fluctuations, high spots or peaks where one node has a much higher value than the ones surrounding it. This can be the result of several scenarios. Firstly, during the simulation, there is the possibility that neighbour nodes become so close that the distance between them leads to numerical instabilities and badly conditioned matrices (this was observed during the analyses). The second possible factor has to do with the penalty nature of the formulation, once again prone to causing numerical instabilities. Thirdly, there is also the fact that the weight attributed to each integration point is considered to be constant. This is a rough approximation since some nodes tend to get closer together and others further apart, the numerical volume/area of each integration point must, consequently, change. Despite this, in this work this weight change was not accounted for and therefore is considered to be constant. Thus, possibly this can lead to some degree of inaccuracy in zones where this change is more pronounced.

Observing closely Figures 4.124c, 4.125c and 4.126c, and comparing them to 4.123, it is possible to observe that the results are very close. Although the time steps may not exactly match, the numerical values are in the same order of magnitude with the pressure at $t = 17,5$ (Figure 4.126c), showing a value very close with the one reported in the literature. In these, the numerical peaks are still visible, although it appears to smooth as time moves on. However, some negative values of the pressure can be observed and also that these are not uniformly distributed along the model, rather, they appear to be sporadic and irregular.

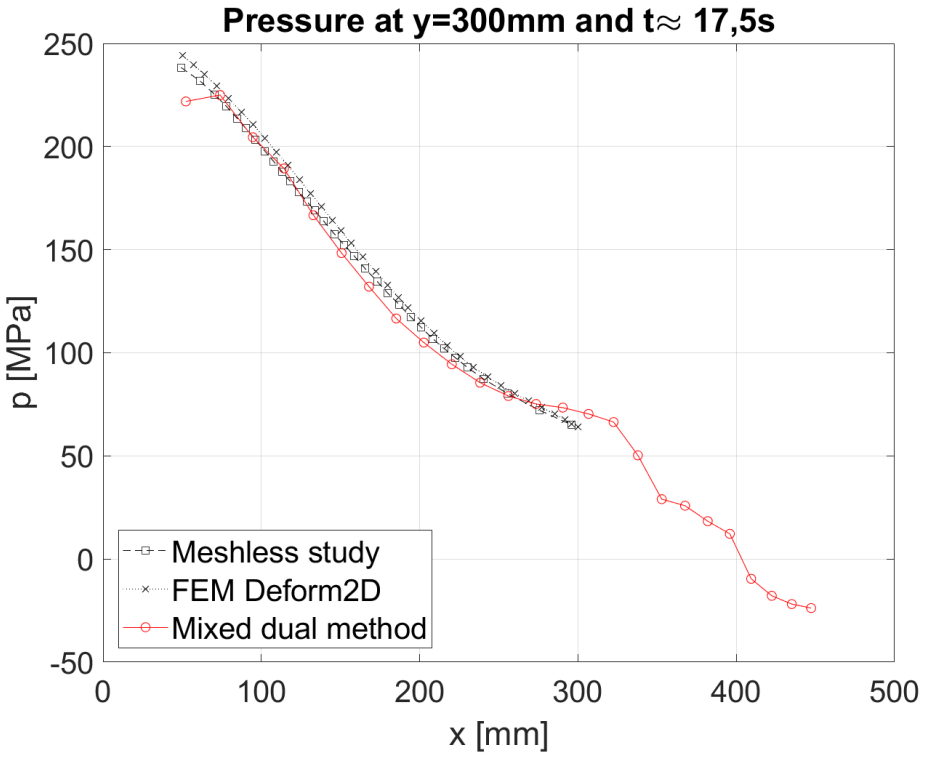


Figure 4.127: Comparison, with reference study, of pressure at $y = 300\,mm$ and $t \approx 17,5\,s$.

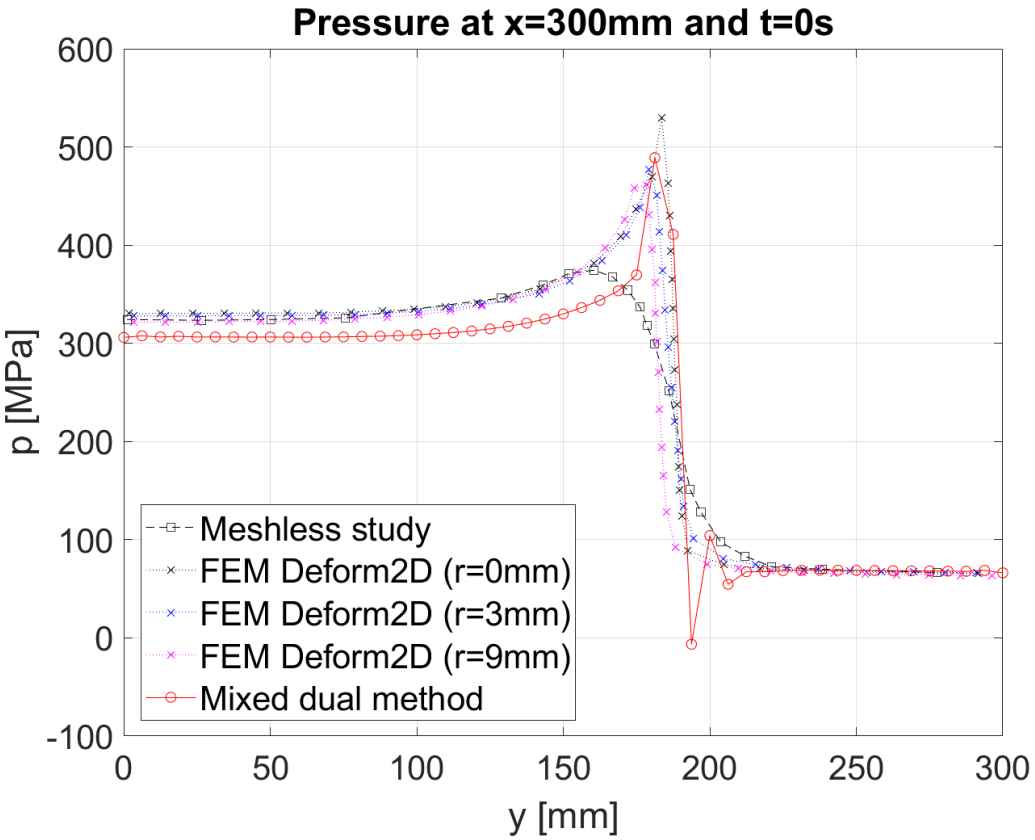


Figure 4.128: Comparison, with reference study, of pressure at $x = 300\,mm$ and $t = 0\,s$.

In Figures 4.127 and 4.128 there is a comparison between datasets obtained from the reference study for meshless method used and, also, the FEM result from Deform2D software and the data from the mixed dual method.

In Figure 4.127, it is plotted the pressure at $y = 300\,mm$ and at time step $t \approx 17,5\,s$. This value for time step was obtained based on the fact that the reference data starts on $x = 50\,mm$. In this plot, it is possible to observe a very good agreement between methods. Also, after $x = 300\,mm$ the mixed dual method's solution appears to oscillate while its slowly decreasing into negative values.

In Figure 4.128, it is plotted the pressure at $x = 300\,mm$ and at the first time step. Notice that the Deform2D FEM results feature three distinct versions based on the parameter r. This parameter represents the radius of the outlet of the extruder. It is possible to observe that as the radius increases the peak of the solutions decreases. The mixed dual method's solution features a peak that is coherent with the fact that in this work $r = 0\,mm$ was used. Also, it is possible to see that the methods have a very good numerical agreement. There are slight differences in the first half of the curve before the peak. Also, there is an oscillation in the value of the mixed dual method near the $x = 200\,mm$ mark, which can be associated with some kind of numerical stress concentration.

Chapter 5

Benchmark results

5.1 Problem Definition

In the previous chapter, the flow formulation was compared to the literature using a problem with a relatively simple geometry. Despite its simplicity, it allowed to determine which of the methods provides the best results, and what are the optimal parameters for the proposed formulation. Now, with that method and those optimal parameters, it is important to test the formulation in different problems with different, more complex, geometries.

For this, a 2D FEM study of aluminium extrusion by *Li et al.* was selected [3]. In this, the isothermal extrusion process is simulated using the Deform2D commercial package. Four different models are considered to compare different geometrical configurations of extrusion die. Specifically, to study the effect of the number of steps on a stepped die and how it compares to a conical die. The study in question takes into account the friction in the walls of the dies, which was not implemented in this work. For this reason, the aim of this section is not to numerically compare the results but to test the method in different domain configurations.

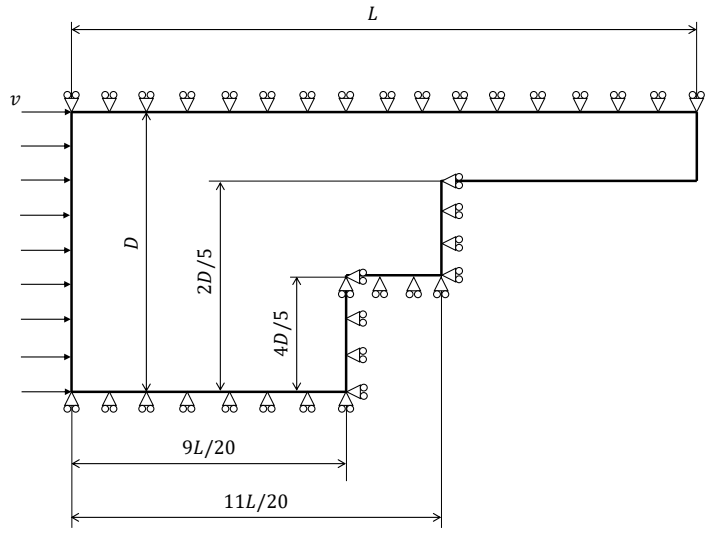


Figure 5.1: Die model with just one step.

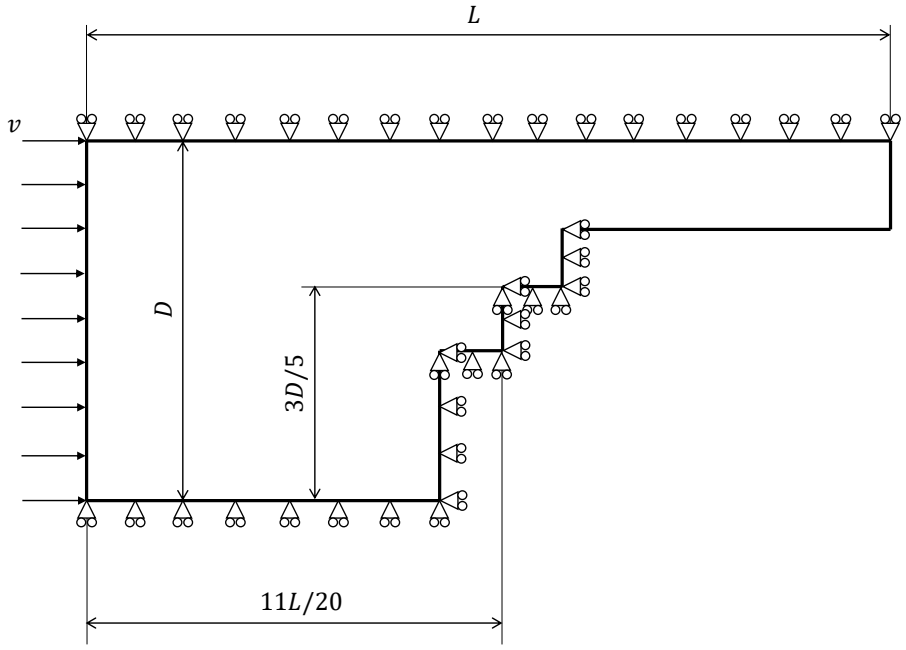


Figure 5.2: Die model with two steps.

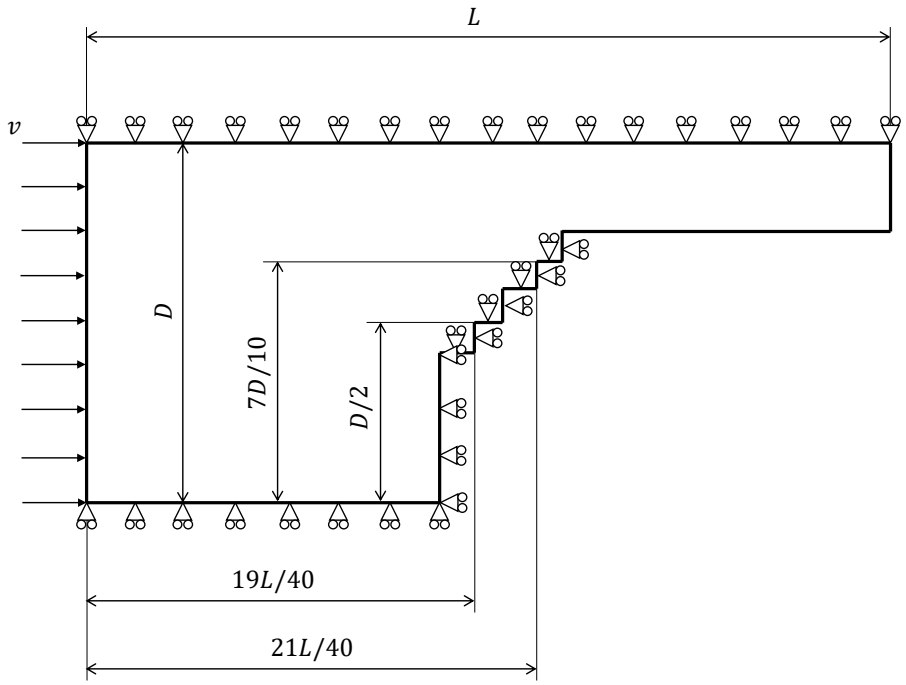


Figure 5.3: Die model with four steps.

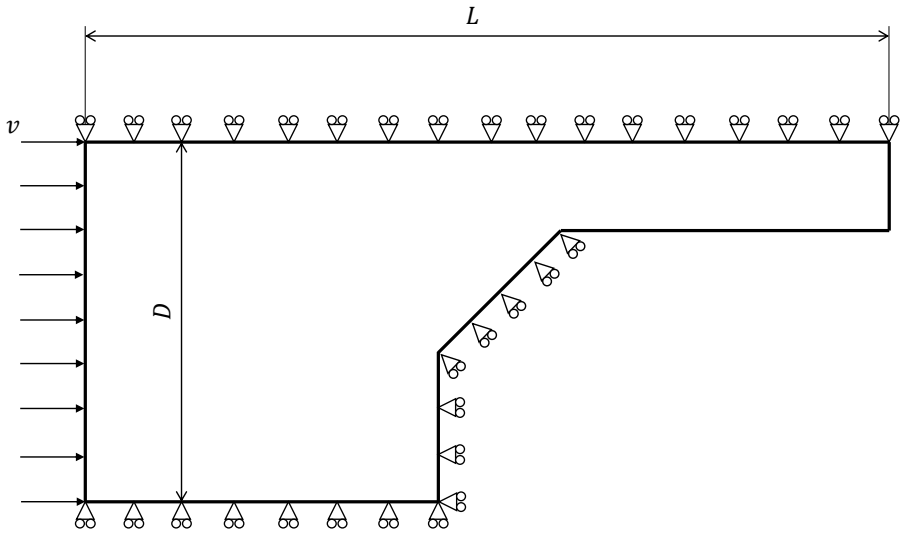


Figure 5.4: Conical die model.

Figures (5.1) to (5.4) contain the schematic representations of the four models studied in this work, with, [3]

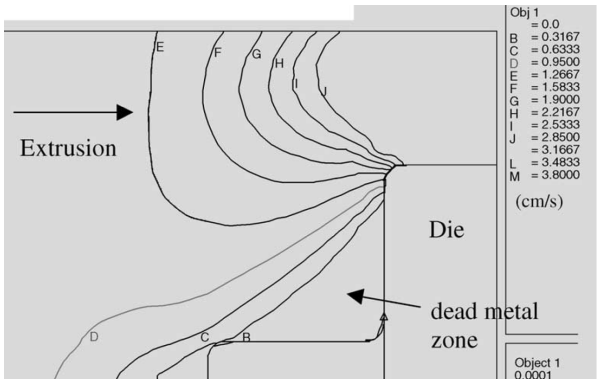
$$\begin{aligned} L &= 0,1\,\mathrm{m}, \\ D &= 0,025\,\mathrm{m}, \\ v &= 0,01\,\mathrm{m/s}. \end{aligned} \tag{5.1}$$

These models where simulated considering an aluminium material and the material law defined in equation (3.35) with the following parameters,

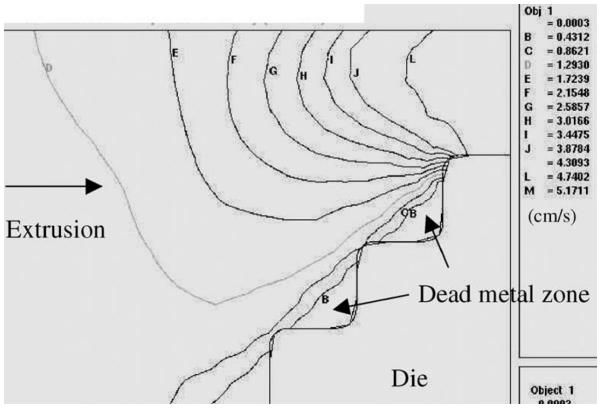
Table 5.1: Parameters used for simulation [3, 4],

Parameter	Value
μ_0	2800 Pa · s
σ_y	10,7 MPa
γ	52,4
n	0,4

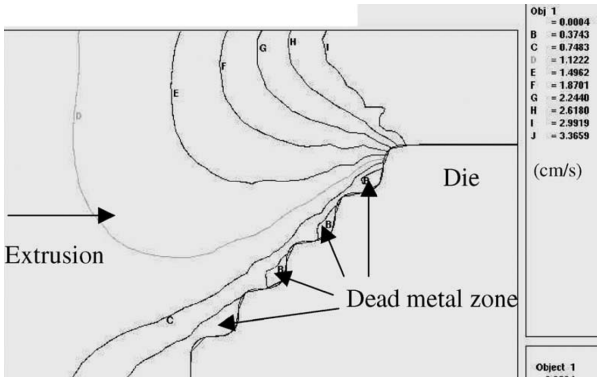
Even though the direct numerical comparison is not the main purpose of this example, it is important to have a reference to base analysis and conclusions on. For this reason, it is important to documented here the results obtained in the FEM study, which can be observed in Figure 5.5.



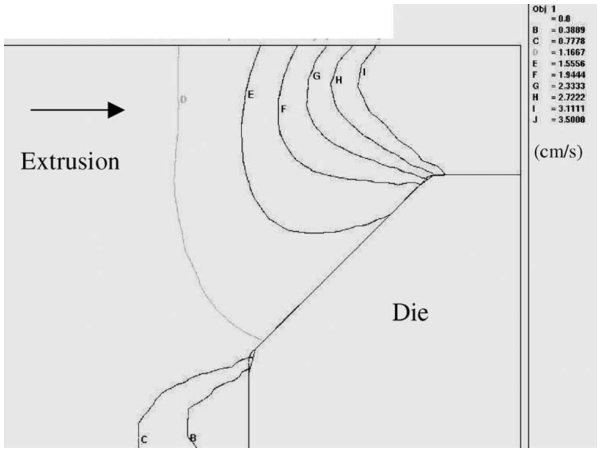
(a) Model 1.



(b) Model 2.



(c) Model 3.

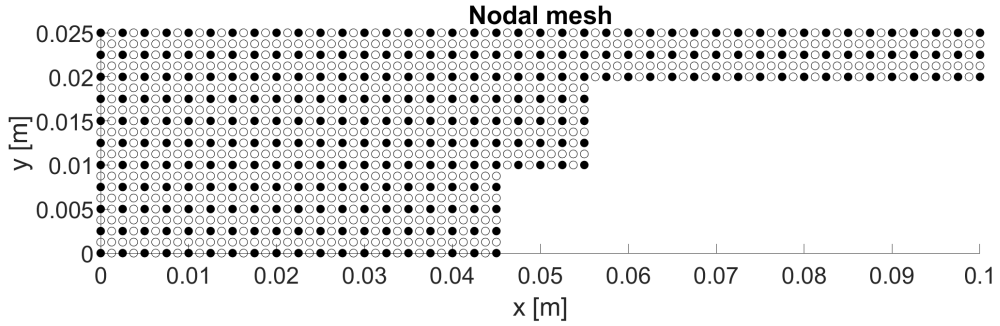


(d) Model 4.

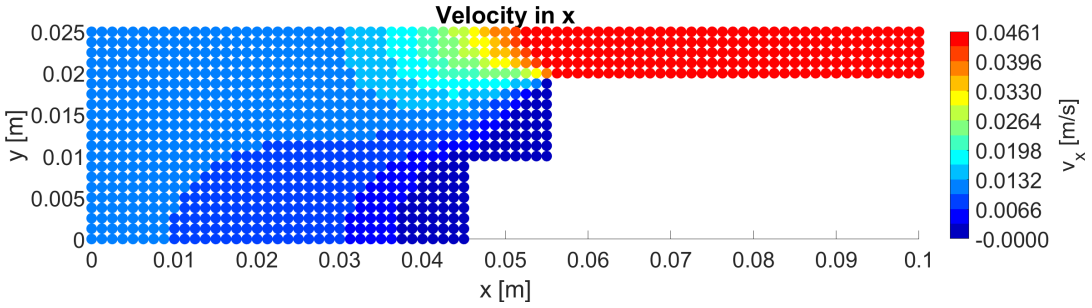
Figure 5.5: Reference results from the FEM study [3].

5.2 Mixed Dual Method

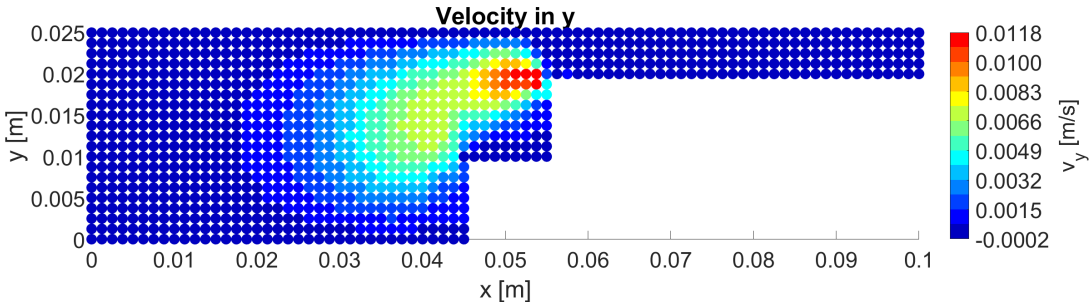
The results using the mixed dual method were as follows in Figures 5.6 to 5.9.



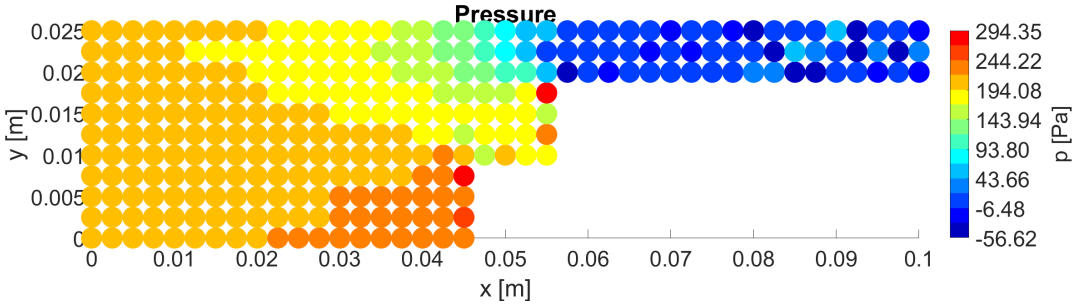
(a) Nodal mesh.



(b) Velocity in x.

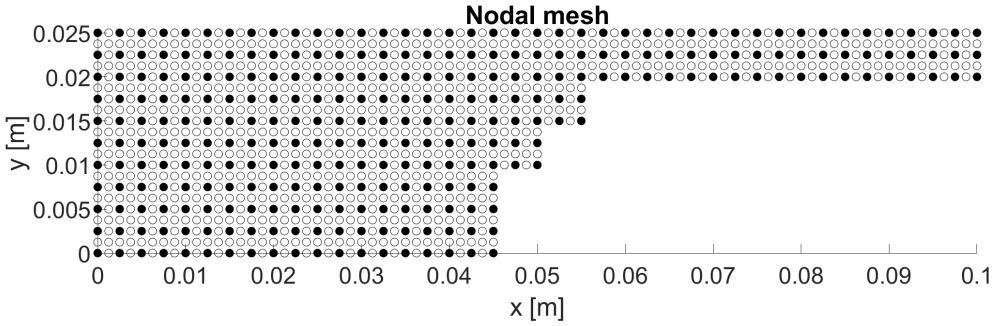


(c) Velocity in y.

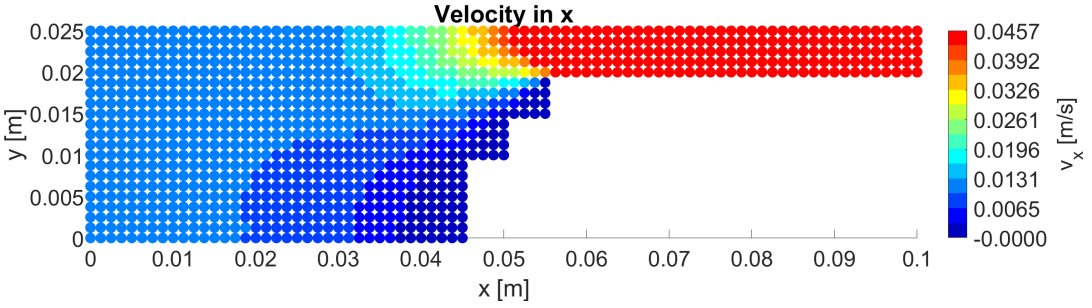


(d) Pressure.

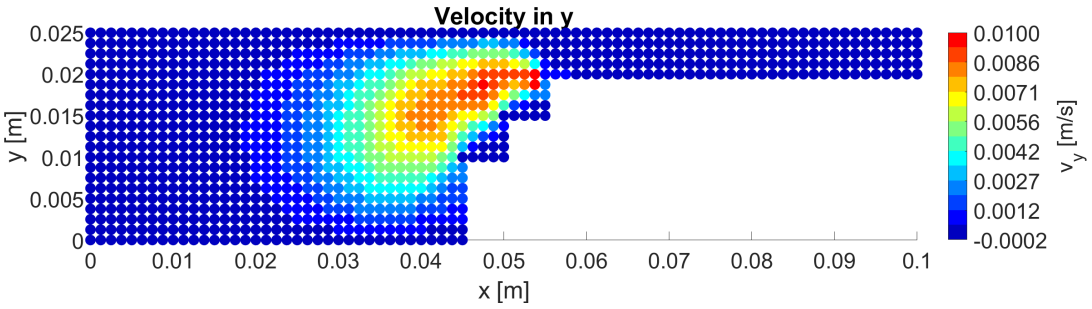
Figure 5.6: Results of the first model, with 1 step.



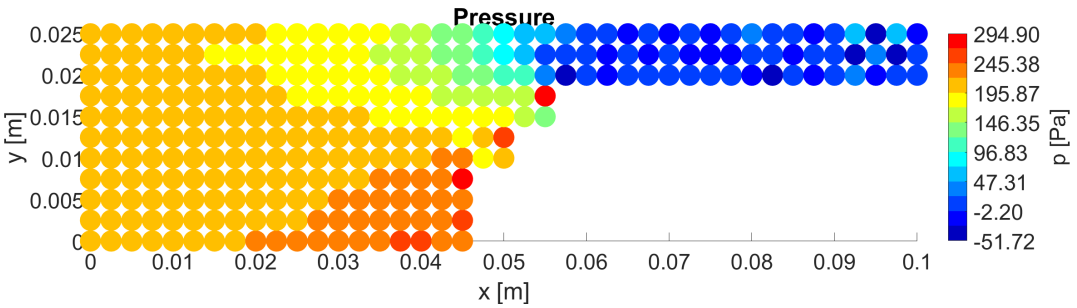
(a) Nodal mesh.



(b) Velocity in x.

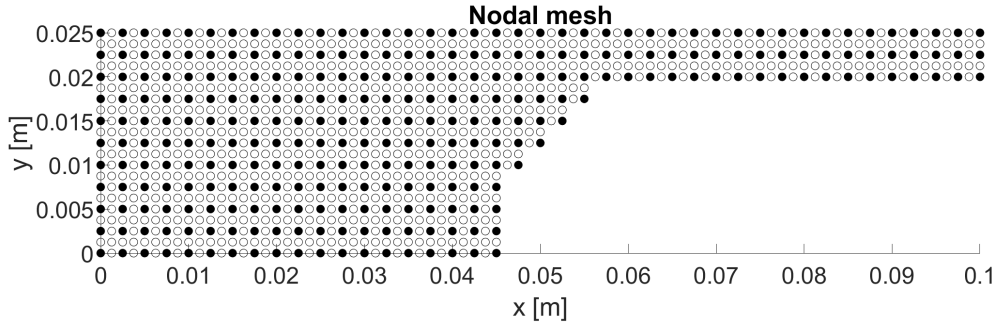


(c) Velocity in y.

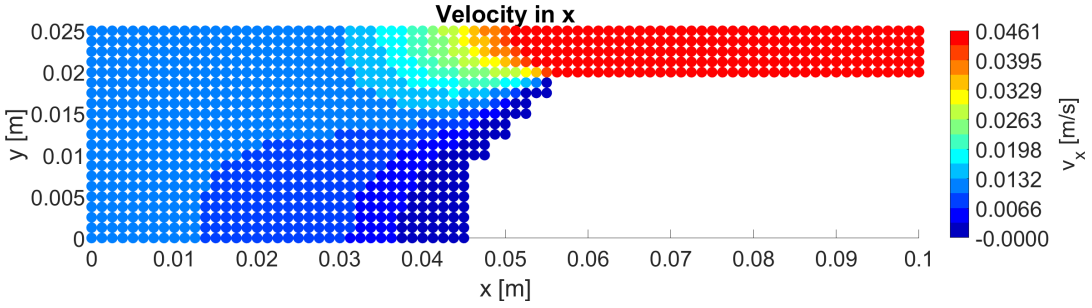


(d) Pressure.

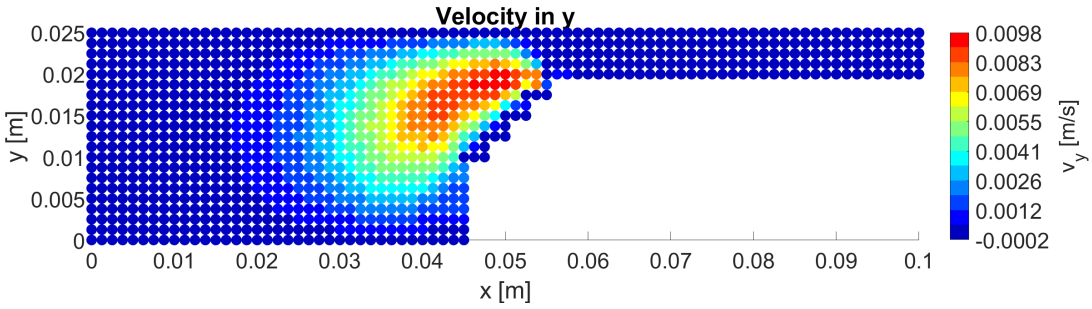
Figure 5.7: Results of the second model, with 2 steps.



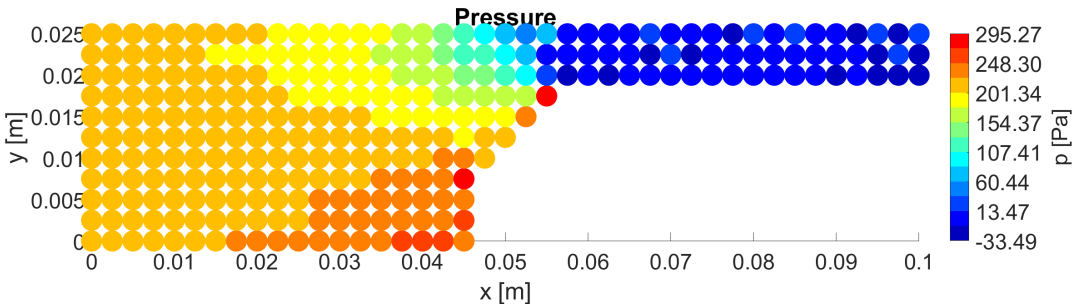
(a) Nodal mesh.



(b) Velocity in x.

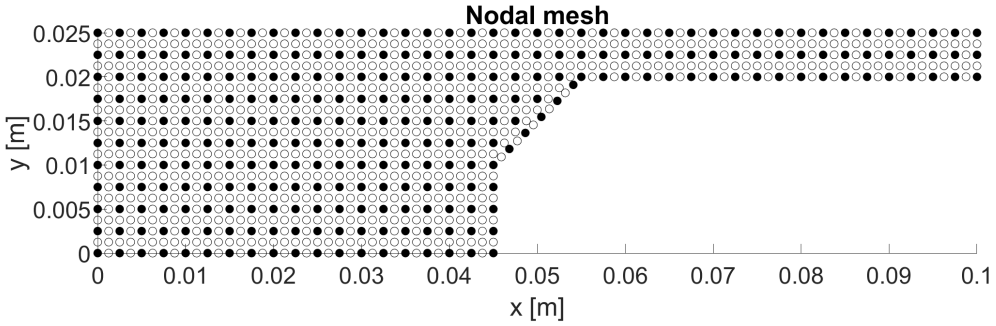


(c) Velocity in y.

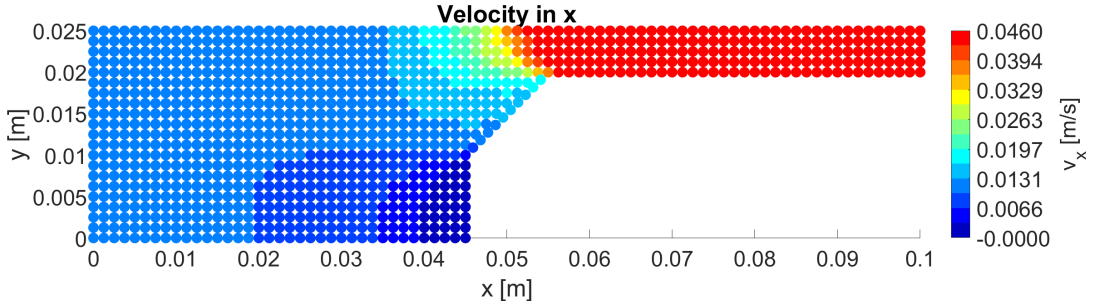


(d) Pressure.

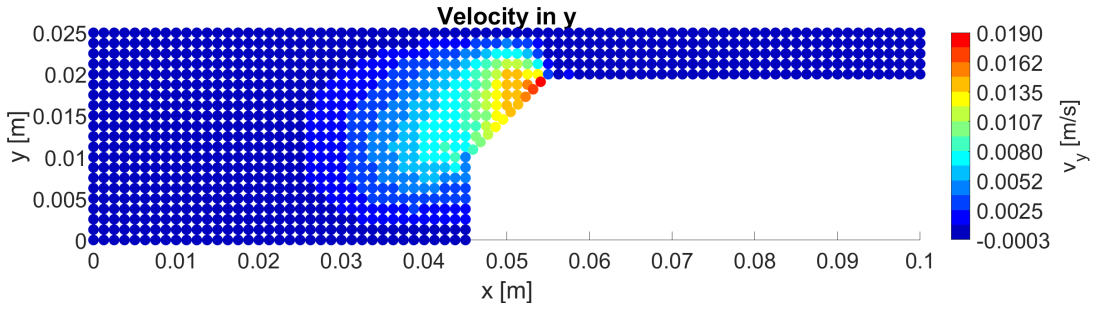
Figure 5.8: Results of the third model, with 4 steps.



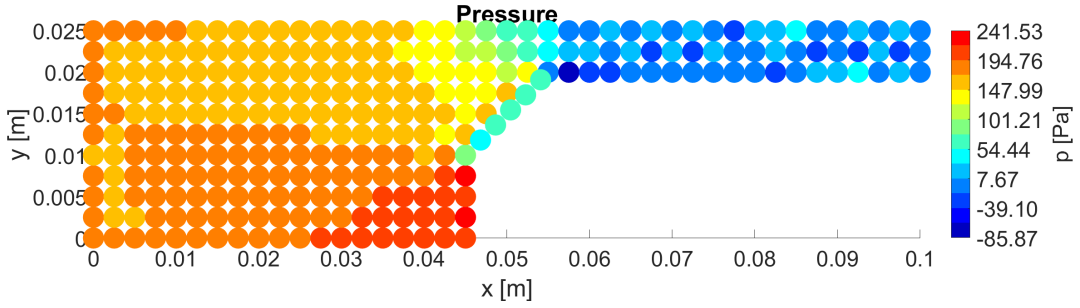
(a) Nodal mesh.



(b) Velocity in x.



(c) Velocity in y.



(d) Pressure.

Figure 5.9: Results of the fourth model, the conical die.

In Figures 5.6a, 5.7a, 5.8a and 5.9a the nodal meshes associated with each of the four models are represented, in which the velocity-only nodes are represented in white and the shared velocity-pressure nodes are represented in black. This allows to more clearly observe the different discretizations associated with each of the field variables.

Moreover, it is possible to observe that the velocity results (the ones with a reference to compare with) are in the same order of magnitude with some values being actually very close to the ones in the study, namely the die with 2 steps. Notice that there is no information regarding the time step at which the contours shown in Figure 5.5 were plotted but, nonetheless, this is a good indicator that the method described in this work is providing physically valid results. As for the other models, the velocity values appear to be lower in the FEM study, which is to be expected given that friction was not accounted for in this work, thus, the material can slide freely in the walls of the dies.

As for the pressure fields represented in 5.6d, 5.7d, 5.8d and 5.9d, it is not possible to make a direct comparison, although, the quality of the results can be evaluated comparing them to what was previously seen from the mixed dual method. It is possible to observe the same numerical instabilities that seem to be a standard in this formulation, however they seem more pronounced in this problem. It is especially visible in the wall areas leading to the outlet, where some peaks show up rather sporadically, and also it can be seen in the portion of material that's already out of the extruder. In these nodes same darker blue spots with a negative pressure value can be seen in somewhat of a patterned distribution. These can be caused by several factors, some hypothesis were already made in previous chapters concerning the penalty-based formulation and how it leads to poorly conditioned matrices and numerical instabilities.

Finally, there is an issue visible in the pressure field in Figure 5.9d, in the inclined boundary leading to the outlet of the extruder. Observing the evolution of the geometry between the four models, it is visible that the volume of the dead metal zone decreases from model to model. This leads to the conclusion that from the stepped models to the model with the inclined border, it should be expected less resistance to the flow in the latter case as there is no vertical boundary retaining material. Thus, it should also be expected that this decrease in flow resistance should originate a decrease in pressure. Numerically, it is observed that in this boundary the pressure obtained is much lower than its surroundings, resulting in a jump. In this case, it appears that the cause results from the transformation needed to imposed boundary conditions on inclined supports.

This page has been intentionally left blank.

Chapter 6

Conclusion

In this work, a numerical tool to simulate the entire extrusion process of viscoplastic materials was created. The algorithm seeks the velocity and pressure fields iteratively and it is able to perform this at different time steps to document the process along time. Given that, in each iteration the mesh is updated considering the nodal velocity of the previous iteration.

The RPIM proved to be a capable and solid method to study the *flow formulation* problems. The results obtained with the RPIM were in accordance with the examples from literature of a more recent meshless method and the FEM. Also, being completely discretized by nodes, the RPIM was a valuable tool for the remeshing at each time step, turning it into a simple and computationally light task. Particularly suited for a Lagrangian-type approach, as the one implemented in this work.

Moreover, programming the RPIM turned out to be a pleasant task. In the case of the FEM, each element has to be separately programmed as the shape functions, stiffness matrix, strain matrix and so on, are all element dependent. In the RPIM, the formulation is much more parameter based because of the concept of influence domain and the nodal independence. For the same program structure, the possibility to have influence domains with different sizes, shapes or number of nodes inside them makes for a versatile and flexible method.

The *flow formulation* showed its value in the simulation of the extrusion process, and proved to a good approach to study fluid-like behaviour using a formulation almost entirely ported from solid mechanics. However, due to the iterative nature of the time stepped approach and also the non linear iterative extrusion process, some drawbacks and challenges can be identified. On one hand, the fact that a simple linear time integration is performed in every time step is a crude approximation since a significant amount of information is being lost, even for very small values of Δt. On the other hand, the computational cost can be very high when simulating complex problems over a relatively small amount of time steps. For instance, the simulation of just $17,5\,s$ at $0,05\,s/iteration$ took about 27 hours and 35 minutes of computing time.

Moreover, the formulation is based upon the penalty method to impose the incompressibility constraint and consequently to obtain the pressure field. For this reason, it was observed throughout the examples that numerical instabilities appear especially in the pressure field. These took the form of numerical stress concentrations, fluctuations or peaks that are not physically coherent but are caused by the numerical method. These peaks appeared to be more common in areas where

boundaries existed and also high pressure gradients where to be expected. Despite these instabilities, the method was capable of producing physically valid and accurate results in agreement with those in the literature.

The formulation was obtained in an iterative fashion resulting in 3 versions: the direct penalty method, the mixed method and the mixed dual method. Each one that followed was an attempt to obtain better results than the previous, usually in the pressure field. It was observed throughout this process that the formulation is prone to a locking phenomenon, which could easily be attained in the direct and mixed dual methods by using hybrid integration. In the first case, by using two integration meshes one less dense than the other, and in the second by using a nodal discretization for each degree of freedom, with different nodal densities and the same integration mesh. Both the solutions were valid although the first was more sensitive to numerical instabilities.

It was found in the development of the mixed dual method that the formulation using the RPIM is highly dependent on some parameters. These are the order of integration, the number of nodes inside the influence domains, the mesh regularity and the nodal density.

Concerning the order of integration, it was observed that the higher it was, the more stable the solution became, as it converged with the increasing number of integration points. Also, the computation time increased exponentially with the order of integration. A good compromise was found for $quado = 6$.

As for the influence domains, in the mixed dual method it was observed that only above $n_{dom} = 13$ a valid solution was obtained, with the value stabilizing in the following increments around $n_{dom} = 18$. Similarly to the order of integration, the computing time also increased with the increase in the size of influence domains, although not as much.

In terms of mesh regularity it was found that the method preferred regular meshes over irregular ones, since the latter introduced visible fluctuations and numerical errors into the solution. However, this numerical error was found to be as low as 3% with the most irregular mesh tested, which provides confidence that the method is able to provide sound results regardless of the regularity of the nodal discretization.

Finally, in terms of nodal density the formulation showed a satisfactory convergence after approximately 2500 nodes. Additionally, due to the slope verified in the asymptotic convergence line it was possible to conclude that the method is characterized by a fast convergence, as it takes less nodes to converge.

Also, by testing the method with a more complex problem it was possible to conclude that it is robust enough to handle more complex geometries with the same quality of results witnessed in the simpler problem.

The present work is an introductory application of the RPIM and meshless methods to *flow formulation*. There is plenty of room for improvements and developments on this work. Some interesting possibilities can be identified:

- Introduce friction and temperature into the formulation. Viscosity and yield stress are heavily temperature dependent, so it would be interesting to be able to model these contributions as well;

- Introduce empirical models for polymer materials, such as PLA. This would be a way to test this method and formulation in a true FDM context;

- Expand this program to simulate the contact with the bed and the coalescence between layers to incorporate the full FDM process;
- Test a truly meshless method, completely nodal dependent to eliminate the need for an integration mesh. This way more freedom and versatility would be gained.

Ultimately, in this work, a numerical tool capable of accurately providing the velocity and pressure fields resulting from the extrusion of viscoplastic materials was developed.

This page has been intentionally left blank.

Bibliography

[1] O. C. Zienkiewicz, R. L. Taylor, and P. Nithiarasu, "Chapter 4 - Incompressible Newtonian Laminar Flows BT - The Finite Element Method for Fluid Dynamics (Seventh Edition)," pp. 127–161, Oxford: Butterworth-Heinemann, 2014.

[2] F. Greco, L. Filice, C. Peco, and M. Arroyo, "A stabilized formulation with maximum entropy meshfree approximants for viscoplastic flow simulation in metal forming," *International Journal of Material Forming*, vol. 8, no. 3, pp. 341–353, 2015.

[3] Q. Li, C. J. Smith, C. Harris, and M. R. Jolly, "Finite element modelling investigations upon the influence of pocket die designs on metal flow in aluminium extrusion: Part II. Effect of pocket geometry configurations on metal flow," *Journal of Materials Processing Technology*, vol. 135, no. 2-3 SPEC., pp. 197–203, 2003.

[4] O. C. Zienkiewicz, E. Oñae, and J. C. Heinrich, "A general formulation for coupled thermal flow of metals using finite elements," *International Journal for Numerical Methods in Engineering*, vol. 17, no. 10, pp. 1497–1514, 1981.

[5] R. A. Gingold and J. J. Monaghan, "Smoothed particle hydrodynamics: theory and application to non-spherical stars," *Monthly Notices of the Royal Astronomical Society*, vol. 181, pp. 375–389, dec 1977.

[6] B. Nayroles, G. Touzot, and P. Villon, "Generalizing the finite element method: Diffuse approximation and diffuse elements," *Computational Mechanics*, vol. 10, no. 5, pp. 307–318, 1992.

[7] T. Belytschko, Y. Y. Lu, and L. Gu, "Element-free Galerkin methods," *International Journal for Numerical Methods in Engineering*, vol. 37, pp. 229–256, jun 1994.

[8] L. W. Kam, J. Sukky, and Z. Y. Fei, "Reproducing kernel particle methods," *International Journal for Numerical Methods in Fluids*, vol. 20, pp. 1081–1106, jun 1995.

[9] N. Sukumar, B. Moran, and T. Belytschko, "The natural element method in solid mechanics," *International Journal for Numerical Methods in Engineering*, vol. 43, pp. 839–887, dec 1998.

[10] S. N. Atluri and T. Zhu, "A new Meshless Local Petrov-Galerkin (MLPG) approach in computational mechanics," *Computational Mechanics*, vol. 22, no. 2, pp. 117–127, 1998.

[11] S. De and K. J. Bathe, "The method of finite spheres," *Computational Mechanics*, vol. 25, no. 4, pp. 329–345, 2000.

[12] G. R. Liu and Y. T. Gu, "A point interpolation method for two-dimensional solids," *International Journal for Numerical Methods in Engineering*, vol. 50, pp. 937–951, jan 2001.

[13] G. R. Liu, "A point assembly method for stress analysis for two-dimensional solids," *International Journal of Solids and Structures*, vol. 39, no. 1, pp. 261–276, 2002.

[14] J. G. Wang and G. R. Liu, "A point interpolation meshless method based on radial basis functions," *International Journal for Numerical Methods in Engineering*, vol. 54, pp. 1623–1648, may 2002.

[15] I. S. R., O. Eugenio, C. Nestor, and D. P. Facundo, "The meshless finite element method," *International Journal for Numerical Methods in Engineering*, vol. 58, pp. 893–912, jul 2003.

[16] L. M. J. S. Dinis, R. M. Natal Jorge, and J. Belinha, "Analysis of 3D solids using the natural neighbour radial point interpolation method," *Computer Methods in Applied Mechanics and Engineering*, vol. 196, no. 13–16, pp. 2009–2028, 2007.

[17] W. Gao, Y. Zhang, D. Ramanujan, K. Ramani, Y. Chen, C. B. Williams, C. C. L. Wang, Y. C. Shin, S. Zhang, and P. D. Zavattieri, "The status, challenges, and future of additive manufacturing in engineering," *Computer-Aided Design*, vol. 69, pp. 65–89, 2015.

[18] S. Ford and M. Despeisse, "Additive manufacturing and sustainability: an exploratory study of the advantages and challenges," *Journal of Cleaner Production*, vol. 137, pp. 1573–1587, 2016.

[19] J. Lof, "Elasto-viscoplastic FEM simulations of the aluminium flow in the bearing area for extrusion of thin-walled sections," *Journal of Materials Processing Technology*, vol. 114, no. 2, pp. 174–183, 2001.

[20] O. Zienkiewicz, *Flow formulation for numerical solution of forming processes*. jan 1984.

[21] E. Cueto and F. Chinesta, "Meshless methods for the simulation of material forming," *International Journal of Material Forming*, vol. 8, no. 1, pp. 25–43, 2015.

[22] P. Lu, G. Zhao, Y. Guan, and X. Wu, "Bulk metal forming process simulation based on rigid-plastic/viscoplastic element free Galerkin method," *Materials Science and Engineering: A*, vol. 479, no. 1, pp. 197–212, 2008.

[23] O. C. Zienkiewicz, R. L. Taylor, and P. Nithiarasu, "Chapter 3 - The Characteristic-Based Split (CBS) Algorithm: A General Procedure for Compressible and Incompressible Flow BT - The Finite Element Method for Fluid Dynamics (Seventh Edition)," pp. 87–125, Oxford: Butterworth-Heinemann, 2014.

[24] J. Belinha, *Meshless Methods in Biomechanics: Bone Tissue Remodelling Analysis*. Lecture Notes in Computational Vision and Biomechanics, Springer International Publishing, 2014.

[25] K. Tian, J. Chen, L. Han, J. Yang, W. Huang, and D. Wu, "Angled abutments result in increased or decreased stress on surrounding bone of single-unit dental implants: A finite element analysis," *Medical Engineering and Physics*, vol. 34, no. 10, pp. 1526–1531, 2012.

[26] O. C. Zienkiewicz, Y. C. Liu, and G. C. Huang, "Error estimation and adaptivity in flow formulation for forming problems," *International Journal for Numerical Methods in Engineering*, vol. 25, pp. 23–42, jan 1988.

[27] R. Temam, "A generalized Norton-Hoff model and the Prandtl-Reuss law of plasticity," *Archive for Rational Mechanics and Analysis*, vol. 95, no. 2, pp. 137–183, 1986.